Computational study of statistically one-dimensional propagation of turbulence

Vom Fachbereich Maschinenbau
an der Technischen Universität Darmstadt
zur
Erlangung des Grades eines Doktor-Ingineurs (Dr.-Ing.)
genehmigte

D i s s e r t a t i o n

vorgelegt von

Dipl.-Ing. Emir Sirbubalo

aus Sarajevo

Berichterstatter:	Prof. Dr.-Ing. habil. C. Tropea
Mitberichterstatter:	Prof. Dr.-Ing. habil. M. Oberlack
	Apl. Prof. Dr.-Ing. habil. S. Jakirlić
Tag der Einreichung:	26. 01. 2012
Tag der mündlichen Prüfüng:	15. 05. 2012

Darmstadt 2012
D17

Hiermit versichere ich, die vorliegende Doktorarbeit unter der Betreuung von Prof. Dr.-Ing. C. Tropea nur mit den angegebenen Hilfsmitteln selbständig angefertigt zu haben.
Darmstadt, den 26. 01. 2012

Acknowledgments

Financial support by the Deutsche Forschungsgemeinschaft is gratefully acknowledged.

This work has been carried out at the Institute of Fluid Dynamics and Aerodynamcs SLA of the Technische Universität Darmstadt during the period between November 2006 to November 2010.

I would like to thank Prof. Dr.-Ing. habil. Cameron Tropea and Apl. Prof. Dr.-Ing. habil. Suad Jakirlić for the possibility to do this work and for their helpful comments on the present work. Thanks are also due to Prof. Dr.-Ing. habil. Martin Oberlack for taking on the second supervisor role and Dr.-Ing. George Khujadze and Dr.-Ing. Matthias Kinzel for their constructive support.

I would also like to thank the administrative staff of the SLA institute for their profesionalism and help in making sure formalities were taken care of.

Thanks go to my colleagues and friends from the SLA Institute for creating a pleasant atmosphere, both working and extracurricular.

Thanks to my friends and family for the never-ending support and encouragement.

Abstract

Symmetry analysis of the evolution equation of the two-point correlation tensor $R_{ij}\left(x_k, r_l, t\right)$ in the case of planar generation of turbulence in an otherwise quiescent semi-infinite body of fluid has revealed some interesting solutions concerning the statistical properties of turbulence and how they develop with distance from the generation source. The first solution concerns the classical case of shear-free turbulent diffusion. Here, the turbulent kinetic energy is distributed according to a power law x^{-n} where n is a constant larger than one, and x is the normal distance to the forcing plane. The integral length scales of turbulence increase linearly with x. A second case is considered when the symmetry of scaling of space is broken by introducing confinement to the flow. The turbulent kinetic energy decays with x as $\exp\left(-x\right)$ and the integral length scales remain constant along x. A third case treated is turbulent diffusion in a rotating frame, where symmetry of scaling of time is broken. Turbulent kinetic energy is distributed according to x^{-2} and there is an upper limit to turbulence propagation.

The purpose of the present work is to investigate characteristics of this type of flow by means of large eddy simulation. Turbulent fields are generated in a box of isotropic turbulence using standard procedures. Planar samples of the generated fields are fed as a series of unsteady and nonuniform boundary conditions to the zero initial fields in an elongated turbulence box and turbulence propagation is monitored. The three cases are distinguished in simulations by imposing periodic and slip boundary conditions on lateral sides of the simulation box for the cases of free and confined turbulent diffusion respectively, and by solving LES equations in the rotating frame of reference for the third case. Specifically, the present work discusses identification criteria of turbulent front from filtered fields of LES turbulence. Furthermore, propagation of the front and associated profiles of turbulent kinetic energy and vorticity are discussed and compared to experimental and direct numerical simulation results. Complementing the main results, principles of symmetry analysis of two-point correlation equations and a description of the algorithm used for generation of the isotropic and rotating homogeneous turbulence fields are given. Finally, the performance of the presently popular Reynolds-averaged models in the three cases is evaluated.

Kurzfassung

Die Symmetrieanalyse der Evolutionsgleichung des Zweipunktkorrelationstensors $R_{ij}\left(x_k, r_l, t\right)$ hat im Falle der planaren Erzeugung von Turbulenz im semiunendlichen Fluidraum einige interessante Lösungen bezüglich der statistischen Eigenschaften der Turbulenz, und ihrer Entwicklung mit der Entfernung von der Erzeugungsquelle erkennen lassen. Die erste Lösung beschreibt den klassischen Fall der scherfreien turbulenten Diffusion. Hier folgt die turbulente kinetische Energie einem Potenzgesetz x^{-n}, wo n eine Konstante darstellt und x die senkrechte Koordinate zur Trubulenzebene ist. Das integrale Längenmaß nimmt mit x linear zu. Die zweite Lösung untersucht den Fall, in dem die Symmetrie der Raumskalierung durch die Einschränckung des Fluidraumes gebrochen ist. Die turbulente kinetische Energie fällt mit x als $\exp\left(-x\right)$ ab, und die integrale Längenmaße bleiben konstant. Der dritte in der vorliegenden Arbeit untersuchte Fall befasst sich mit der turbulenten Diffusion in einem rotierenden Koordinatensystem, wo die Symmetrie der Zeitskalierung gebrochen ist. Die turbulente kinetische Energie ist gemäß x^{-2} verteilt, und es gibt einen Grenzwert zur Turbulenzausbreitung.

Das Ziel der vorliegenden Arbeit ist es, die Eigenschaften der oben beschriebenen Strömungen mittels *large-eddy simulation* zu untersuchen. Die homogene isotrope Turbulenz ist in einem Simulationswürfel anhand des allgemein verwendeten Verfahrens erzeugt. Planare Querschnitte der generierten Turbulenzfelder sind als eine Reihe der zeitlich und räumlich abhängigen Randbedingungen dem gestreckten unberührten Diffusionsrechengebiet eingeführt, und die Entwicklung der Turbulenz ist überwacht. Die oben beschriebenen Fälle der freien und räumlich eingeschränkten Diffusion sind in den Simulationen durch jeweils periodischen und perfekt gleitenden Randbedingungen an den lateralen Seiten des Rechengebiets unterscheidet. Die Simulationen der rotierenden Diffusion sind mittels den LES Gleichungen in einem rotierenden Referenzsystem durchgeführt. Die Arbeit behandelt die Kriterien, die für die Identifizierung der turbulenten Front aus LES Feldern praktisch anwendbar sind. Zudem werden die Ausbreitung der turbulenten Front und die dazugehörige Profile der turbulenten kinetischen Energie und der Wirbelstärke der aufgelösten LES Geschwindigkeit dargestellt und werden qualitativ mit den verfügbaren experimentellen und DNS Ergebnissen verglichen. Neben den Simulationsergebnissen die Grundbegriffe der Symmetrieanalyse der Evolutionsgleichungen des Zweipunktkorrelationstensors und das Verfahren zur Erzeugung der isotropen und homogenen, rotierenden Trubulenz sind beschrieben. Darüber hinaus werden auch die Characteristiken der Reynolds-Spannungsmodelle in den Fällen der turbulenten Diffusion analysiert.

Nomenclature

Abbreviations

confHitDiff	Large-eddy simulation of confined turbulent diffusion
DNS	Direct numerical simulation
FVM	Finite-volume method
HIT	Homogeneous-isotropic turbulence
hitDiff	LES of turbulent diffusion
LES	Large-eddy simulation
lesHit	Large-eddy simulation of homogeneous isotropic turbulence
LIF	Laser-induced fluorescence
OpenFOAM	Open Field Operation and Manipulation
PDE	Partial differential equation
PIV	Particle image velocimetry
RANS	Reynolds-averaged Navier-Stokes
rotHitDiff	Rotating turbulent diffusion case
TNTI	Turbulent/non-turbulent interface

Greek symbols

δ_{ij}	Kronecker delta, identity tensor
ϵ	Rate of dissipation of turbulent kinetic energy
ϵ_{ij}	Rate of dissipation of Reynolds stress tensor
ν	Kinematic viscosity
ν_t	Turbulent viscosity
ω_i	Vorticity
σ_ϵ	Rate of dissipation turbulent Prandtl number
σ_k	Turbulent kinetic energy turbulent Prandtl number
$\sigma_{\langle u_i u_j \rangle}$	Reynolds stress turbulent Prandtl number
τ	Characteristic time scale for TNTI propagation
τ_{ij}^R	Sub-grid or residual stress in LES
τ_{ij}^r	Anisotropic part of the residual stress in LES

Latin symbols

ℓ	Characteristic length scale for TNTI propagation
$\langle \mathbf{U}(\mathbf{x},t) \rangle$, $\langle \mathbf{U} \rangle$	Average (probability weighted) velocity field
$\langle P \rangle (\mathbf{x},t)$, $\langle P \rangle$	Average (probability weighted) effective pressure field
$\langle u_i u_j \rangle (\mathbf{x},t)$, $\langle u_i u_j \rangle$	Reynolds stress tensor
$\mathbf{U}(\mathbf{x},t)$, $\mathbf{U}$	Instantaneous velocity field
$\mathbf{u}(\mathbf{x},t)$, $\mathbf{u}$	Fluctuating velocity, average of which is identically zero
$\mathbf{u}'(\mathbf{x},t)$, $\mathbf{u}'$	Unresolved (sub-grid-scale) velocity field
$\mathbf{x}$	Position vector
$\mathcal{L}$	Characteristic length scale
$\mathcal{P}$	Production of turbulent kinetic energy
$\mathcal{P}_{ij}$	Production of Reynolds stress
$\mathcal{R}_{ij}$	Redistribution of Reynolds stress
$\mathcal{U}$	Characteristic velocity scale
$\overline{\mathbf{U}}(\mathbf{x},t)$, $\overline{\mathbf{U}}$	Resolved (filtered) velocity field
$\overline{\mathcal{S}}$	Magnitude of filtered rate of strain
$\overline{P}(\mathbf{x},t)$, $\overline{P}$	Filtered effective pressure field
$\overline{S}_{ij}$	Filtered rate of strain
e_{ijk}	Permutation symbol
f	Probability density function
$G(\mathbf{x},t)$, G	Filtering kernel
H, h	TNTI position
k	Turbulent kinetic energy
k_r	Residual kinetic energy in LES
L	Integral length scale of homogeneous isotropic turbulence
L_x, L_y, L_z	Dimensions of the computational domain
$P(\mathbf{x},t)$, P	Instantaneous effective pressure field, i.e. pressure including other potential functions divided by constant density
$p(\mathbf{x},t)$, p	Instantaneous pressure field; fluctuating effective pressure field
r_i	Two-point correlation separation coordinate
R_{ij}	Two-point correlation tensor
s_{ij}	Rate of strain of fluctuating velocity
T	Integral time scale of homogeneous isotropic turbulence
t	Time
T_{ijk}	Turbulent transport
y^*	Distance from TNTI; used in conditional averaging

Mathematical symbols

$(\cdot)^*$	Non-dimensional variable

$\langle \cdot \rangle$	Mathematical expectation
$\nabla \cdot$	Divergence operator
∇	Gradient operator
∇^2	Laplacian operator (divergence of a gradient)
$\otimes$	Outer product
$\overline{(\cdot)}$, $\widetilde{(\cdot)}$	Filtering operation

Dimensionless numbers

Re	Reynolds number
Ro	Rossby number

Contents

1. Introduction

The present thesis reports on simulations of spatial spreading of incompressible turbulent fluctuations of a fluid of constant and uniform density in a statistically unsteady and one-dimensional setting, where the turbulent motion is induced exclusively by a homogeneous planar source of energy. To facilitate the description of the problem of pure one-dimensional *turbulent diffusion*, this chapter gives an introduction to some of the phenomenological concepts developed in scientific and engineering studies of turbulent flows. Additionally, the principles of formal mathematical treatment of turbulent flows and some of the methods of their reduced-order modeling are outlined. The chapter concludes with a detailed account of the case of shear-free turbulent diffusion and a brief outline of the remainder of the thesis.

1.1. Turbulent flows

From observations it has been generally accepted that no rigorous definition can be given for turbulent flows. On the other hand, certain characteristics that characterize turbulent flows have been identified in order to distinguish them from the other observed fluid motions. Turbulent flows exhibit [68]:

- Irregularity, i.e. the velocity field $\mathbf{U}(\mathbf{x}, t)$ and the pressure field $p(\mathbf{x}, t)$ may be treated as time-dependent random fields [58].
- Diffusivity, i.e. in turbulent flows rates of transfer of momentum, heat and mass are significantly increased in comparison to relevant non-turbulent flows.
- The turbulent flow state invariably occurs at large Reynolds numbers, i.e.

$$\mathrm{Re} \equiv \frac{\mathcal{L}\mathcal{U}}{\nu} \tag{1.1}$$

  where $\mathcal{L}$ is the characteristic length scale of a flow, $\mathcal{U}$ is the characteristic velocity scale of a flow, and ν is the kinematic viscosity of fluid. The condition of large Re usually corresponds to a weak influence of ν.
- Energy dissipation, i.e. drag experienced by a bluff body or pressure drop in conduits/pipes are strongly increased in turbulent flows relative to non-turbulent or laminar flows.
- Three-dimensional vorticity fluctuations – turbulence is sustained by the mechanism of vortex stretching which does not exist unless the vorticity fluctuations are three-dimensional.

- Continuum – the smallest relevant scales in turbulent flows are in the vast majority of cases still orders of magnitude larger than the mean-free path of fluid molecules and therefore the continuity assumption remains accurate.

Turbulent flows appear as a consequence of the loss of stability of laminar flows as the Reynolds number is increased. They are characterized by a broad spectrum of relevant time and length scales, as exemplified by e.g. the energy content of the Fourier modes of an incompressible velocity field. The spectrum of scales is bounded from above by the characteristic length scale of the geometry of the flow, and from below by the action of viscosity which strongly damps motions below its characteristic scale.

1.2. Mathematical description of turbulent flows

It is generally accepted that motions of Newtonian fluids are accurately modeled by the Navier-Stokes equations. Under the assumption of incompressibility, and the assumption that the fields are differentiable, the Navier-Stokes equations reduce to

$$\frac{\partial U_i}{\partial x_i} = 0 \tag{1.2}$$

$$\frac{\partial U_i}{\partial t} + U_j \frac{\partial U_i}{\partial x_j} = -\frac{\partial P}{\partial x_i} + \frac{\partial}{\partial x_j}\left(\nu \frac{\partial U_i}{\partial x_j}\right) \tag{1.3}$$

where P is the effective pressure (the physical pressure scaled by density together with any potential forces which may act in a flow). In order to fully specify a fluid flow problem, initial and boundary conditions need to be specified.

Utilizing the identities in the calculus of vector fields and the continuity equation, various equivalent expressions for the nonlinear convective term may be derived [73]

- The convection form
$$U_j \frac{\partial U_i}{\partial x_j} \tag{1.4}$$

- The divergence form
$$\frac{\partial U_i U_j}{\partial x_j} \tag{1.5}$$

- The skew-symmetric form
$$\frac{1}{2} U_j \frac{\partial U_i}{\partial x_j} + \frac{1}{2} \frac{\partial U_i U_j}{\partial x_j} \tag{1.6}$$

- The rotation form
$$e_{ijk} \omega_j U_k + \nabla \left(\frac{1}{2} U_i U_i\right) \tag{1.7}$$

where ω_i is the vorticity field defined by

$$\omega_i \equiv e_{ijk}\frac{\partial U_k}{\partial x_j} \tag{1.8}$$

Particular form of the convective term is significant in the discretization of the equations as will be shown in the next chapter.

The incompressible Navier-Stokes equations have elementary analytical solutions only in simple cases, therefore to acquire information on velocity and pressure fields in a particular flow, measurements or computer simulations have to be performed. Numerical methods have been developed to completely solve for the velocity and pressure fields under various conditions. The principal difficulty when applying the present techniques of direct simulations or measurements to turbulent flows is that the existence of a wide spectrum of relevant time and length scales imposes for the majority of practical flow cases prohibitive requirements on measurement or computational equipment. Therefore, in order to be able to investigate turbulent flows reduced-order models have to be utilized.

1.2.1. Reynolds-averaged Navier-Stokes equations

The velocity field in a turbulent flow varies randomly, but its mathematical expectation, defined as [58]

$$\langle U_i(\mathbf{x},t)\rangle \equiv \iiint_{-\infty}^{\infty} V_i f(\mathbf{V},\mathbf{x},t)\mathrm{d}V_1\mathrm{d}V_2\mathrm{d}V_3 \tag{1.9}$$

where $\mathbf{V}$ is the sample-space variable, and $f(\mathbf{V},\mathbf{x},t)$ is the probability density function (PDF) of $\mathbf{U}$, is comparatively regular and predictable. The velocity fluctuation field may be defined as

$$u_i(\mathbf{x},t) \equiv U_i(\mathbf{x},t) - \langle U_i(\mathbf{x},t)\rangle \tag{1.10}$$

Utilizing linearity of the operator $\langle\cdot\rangle$ and eqs. (1.2) and (1.3) (see [58]) the mean-continuity equation reads

$$\frac{\partial \langle U_i\rangle}{\partial x_i} = 0 \tag{1.11}$$

and the mean-momentum equation then becomes

$$\frac{\partial \langle U_i\rangle}{\partial t} + \langle U_j\rangle \frac{\partial \langle U_i\rangle}{\partial x_j} = -\frac{\partial \langle P\rangle}{\partial x_i} + \frac{\partial}{\partial x_j}\left(\nu\frac{\partial \langle U_i\rangle}{\partial x_j}\right) - \frac{\partial \langle u_i u_j\rangle}{\partial x_j} \tag{1.12}$$

where $\langle u_i u_j\rangle$ is the Reynolds stress (scaled by density). The Reynolds-Averaged Navier-Stokes (RANS) equations differ from their non-averaged counterpart by the divergence of the Reynolds stress. The challenge of turbulence modelling is to express this term in as a function of known quantities in order to close the system of equations.

1.2.2. Large-eddy simulation equations

Another way to reduce the number of degrees of freedom in a mathematical model of a turbulent flow is to consider the dynamics of low-pass filtered variables. The rationale

for such an attempt is the observation that low-frequency components of turbulent velocity fields exhibit a strong dependence on specific flow configurations (flow geometry and boundary conditions), while, in principle, the high-frequency components lend themselves to simplified descriptions because of their nearly universal behavior. Formally, one proceeds by defining a low-pass filtered velocity field, termed resolved or grid-scale velocity, as

$$\overline{U}_i(\mathbf{x},t) \equiv \int_\Omega G(\mathbf{y}-\mathbf{x},\Delta)\, U_i(\mathbf{x},t)\,\mathrm{d}\mathbf{y} \tag{1.13}$$

where $G(\mathbf{x},\Delta)$ is a filtering kernel of width Δ, with the normalization property

$$\int_\Omega G(\mathbf{x},\Delta) = 1 \tag{1.14}$$

and Ω is the flow domain under consideration. The subgrid-scale or unresolved velocity field is now defined as

$$u_i'(\mathbf{x},t) \equiv U_i(\mathbf{x},t) - \overline{U}_i(\mathbf{x},t) \tag{1.15}$$

Under the assumption of commutativity between the filtering and differentiation operators, which amounts to the filtering kernel G being independent of the position vector $\mathbf{x}$ the evolution equations for the filtered variables may be derived (see [58]). The filtered momentum equation reads

$$\frac{\partial \overline{U}_i}{\partial t} + \overline{U}_j \frac{\partial \overline{U}_i}{\partial x_j} = -\frac{\partial \overline{P}}{\partial x_i} + \frac{\partial}{\partial x_j}\left(\nu \frac{\partial \overline{U}_i}{\partial x_j}\right) - \frac{\partial \tau_{ij}^R}{\partial x_j} \tag{1.16}$$

and the filtered continuity equation is

$$\frac{\partial \overline{U}_i}{\partial x_i} = 0 \tag{1.17}$$

Here, τ_{ij}^R, the sub-grid or residual stress, is the additional stress tensor which arises due to the effect of the missing unresolved velocities. Formally,

$$\tau_{ij}^R \equiv \overline{U_i U_j} - \overline{U}_i \overline{U}_j \tag{1.18}$$

The objective of LES modeling is to develop adequate parametrizations of the sub-grid stress τ_{ij}^R.

1.3. One-dimensional propagation of turbulence

The problem considered in this study is the propagation of turbulent motions from a planar source of energy into a semi-infinite body of fluid without mean velocity gradients. At the level of the one-point, second-order velocity moments this condition corresponds to a zero mean rate of production of turbulent stresses by the mean rate of strain.

The simplicity of the motion is one of the prime reasons for the attention it has received in the past. It represents one of the simplest departures to inhomogeneity and anisotropy from the thoroughly studied case of homogeneous, isotropic turbulence (HIT). The relevance of this case has been recognized in several practical contexts as well, e.g. turbulence at the air-water interface, determination of the empirical constants in the two-equation, $k-\epsilon$-type

models, in atmospheric and geophysical turbulence investigations, to name a few (e.g. Lele [45], Hopfinger et al. [31, 32], Holzner et al. [28, 29]).

The fluid motion in this setting can be described as partially turbulent. It gives rise to the concept of the turbulent-non-turbulent interface (TNTI) which separates the vortical, turbulent region from the essentially irrotational non-turbulent region, which is, however, not completely void of the velocity fluctuations. The TNTI is a thin, spatially and temporaly irregular layer. It propagates into the turbulent region by the entrainment process. It has been established that the prevailing mechanism responsible for the entrainment is the small-scale "nibbling", as opposed to the large-scale "engulfment" process (Westerweel et al. [71], Mathew and Basu [50]).

Oberlack and Guenther [56] have applied the method of symmetry analysis of differential equations (c.f. appendix A) to the equations governing the two-point correlation of velocity, defined by

$$R_{ij}(\mathbf{x}, \mathbf{r}, t) \equiv \langle u_i(\mathbf{x}, t) u_j(\mathbf{x} + \mathbf{r}, t) \rangle \tag{1.19}$$

The analysis has been carried out by utilizing an asymptotic expansion of R_{ij} in the $\mathbf{r}$-space, thereby avoiding the influence of the viscosity on the large scales and recovering an additional scaling symmetry present in the Euler equations. It has been shown that the analysis and the results are entirely applicable to the multi-point statistical correlations of arbitrary order. The analysis has revealed new *similarity solutions* (*scaling laws*) which are manifestations of particular broken symmetries admitted by the original system.

The analysis firstly recovers the classical, *diffusion-like, heat-equation-like*, solution in the case that all the symmetries are valid. This similarity solution is characterized by a power-law decay of the turbulent kinetic energy with the distance from the forcing plane, $(x/\ell)^{-n}$, in the limit $t \to \infty$ and the linear growth of the integral length scale with (x/ℓ) (ℓ represents a characteristic length scale). The propagation of the TNTI has been shown to take place according to

$$H\left(t\right)/\ell \sim \left[\left(t - t_0\right)/\tau\right]^m \tag{1.20}$$

where $H\left(t\right)$ is the distance of the TNTI from the forcing plane, τ is a timescale and t_0 is a temporal virtual origin (Hopfinger et al. [32]).

The second similarity solution, the *decelerating diffusion-wave* solution, is obtained by considering the symmetry breaking of scaling of space. The turbulent kinetic energy now exhibits an exponential decay with the distance from the grid, $\exp\left(-(x/\ell)\right)$, in the steady state limit and the integral length scales are invariant with respect to distance from the source. The TNTI propagates according to

$$H\left(t\right)/\ell \sim \ln\left[\left(t - t_0\right)/\tau\right] \tag{1.21}$$

Similar theoretical and experimental results have been obtained recently, albeit in the setting of isotropic turbulence. In the experiments utilizing multiscale, fractal grids in a wind tunnel to create an isotropic turbulent field, Hurst and Vassilicos [34] have discovered regions with an exponential decay of turbulence and constant integral length scales. George and Wang [19] have analyzed the similarity solutions to the energy equation in the spectral space and recovered an exponential temporal decay of turbulence when the (integral) length scales are kept constant. Risso and Fabre [60] studied a confined jet flow, a turbulent round jet issuing in a pipe closed on one end, and with a narrow slit coplanar and concentric with

the jet nozzle on the other end. The configuration forces the jet mean flow to reverse and exit at the slit, thereby leaving in the far-field a region without mean flow governed by turbulent diffusion. The results showed that the Reynolds stresses decay exponentially in the diffusive region and that the length scales are constant. The DNS study performed by Godeferd and Lollini [26] on artificially forced confined diffusive turbulence indicated similar results (see section 4.2).

An additional similarity solution is obtained by introducing constant system rotation Ω with the axis perpendicular to the forcing plane, thereby introducing the timescale $1/\Omega$ to the system. The turbulent kinetic energy has been shown to decay according to $(x/\ell)^{-2}$ and the TNTI asymptotically approaches the maximum propagation distance

$$H\left(t\right)/\ell \sim \exp\left[-\left(t-t_0\right)/\tau\right] \tag{1.22}$$

This case has been investigated mainly in the steady state limit, and several characteristics of the turbulent field have been emphasized, e.g. change from nearly isotropic turbulence to the quasi two-component turbulence with the distance to the grid, the appearance of coherent vortices which are aligned with the axis of rotation, the interaction of inertial waves and turbulent motions, the modulation of the energy spectrum by rotation, etc. (e.g. Dickinson and Long [12], Hopfinger et al. [32], Godeferd and Lollini [26], Staplehurst et al. [64]).

1.4. Outline

The remainder of this thesis proceeds as follows. In chapter 2, some aspects of modeling of turbulent flows in the framework of RANS and LES are reviewed. Additionally, the behaviour of various RANS models is presented in the present case of statistically one-dimensional and unsteady configuration. Chapter 3 lists numerical methods employed and requirements on these methods imposed by the physics being treated. In chapter 4 the results of LES simulations of the shear-free turbulent diffusion are presented. Conclusions and ideas for future work are listed in chapter 5. Appendix A gives some details about the symmetry analysis method from which the present work is derived. In Appendix B the forcing method used in the generation of turbulence is explained.

2. Turbulence modeling

This chapter presents approaches to modeling of the apparent turbulent stresses in the framework of RANS and LES. In addition to the presentation of conventional modeling approaches solutions are given to several RANS models in the setting of one-dimensional unsteady turbulent diffusion. Counterparts to these solutions in the LES mode will be given in the following chapter.

2.1. RANS models

The approaches to modeling the Reynolds stress in the transport equation for mean momentum span a wide range in their complexity and generality of predictions (see [58] and [44]). For the present purpose of gaining insight into the behavior of the turbulence statistics in the case of pure turbulent diffusion the two most developed and widely applied modeling approaches will be examined

- The Reynolds-stress transport modeling (RSTM) where model equations are solved for the Reynolds-stress components, and
- The two-equation eddy-viscosity models which are based on the turbulent-viscosity hypothesis, originaly proposed by Boussinesq [4], that the Reynolds stress is related to the mean rate of strain by

$$\langle u_i u_j \rangle = -\nu_t \left(\frac{\partial \langle U_i \rangle}{\partial x_j} + \frac{\partial \langle U_j \rangle}{\partial x_i} \right) + \frac{2}{3} k \delta_{ij} \tag{2.1}$$

  Here, the eddy-viscosity ν_t is modeled by approximating it, on dimensional grounds, as a product of characteristic length and velocity scales. The velocity scale of turbulence is usually given as a square root of the turbulent kinetic energy, $k^{1/2}$, and the length scale is calculated from k and a scale-supplying variable such as the rate of dissipation of the turbulent kinetic energy ϵ or similar variables.

The equation governing behavior of the Reynolds stress, may be derived from the Navier-Stokes equations utilizing the properties of averaging (see [58]). The Reynolds-stress equation reads

$$\frac{\partial \langle u_i u_j \rangle}{\partial t} + \langle U_k \rangle \frac{\partial \langle u_i u_j \rangle}{\partial x_k} + \frac{\partial T_{kij}}{\partial x_k} = \mathcal{P}_{ij} + \mathcal{R}_{ij} - \epsilon_{ij} \tag{2.2}$$

where, besides the rate of change and the convection terms the following terms arise

- The Reynolds-stress production by gradients of mean velocity

$$\mathcal{P}_{ij} \equiv - \langle u_i u_k \rangle \frac{\partial \langle U_j \rangle}{\partial x_k} - \langle u_j u_k \rangle \frac{\partial \langle U_i \rangle}{\partial x_k} \tag{2.3}$$

- The Reynolds-stress transport

$$T_{kij} \equiv \langle u_i u_j u_k \rangle - \nu \frac{\partial \langle u_i u_j \rangle}{\partial x_k} + \langle u_i p \rangle \delta_{kj} + \langle u_j p \rangle \delta_{ik} \tag{2.4}$$

  which is usually modeled by (Daly and Harlow [11])

$$\left(\nu \delta_{kl} + C_S \frac{k}{\epsilon} \langle u_k u_l \rangle \right) \frac{\partial \langle u_i u_j \rangle}{\partial x_l} \tag{2.5}$$

  or in a simpler manner by augmenting kinematic viscosity with eddy-viscosity

$$\left(\nu + \frac{\nu_t}{\sigma_{\langle u_i u_j \rangle}} \right) \frac{\partial \langle u_i u_j \rangle}{\partial x_k} \tag{2.6}$$

- The pressure-rate-of-strain correlation

$$\mathcal{R}_{ij} \equiv \left\langle p \left(\frac{\partial u_i}{\partial x_j} + \frac{\partial u_j}{\partial x_i} \right) \right\rangle \tag{2.7}$$

  A linear model for the redistribution term (see e.g. Gibson and Launder [23]) is given by

$$-C_1 \epsilon a_{ij} - C_2 \left(\mathcal{P}_{ij} - \frac{1}{3} \mathcal{P}_{kk} \delta_{ij} \right) \tag{2.8}$$

  where a_{ij} is the Reynolds stress anisotropy tensor, defined as

$$a_{ij} \equiv \frac{\langle u_i u_j \rangle}{\langle u_k u_k \rangle} - \frac{1}{3} \delta_{ij} \tag{2.9}$$

- The Reynolds-stress dissipation

$$\epsilon_{ij} \equiv 2\nu \left\langle \frac{\partial u_i}{\partial x_k} \frac{\partial u_j}{\partial x_k} \right\rangle \tag{2.10}$$

  which is, in off-wall regions, modeled by (Rotta [61])

$$\epsilon_{ij} = \frac{2}{3} \epsilon \delta_{ij} \tag{2.11}$$

The pressure-rate-of-strain, turbulent and pressure transport and the dissipation correlation require modeling. The models for the first two terms are given along their with their definitions. Here the definitions are simplified in comparison with the formal model specification (which may be found in the original publications and several well known texts, e.g. Pope [58]). The simplification is achieved by avoiding any modeling terms which deal with various aspects of turbulence near rigid surfaces, as these are of no relevance in the present context.

The equation for the turbulent kinetic energy k may be derived by contracting eq. (2.2) (and multiplying it by 1/2)

$$\frac{\partial k}{\partial t} + \langle U_j \rangle \frac{\partial k}{\partial x_j} = -\frac{\partial T_i}{\partial x_i} + \mathcal{P} - \epsilon \tag{2.12}$$

where

- The transport of the turbulent kinetic energy is

$$T_i \equiv \frac{1}{2} \langle u_i u_j u_j \rangle + \langle u_i p \rangle - 2\nu \langle u_j s_{ij} \rangle \tag{2.13}$$

where the fluctuating rate of strain s_{ij} is defined as

$$s_{ij} \equiv \frac{1}{2} \left(\frac{\partial u_i}{\partial x_j} + \frac{\partial u_j}{\partial x_i} \right) \tag{2.14}$$

The transport term in eq. (2.13) is commonly modeled by

$$\frac{\nu_t}{\sigma_k} \frac{\partial k}{\partial x_j} \tag{2.15}$$

- The production of the turbulent kinetic energy is

$$\mathcal{P} \equiv - \langle u_i u_j \rangle \frac{\partial \langle U_i \rangle}{\partial x_j} \tag{2.16}$$

- The rate of dissipation of the turbulent kinetic energy is

$$\epsilon \equiv 2\nu \langle s_{ij} s_{ij} \rangle \tag{2.17}$$

Common practice in modeling the rate of dissipation is to represent its behavior with an advection-diffusion equation accompanied by appropriate source terms, which does not stem from the exact equation for the rate of dissipation. The common form of the equation for the rate of dissipation of the turbulent kinetic energy reads

$$\frac{\partial \epsilon}{\partial t} + \langle U_i \rangle \frac{\partial \epsilon}{\partial x_i} = \frac{\partial}{\partial x_j} \left[\frac{\nu_t}{\sigma_\epsilon} \frac{\partial \epsilon}{\partial x_j} \right] + C_{\epsilon 1} \frac{\mathcal{P} \epsilon}{k} - C_{\epsilon 2} \frac{\epsilon^2}{k} \tag{2.18}$$

2.1.1. Turbulent diffusion within the RANS framework

The equations have been solved for the case of turbulent diffusion. The computational domain is a slab of cells with fixed boundaries for k, ϵ or $\langle u_i u_j \rangle$ on one side and zero-gradient boundary conditions at the far boundary. Sides of the computational domain have been represented as zero-gradient boundaries.

The case has been studied in Cazalbou and Chassaing [7, 8], Cazalbou et al. [9] and Straatman [66], Straatman et al. [67]. The focus of these studies has been the structure of the solutions to the model equations at TNTI in steady state and at high Reynolds number for various well-known closures for the turbulent transport term. Structure of solutions has not been defined strictly, but these studies assume that the Reynolds-stress anisotropy is the governing parameter for determining the structure. Parameters which influence the structure have been identified to be the modeling coefficients and the free-stream turbulence level. Notably, Cazalbou and Chassaing [7] deal in part with the unsteady problem of turbulent diffusion from a planar source. They have found that there needs to be a distinction between the behavior of turbulence statistics at short times (in comparison to

the turbulence time scale introduced at the source) where the evolution is governed by the parameters at the boundary. On the other hand, at large times turbulence statistics are found to be governed by time-dependent characteristic scales, which are governed by a steady set of equations at the instantaneous location of the TNTI. For short times, they conclude that the only self-similar solution of the two-equation model-equations system in which turbulence quantities are allowed to depend only on the local levels of the turbulent kinetic energy and its rate of dissipation are the power-law solutions. From the solution to the model system of equations they derive the equation for the linear growth of the integral length scale as turbulence propagates from its source. It has been shown that a suitable choice of model coefficients may produce turbulence with a constant length scale, and that in this case the decay of the turbulent kinetic energy and the dissipation rate proceeds exponentially. It is important to note here that in these investigations only the model transport equations have been investigated without addressing how such turbulence might be reliably created.

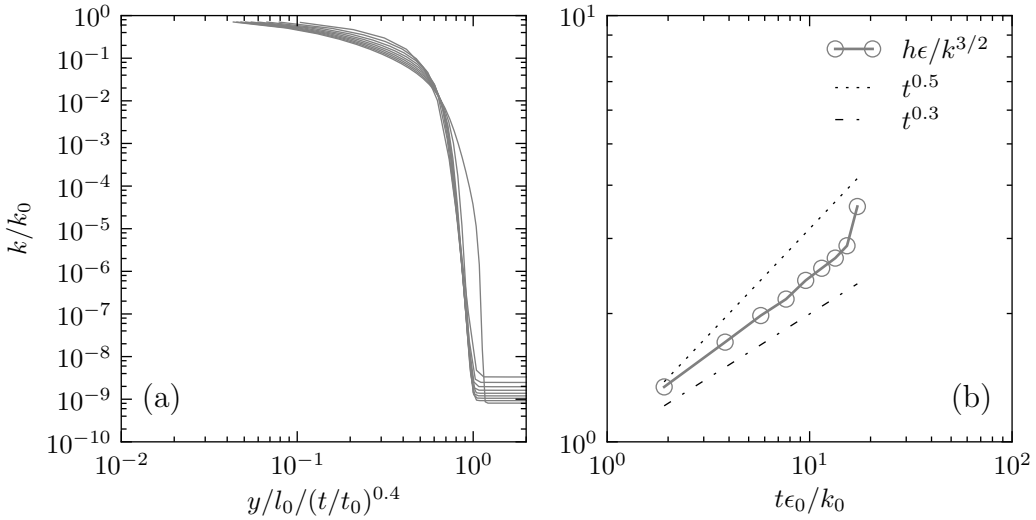

Figure 2.1.: (a) Profiles of turbulent kinetic energy for the standard k-ϵ model in similarity coordinates (the model consists of eqs. (2.12) and (2.18)). The coefficients of the model are $C_\mu = 0.09$, $C_{\epsilon 1} = 1.44$, $C_{\epsilon 2} = 1.92$, $\alpha_k = 1/\sigma_k = 1$ and $\alpha_\epsilon = 1/\sigma_\epsilon = 0.76923$. (b) TNTI propagation

The following results build upon the work discussed above in a way that they show how the TNTI might be detected from the solution and its behavior. It has been shown in Appendix A that for a self-similar (linear) diffusion problem the profiles of the diffusing quantity do not exhibit a step-like fall of the quantity at the front and that the propagation trend is governed by the definition of the similarity variable (i.e., arbitrary selections of the criterion for the front position are different only by a constant factor). It has been generally accepted that vorticity is the discriminating quantity between the turbulent and non-turbulent regions, see e.g. [30, 33].

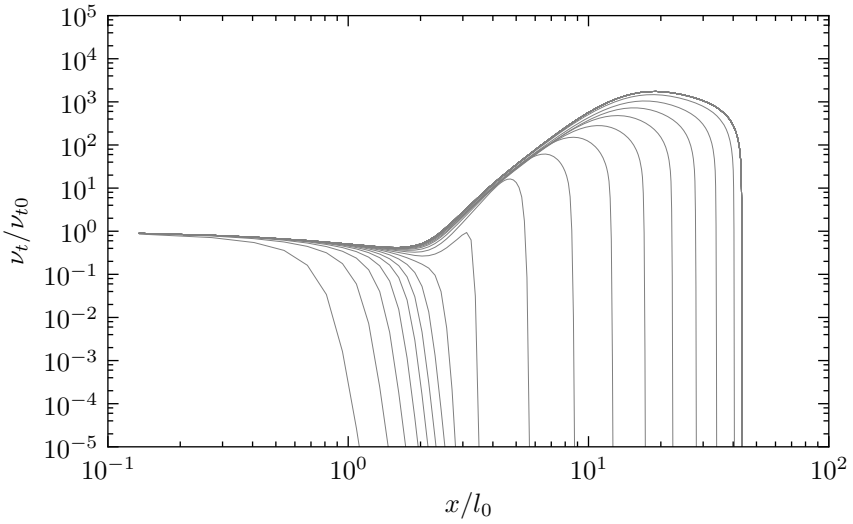

Figure 2.2.: Profiles of turbulent viscosity for the k-ϵ model (see fig. 2.1).

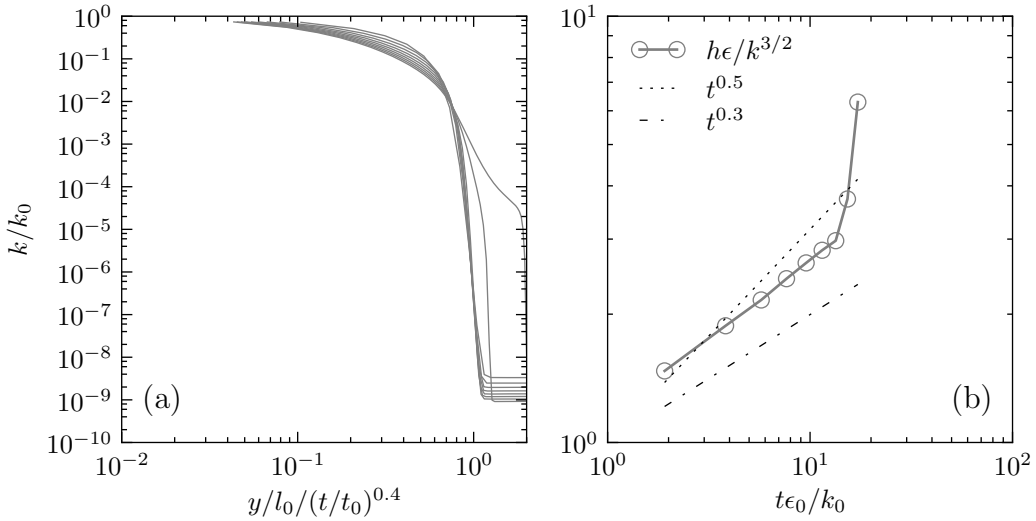

Figure 2.3.: (a) Profiles of turbulent kinetic energy for the Gibson-Launder model in similarity coordinates (the model consists of eqs. (2.2) and (2.18) with the turbulent transport modeled by eq. (2.6)). The coefficients of the model are $C_\mu = 0.09$, $C_{\epsilon 1} = 1.44$, $C_{\epsilon 2} = 1.92$, $\alpha_{\langle u_i u_j \rangle} = 1/\sigma_{\langle u_i u_j \rangle} = 1.22$ and $\alpha_\epsilon = 1/\sigma_\epsilon = 0.76923$. (b) TNTI propagation.

The first case, shown in fig. 2.1 is a solution of the standard k-ϵ model. Figure 2.1 (a) shows that the profiles for different times collapse well for the power-law exponent 0.4 and that the TNTI, fig. 2.1 (b) propagates accordingly. The sudden change of TNTI propagation slope is attributed to the increased eddy-viscosity as shown in fig. 2.2. This change is

dependent on the specification of the initial 'free-space' values of k and ϵ, i.e. it is not universal. Nevertheless, one may conclude that the model is compatible with the power-law propagation of turbulence.

The second case, TNTI propagation with the Gibson-Launder RSTM model, is depicted in fig. 2.3. The velocity-pressure-gradient term does not play a role as the initial conditions are an isotropic decomposition of the k-ϵ case.

Figure 2.4 shows turbulent diffusion results for the Launder-Shima RSTM model. The model consists of a set of equations similar to eqs. (2.2) and (2.18) and here only the differences will be described:

- $C_{\epsilon 1}$ is no longer a model constant. It is given by

$$C_{\epsilon 1} = 1.45 + \Psi_1 + \Psi_2 \tag{2.19}$$

  where

$$\Psi_1 = 2.5A\frac{\mathcal{P}}{\epsilon} - 1 \tag{2.20}$$

  and

$$\Psi_2 = 0.3\left(1 - 0.3A_2\right)\exp\left(0.002\mathrm{Re}_t\right) \tag{2.21}$$

  Here $A_2 = a_{ij}a_{ij}$ and $A_3 = a_{ij}a_{jk}a_{ki}$ are the invariants of the anisotropy tensor a_{ij} and $A = 1 - 9/8\left(A_2 - A_3\right)$ is the flatness parameter. The Reynolds number of turbulence, Re_t, is given by $\mathrm{Re}_t = k^2/\left(\epsilon\nu\right)$.

- The equation for the dissipation rate is given by

$$\frac{\partial \epsilon}{\partial t} + \langle U_i \rangle \frac{\partial \epsilon}{\partial x_i} = \frac{\partial}{\partial x_j}\left[\left(\nu\delta_{jk} + C_\epsilon \frac{k}{\epsilon}\langle u_k u_j \rangle\right)\frac{\partial \epsilon}{\partial x_k}\right] + C_{\epsilon 1}\frac{\mathcal{P}\epsilon}{k} - C_{\epsilon 2}\frac{\epsilon\tilde{\epsilon}}{k} \tag{2.22}$$

  where $\tilde{\epsilon} = \epsilon - 2\nu\left(\partial k/\partial x_i\right)^2$ is introduced in order to enable zero-valued wall boundary condition on ϵ (see e.g. [44]).

Similar to the previous case, results are not affected by the velocity/pressure-gradient correlation. However, turbulent diffusion model in eq. (2.5) exhibits similar propagation trends to the previous two cases.

The tests have shown that current one-point closures are compatible with the first scaling law of Oberlack and Guenther [56]. The propagation of the TNTI is determined based on the turbulence scales and is a good indicator for the requirements of the computational domain size and the time span which is to be used in the LES runs shown in the next chapter. Cazalbou and Chassaing [7] have shown that a suitable combination of constants is required for the k-ϵ model in order to obtain a constant length scale solution.

2.2. LES models

LES modeling concerns itself with the methods of expressing the sub-grid stress tensor τ_{ij}^R in terms of the filtered velocity field $\overline{U}_i$. Formally, τ_{ij}^R may be defined by eq. (1.18). The residual stress energy is defined as

$$k_r \equiv \frac{1}{2}\tau_{ii}^R \tag{2.23}$$

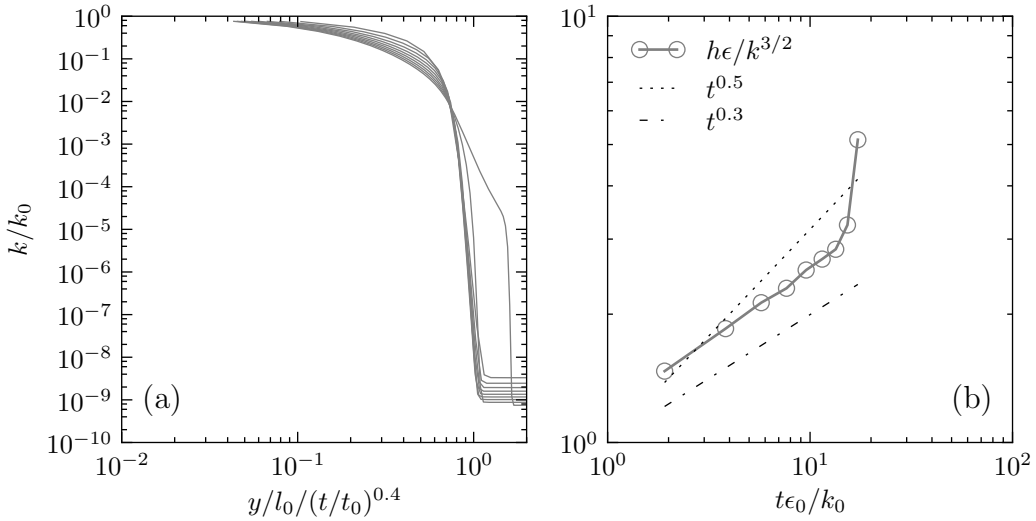

Figure 2.4.: (a) Profiles of turbulent kinetic energy for the Launder-Shima RSTM model in similarity coordinates (the model consists of eqs. (2.2) and (2.22) with the turbulent transport of $\langle u_i u_j \rangle$ modeled by eq. (2.5)). The coefficients of the model are $C_\mu = 0.09$, $C_{\epsilon 2} = 1.90$, $C_S = 0.22$ and $C_\epsilon = 0.18$, where $C_{\epsilon 1}$ is given by eq. (2.19). (b) TNTI propagation.

and the anisotropic residual-stress tensor is defined by

$$\tau_{ij}^r \equiv \tau_{ij}^R - \frac{2}{3} k_r \delta_{ij} \tag{2.24}$$

The isotropic part of the residual stress is usually lumped into the effective filtered pressure and the equation for filtered momentum features divergence of the anisotropic part of the sub-grid-stress tensor only.

2.2.1. The Smagorinsky model

The most common approach to modeling τ_{ij}^r is the eddy-viscosity approach, i.e.

$$\tau_{ij}^r = -2\nu_r \overline{S}_{ij} \tag{2.25}$$

where, on dimensional grounds, the eddy-viscosity of the residual motions may be modeled as

$$\nu_r = \ell_S^2 \overline{\mathcal{S}} = (C_S \Delta)^2 \, \overline{\mathcal{S}} \tag{2.26}$$

and the characteristic filtered rate of strain is defined as

$$\overline{\mathcal{S}} \equiv \left(2 \overline{S}_{ij} \overline{S}_{ij} \right)^{1/2} \tag{2.27}$$

The Smagorinsky length scale ℓ_S is given in terms of the filter width Δ and the Smagorinsky coefficient C_S.[1]

2.2.2. The dynamic procedure

Experience has shown that the Smagorinsky coefficient C_S must assume different values in different flows. The dynamic procedure, proposed by Germano et al. [21], is a means of calculating the coefficient C_S from quantities available in a flow. The procedure introduces a test filter with the filter width $\widetilde{\Delta}$ which is larger (typically two times) than the original (grid) filter $\overline{\Delta}$. It is worth noting that the test-filtered velocity field may formally be expressed in two equivalent ways, namely by test-filtering the instantaneous velocity field U_i, or by test-filtering the resolved velocity field $\overline{U}_i$, i.e.

$$\widetilde{U}_i = \widetilde{\overline{U}}_i \tag{2.28}$$

The sub-grid stress arising from the test filter is

$$T_{ij} \equiv \widetilde{\overline{U_i U_j}} - \widetilde{\overline{U}}_i \widetilde{\overline{U}}_j \tag{2.29}$$

The Germano identity (see Germano [20])is given by the following equation

$$\mathcal{L}_{ij} \equiv T_{ij} - \widetilde{\tau}^r_{ij} = \widetilde{\overline{U}_i \overline{U}_j} - \widetilde{\overline{U}}_i \widetilde{\overline{U}}_j \tag{2.30}$$

where eqs. (1.18) and (2.28) have been used for simplification. The significance of eq. (2.30) lies in the fact that the resolved stress $\mathcal{L}_{ij}$ is given in terms of $\overline{U}_i$.

2.2.3. The dynamic Smagorinsky model

The Smagorinsky model for the grid filter may be written as

$$\tau^r_{ij} = -2c_S \overline{\Delta}^2 \overline{\mathcal{S}}\, \overline{S}_{ij} \tag{2.31}$$

Analogously, for the test filter

$$T^d_{ij} \equiv T_{ij} - \frac{1}{3} T_{kk} \delta_{ij} = -2c_S \widetilde{\overline{\Delta}}^2 \widetilde{\overline{\mathcal{S}}}\, \widetilde{\overline{S}}_{ij} \tag{2.32}$$

Now, if c_S is taken to be constant we obtain the following overdetermined equation

$$\mathcal{L}^S_{ij} \equiv T^d_{ij} - \widetilde{\tau}^r_{ij} = c_S M_{ij} \tag{2.33}$$

where

$$M_{ij} \equiv 2\overline{\Delta}^2 \widetilde{\overline{\mathcal{S}} \overline{S}_{ij}} - 2\widetilde{\overline{\Delta}}^2 \widetilde{\overline{\mathcal{S}}}\, \widetilde{\overline{S}}_{ij} \tag{2.34}$$

The solution to eq. (2.33) which minimizes the mean-square error component-wise is given by Lilly [46]

$$c_S = \frac{M_{ij} \mathcal{L}_{ij}}{M_{kl} M_{kl}} \tag{2.35}$$

[1] The value of C_S may be derived by considering the behavior of the Smagorinsky model in the Kolmogorov inertial range [58].

Using the value of c_S according to the above equation in simulations has been shown not to be robust enough, i.e. they become numerically unstable. Several procedures to improve on the robustness of the dynamic procedure have been proposed. One way is to average the coefficient in homogeneous directions. This procedure has been employed for LES of HIT in the present study. Another approach is to clip the negative values of c_S to zero, thereby avoiding negative turbulent viscosity and inhibiting the back-scatter of energy associated to it.[2] The latter procedure has been employed in the present LES of turbulent diffusion.[3]

[2] This procedure has been implemented in OpenFOAM by the group at the Lehrstuhl für Technische Thermodynamik of the Universität Rostock, and made available under the public code repository at https://janus.fms.uni-rostock.de/svn/repository/OpenFOAM/trunk/LTTRostockExtensions (exact date of access is unknown). Further information on the model implementation may be found under http://powerlab.fsb.hr/ped/kturbo/openfoam/WorkshopZagrebJan2006/KrogerUniRostock.pdf, accessed on October, 2010.

[3] Averaging across homogeneous directions has not been used as the unstructured parallel code, combined with domain decomposition based on optimal graph partitioning techniques, does not ensure straightforward introduction of the concept of homogeneous layer of cells required for simple implementation of parallel averaging.

3. Numerical method

The simulations presented in this study have been performed with OpenFOAM®[1], a freely available computational continuum mechanics toolbox [47, 70]. In the ensuing sections the numerical method implemented in OpenFOAM® will be described. Additionally, its characteristics relevant for the present work will be highlighted.

3.1. Finite-volume method

The finite-volume method (FVM) is a numerical procedure designed to discretize differential equations in integral form. It is especially suited for applications to PDEs modeling conservation laws as the construction of the method implicitly ensures conservation of a dependent variable at the discrete level. This section is a summary of statements about FVM, further discussions on the topic may be found in [37, 38, 48, 49].

To facilitate the description it is convenient to state a general conservation equation in integral form for a scalar conserved quantity ϕ as

$$\frac{\partial}{\partial t}\int_{\Omega}\phi \mathrm{d}V + \oint_{\partial\Omega}\phi\mathbf{U}\cdot\mathrm{d}\mathbf{S} = \oint_{\partial\Omega}\Gamma\nabla\phi\cdot\mathrm{d}\mathbf{S} + \int_{\Omega}S\mathrm{d}V \tag{3.1}$$

where $\mathbf{U}$ is a velocity field, Γ is a diffusion coefficient and S is a volumetric source term. The equation is defined on the volume $\mathbf{x}\in\Omega$ with the closed boundary $\mathbf{x}\in\partial\Omega$ and the time interval $t\in(0,T]$. To fully specify a numerical simulation problem, boundary conditions at $\partial\Omega$ and initial conditions within Ω at $t=0$ should be added. Equation (3.1) describes evolution of the conserved quantity ϕ within the volume Ω, stating that the rate of change of ϕ within Ω is equal to the net flux of ϕ by convection and diffusion through $\partial\Omega$ and the net source of ϕ within Ω.

In the present FVM volume Ω is subdivided into a collection of N non-overlapping polyhedral volumes V_i with closed boundaries ∂V_i (throughout the section $i=\overline{0,N-1}$). A boundary ∂V_i for a polyhedral cell is, in turn, a union of planar faces, each of which is characterized by a vector $\mathbf{S}$, where the magnitude of $\mathbf{S}$ equals to the area of the face and its direction is along the unit normal vector to the surface of the face $\mathbf{n}$. Furthermore, it is convenient to discriminate between the faces on the boundary of the domain of interest $\partial\Omega$ and the faces within the volume Ω, labeling them as boundary and internal faces respectively. It is also worth noting that this tessellation of the domain implies that every internal face has two neighboring control volumes, and every boundary face neighbors one control volume. It may be shown that eq. (3.1) is equally valid for the control volumes V_i separately.

[1] OpenFOAM® is a registered trade mark of OpenCFD Limited, the producer of the OpenFOAM software.

The present FVM approximates solutions to eq. (3.1) at the centroids of control volumes V_i, where for a particular volume V_P its centroid $\mathbf{x}_P$ is implicitly defined by the equation

$$\int_V (\mathbf{x} - \mathbf{x}_P) \mathrm{d}V = 0 \tag{3.2}$$

The discretization of eq. (3.1) is a procedure for approximating the mathematical operators (integrals, divergence, curl, etc.) in the equation in terms of ϕ_i, the values of the dependent variable ϕ at the centroids of the control volumes V_i. The procedure renders eq. (3.1) into a system of N algebraic equations in terms of the unknowns ϕ_i, geometric quantities and known physical properties of materials which may be written as

$$\left(\left[A_P^\phi\right] + \left[A_N^\phi\right]\right)[\phi_P] = \left[b_P^\phi\right] \tag{3.3}$$

Here, the brackets signify that the terms represent matrices, where

- $\left[A_P^\phi\right]$ is a diagonal $N \times N$ matrix,
- $\left[A_N^\phi\right]$ is a $N \times N$ matrix consisting of off-diagonal elements,
- $[\phi_P]$ is a column matrix of unknown values of ϕ_P at control volume centroids, and
- $\left[b_P^\phi\right]$ is a column matrix of source terms.

Equation (3.3) may be further subdivided into

$$\left(\left[A_P^\phi\right]_{int} + \left[A_P^\phi\right]_{bou} + \left[A_N^\phi\right]\right)[\phi_P] = \left[b_P^\phi\right]_{int} + \left[b_P^\phi\right]_{bou} \tag{3.4}$$

This decomposition reflects the fact that the boundary conditions, in general, update the diagonal and source coefficients of the algebraic equation system.

A satisfactory compromise among requirements of handling geometric complexity, accuracy of approximations to mathematical operators and software implementation has been found to be the assumption of linear variation of the dependent variable ϕ in space within a small enough volume V surrounding a point $\mathbf{x}_0$. The assumption may be stated as

$$\phi(\mathbf{x}, t) \approx \phi(\mathbf{x}_0, t) + (\mathbf{x} - \mathbf{x}_0) \cdot \nabla\phi(\mathbf{x}_0, t) \tag{3.5}$$

This assumption renders the method second-order accurate, as the leading truncated term in the Taylor series expansion of ϕ about the point $\mathbf{x}_0$ is proportional to the square of the distance $(\mathbf{x} - \mathbf{x}_0)$. Taking eq. (3.5) into account, a volume integral of the dependent variable ϕ within the control volume V_P is, after algebraic manipulations, given by

$$\int_V \phi(\mathbf{x}, t) \mathrm{d}V \approx \phi(\mathbf{x}_P, t) V_P \tag{3.6}$$

and a surface integral along the bounding surface ∂V_P by

$$\oint_{\partial V_P} \mathrm{d}\mathbf{S}\phi(\mathbf{x}, t) \approx \sum_f \mathbf{S}_f \phi(\mathbf{x}_f, t) \tag{3.7}$$

where the decomposition of ∂V_P into a union of planar faces has been assumed here. Similarly to the volume centroid, the face centroid $\mathbf{x}_f$ is defined as

$$\int_S (\mathbf{x} - \mathbf{x}_f) \mathrm{d}S = 0 \tag{3.8}$$

According to the above assumptions, eq. (3.1) within a control volume V_P may be approximated as

$$\frac{\partial}{\partial t}(\phi_P V_P) + \sum_f \mathbf{S}_f \cdot (\mathbf{U}\phi)_f = \sum_f \mathbf{S}_f \cdot (\Gamma \nabla \phi)_f + S_P V_P \tag{3.9}$$

Here, indices $(\cdot)_P$ and $(\cdot)_f$ denote corresponding variables at control volume and face centroids respectively. The quantities at the face centroids need to be approximated in terms of the unknowns at the control volume centroids.

The convection term may be further developed as

$$\sum_f \mathbf{S}_f \cdot (\mathbf{U}\phi)_f = \sum_f F \phi_f \tag{3.10}$$

where $F = \mathbf{S}_f \cdot \mathbf{U}_f$ is the volume flux through the face. Calculation of the flux F is a subject of the following section. A convection scheme is a procedure of approximating ϕ_f and in the present FVM the approximation is made by (i) central differencing, i.e. distance weighted linear interpolation of the neighboring control volume values, (ii) upwind differencing, i.e. one of the neighboring values is selected based on the value of F at the face, and (iii) blended differencing, i.e. a linear combination of central and upwind differencing where the weights of the combination are either specified in advance or depend on the solution in some predetermined way. Central and upwind differencing have second and first order of accuracy respectively. Central differencing is characterized by dispersive truncation error which manifests itself through spurious oscillations in the solution which cause unboundedness. On the other hand, upwind differencing has a diffusive error and under many circumstances, especially in highly unsteady simulations, the diffusivity of the numerical scheme can have serious adverse effects on the solution. Blended differencing is introduced as an attempt to mitigate unphysical oscillations by introducing just enough numerical diffusivity where needed. The discretization of the convection term is still a subject of intensive development and testing, detailed discussion of which is out of scope of the present work.

The diffusion term may be written as

$$\sum_f \mathbf{S}_f \cdot (\Gamma \nabla \phi)_f = \sum_f \Gamma_f \mathbf{S}_f \cdot (\nabla \phi)_f \tag{3.11}$$

The diffusivity Γ at the face is approximated by linear interpolation of the values at neighboring cell centers. The gradient of ϕ at the face is calculated as a ratio of the difference between the neighboring control volume values of ϕ to the distance between the neighboring control volume centroids. This approximation is second-order accurate for orthogonal meshes (meshes for which the vector between the neighboring control volume centroids is parallel to $\mathbf{S}$). There exist methods to correct for non-orthogonality of the mesh, a discussion of which can be found in Jasak [37].

Source terms are linearized, i.e. their contribution to the rate of change are described as a linear function of the unknown ϕ at cell centers as

$$S_P = S_u + S_p \phi_P \tag{3.12}$$

Time discretization is based on the approximation that ϕ varies linearly with time for a small enough time step. The specific approximation to the temporal derivatives used in the present work are given in the following section.

Boundary conditions may be of Dirichlet or Neumann type, or a combination of the two. Dirichlet boundary conditions specify the value of a dependent variable at the boundary; for the convection term ϕ_f is directly specified and for the diffusion term it is used to calculate $(\nabla\phi)_f$ with the help of the corresponding control volume value. Neumann boundary conditions specify the gradient of the dependent variable at the boundary; for the convection term the gradient is used to linearly extrapolate the control volume value to the boundary and for the diffusion term it is used directly in the approximation. Mixed boundary condition is a per-face combination of the two types of boundary conditions based on a predefined criterion. As opposed to the types of boundary conditions where externally specified parameters are required, periodic boundary conditions signify internal coupling of control volumes at opposite sides of a computational domain and are a question of software implementation.

The highly unsteady multi-scale turbulence fields impose particular requirements on the numerical methods used. As it has been succinctly put by Moin and Mahesh [51]

> The range of scales that need to be accurately represented in a computation is dictated by the physics. The grid determines the scales that are represented, while the accuracy with which these scales are represented is determined by the numerical method.
>
> Along statistically inhomogeneous directions, physical parameters such as channel width, boundary-layer thickness, or mixing layer thickness determine the largest scales. Along homogeneous directions, where periodic boundary conditions are imposed, two-point correlations of the solution are required to decay nearly to zero within half the domain, to ensure proper statistical representation of the large scales.

The methods utilized to solve the fully unsteady three-dimensional LES equations should retain the properties of the continuous differential operators and equations. Particularly, the kinetic energy should be conserved in the inviscid limit. It is known that the standard discretization practices for the convective and temporal terms, as well as the algorithm of pressure-velocity coupling, introduce numerical dissipation which violates the kinetic energy conservation. The levels of numerical dissipation can in some cases overwhelm the effects of the sub-grid scale model in LES. Also, spurious oscillations introduced through the dispersive error of central differencing may be interacting with physical fluctuations of turbulence fields. In general, it is not possible to distinguish the influences of errors from the influences of physics. Therefore a careful choice of approximations needs to be made in order to keep their adverse effects under control.

3.1.1. Discrete filtering in LES

LES in present work assumes implicit filtering by the grid, i.e. fields defined on a given grid are asumed to be filtered fields. The dynamic procedure of determining model coefficients in LES requires fields at two different filtering levels. The test-filtering operation used in present simulations may be described as follows: for a control-volume value of a dependent variable ϕ_P, its filtered value $\bar{\phi}_P$ is given by

$$\bar{\phi}_P = \frac{\sum_f S_f \phi_f}{\sum_f S_f} \tag{3.13}$$

where, for every face of the mesh, ϕ_f is calculated by linear interpolation of the adjacent control-volume values of ϕ.

3.2. Discretization of the Navier-Stokes equations

The Navier-Stokes system is given by eqs. (1.2) and (1.3). In the framework of the eddy-viscosity LES or RANS simulations the Navier-Stokes equations are augmented by an additional viscosity term so the algorithm presented in this section is equally applicable to LES or RANS equation systems. For the more involved turbulence closures such as second-moment RANS models or differential sub-grid stress models in the LES framework a practice is devised which combines the implicit and explicit eddy-viscosity diffusive terms with explicit model contributions to achieve acceptable robustness of the simulation algorithm. The algorithm implemented in the present method is segregated, meaning that the equations are solved sequentially, treating the inter-variable coupling and non-linearity explicitly. The segregated approach poses a particular challenge in determining the pressure as the evolution equation for the pressure is not available. This issue is addressed by the so-called pressure-velocity coupling algorithms, which are iterative procedures where an equation for the pressure is derived to produce the pressure field which ensures divergencelesness of the velocity. The PISO (pressure-implicit with splitting of operators) algorithm of Issa [36] is used in the present LES. The time derivative in the momentum equation is discretized using the three-time-step backward differencing as

$$\frac{\partial U_i}{\partial t} \approx \frac{\frac{3}{2}U_i^n - 2U_i^o + \frac{1}{2}U_i^{oo}}{\Delta t} \tag{3.14}$$

The convective term is discretized in its rotation form, see eq. (1.7), and is treated explicitly. The rotation form is selected on the basis of precursor simulations. The specific simulation of calm fluid which is perturbed only at the boundary by velocities which are on average close to zero has proved to be a challenge for the conventional discretization schemes which have been developed and tested for convection dominated flows. By the choice of the convection discretization, statistically diffusive character of the physics is reflected in the discretization. The vorticity in the rotating form of the convective term is discretized by calculating the Hodge dual of the skew-symmetric part of the velocity gradient (see [48]). The diffusive term is treated implicitly whereby the effective kinematic viscosity (the sum of molecular and turbulent viscosities) is linearly interpolated on the cell faces and the face gradient is calculated according to eq. (3.11). The contribution of the turbulent stress tensor proportional to the transposed-gradient part of the rate of strain is treated explicitly.

3.2.1. The equations for momentum and pressure

The semi-discretized form of the momentum equation can be formally written as

$$a_P^{\mathbf{U}}\mathbf{U}_P = \mathbf{H}(\mathbf{U}) - \nabla p \tag{3.15}$$

where ∇p is at this stage not discretized and

$$\mathbf{H}(\mathbf{U}) = -\sum_N a_N^{\mathbf{U}}\mathbf{U}_N + b_P^{\mathbf{U}} \tag{3.16}$$

The discretized continuity equation reads

$$\sum_f \mathbf{S}\cdot\mathbf{U}_f = \sum_f F = 0 \tag{3.17}$$

Taking divergence of eq. (3.15), and taking into account that (somewhat imprecisely) $\nabla \cdot \mathbf{U}_P = 0$ the following equation for pressure is derived

$$\nabla\cdot\left(\left[a_P^{\mathbf{U}}\right]^{-1}\nabla p\right) = \nabla\cdot\left(\left[a_P^{\mathbf{U}}\right]^{-1}\mathbf{H}\left(\mathbf{U}\right)\right) \tag{3.18}$$

From eq. (3.15) the face flux F may now be expressed as

$$F = \mathbf{S}\cdot\mathbf{U}_f = \mathbf{S}\cdot\left[\left(\frac{\mathbf{H}\left(\mathbf{U}\right)}{a_P^{\mathbf{U}}}\right)_f - \left(\frac{1}{a_P^{\mathbf{U}}}\right)_f (\nabla p)_f\right] \tag{3.19}$$

In matrix notation, the momentum equation without the contribution of the pressure gradient reads (see eq. (3.4))

$$\left(\left[a_P^{\mathbf{U}}\right]_{int} + \left[a_P^{\mathbf{U}}\right]_{bou} + \left[a_N^{\mathbf{U}}\right]\right)[\mathbf{U}_P] = \left[b_P^{\mathbf{U}}\right]_{int} + \left[b_P^{\mathbf{U}}\right]_{bou} \tag{3.20}$$

The pressure Poisson equation, eq. (3.18), has a diffusion coefficient equal to the diagonal coefficient in the momentum matrix. In general, the internal contribution to the diagonal coefficient is a scalar, i.e. equal for all three components of velocity, while the contribution from the boundary conditions is different component-wise. In order to surmount this inconsistency (and enhance diagonal dominance of the pressure matrix) the pressure diffusivity coefficient is calculated as

$$\left[a_P^{\mathbf{U}}\right]_{int} + \left\langle\left[a_P^{\mathbf{U}}\right]_{bou}\right\rangle_{cmpts} \tag{3.21}$$

where the angled brackets denote an arithmetic average over component contributions. The $\mathbf{H}\left(\mathbf{U}\right)$ operator now reads

$$\mathbf{H}\left(\mathbf{U}\right) = \left(\left[a_N^{\mathbf{U}}\right] - \left[a_P^{\mathbf{U}}\right]_{bou} + \left\langle\left[a_P^{\mathbf{U}}\right]_{bou}\right\rangle_{cmpts}\right)[\mathbf{U}_P] + \left[b_P^{\mathbf{U}}\right]_{int} + \left[b_P^{\mathbf{U}}\right]_{bou} \tag{3.22}$$

The discretized pressure Poisson equation, eq. (3.18), may be formally stated in matrix form as

$$\left(\left[a_P^p\right] + \left[a_N^p\right]\right)[p_P] = \left[b_P^p\right] \tag{3.23}$$

From the discretization of the Laplacian, c.f. eq. (3.11), it may be shown that the second term in the flux-update expression may be rewritten as [38][2]

$$F = \mathbf{S} \cdot \mathbf{U}_f = \mathbf{S} \cdot \left(\frac{\mathbf{H}(\mathbf{U})}{a_P^{\mathbf{U}}} \right)_f - a_N^p (p_N - p_P) \tag{3.24}$$

3.2.2. The PISO algorithm

The PISO (pressure-implicit with splitting of operators) algorithm proceeds as follows[3]

1. The implicit momentum equation is assembled and solved. This step is known as *momentum predictor*. A new value of the velocity field is obtained using the currently known pressure field.
2. The operator $\mathbf{H}(\mathbf{U})$ is assembled as outlined above.
3. The face flux field of momentum corresponding to the non-pressure contributions is calculated by linearly interpolating $\mathbf{H}(\mathbf{U})$ to mesh faces. Additionally a correction term is introduced here, the exact form of which depends on the specific temporal discretization scheme used. Regardless of the specific time discretization scheme, a source term is introduced into the $\mathbf{H}(\mathbf{U})$ which is proportional to the value of cell-centered velocity at old time(s). When this term is used in the pressure equation, it features as a source term proportional to the divergence of velocity at old time(s). The pressure equation, eq. (3.18), is, however, a statement of balance between face fluxes and face-centered pressure gradients,[4] and therefore the divergencelessness of the cell-centered velocities is not strictly assured. In order to remove the inconsistency, the divergence of cell-centered velocities at old times is replaced with the corresponding divergence of the face flux.
4. The pressure equation, eq. (3.18), is solved. This step is known as the *pressure solution*.
5. The conservative face flux is calculated using the new pressure solution according to eq. (3.24). The velocity field is corrected using the new pressure gradient.

Steps 2. to 5. are repeated for a specified number of times to achieve acceptable convergence of the pressure equation – here 2 repetitions have been selected in accordance with the recommendations available in literature.

[2] This is an expression for internal faces. On zero-gradient pressure boundaries there is no contribution to the boundary faces from the second term. On fixed-value pressure boundaries, the contribution is $a_P^p p_P$ for cell P adjacent of the corresponding boundary face.

[3] The algorithm outlined here is a variation on the PISO algorithm available in OpenFOAM; here, the available corrections pertaining to mitigating adverse effects of mesh non-orthogonality on the overall accuracy of the algorithm are discarded as these are of no significance for the present equispaced box-type meshes, the convection term in the momentum equation is discretized explicitly as stated above and the velocity correction step is performed using the conservative face flux field instead of the pressure gradient.

[4] The pressure gradient adjusts itself to the non-pressure fluxes in order to form zero-divergence conservative face flux.

4. Results and discussion

This chapter presents the results of LES of turbulent diffusion. The numerical setup and boundary conditions are described in the first section. In the next section, a summary is presented of the accompanying DNS and experimental results, as relevant for the present work. Following this general introduction, separate sections are devoted to presenting the simulations of HIT, free turbulent diffusion, confined turbulent diffusion, rotating homogeneous turbulence and turbulent diffusion in the rotating frame.

4.1. Computational setup

The symmetry analysis of the shear-free turbulent diffusion case has been carried out under several constraints. The major constraint imposed in the analytical study is consideration of the two-point correlation equations without viscosity. This formally implies $\mathrm{Re} \to \infty$. Practically, this constraint amounts to a sufficiently high Reynolds number whereby the separation of the largest and smallest relevant scales is large enough for the dynamics of the largest scales to be treated independently of viscosity. Second, the mean flow or mean rate of strain should not be present in turbulent diffusion fields. The description of the simulation settings that follows is given in the light of these constraints.

The computational domain is shown in fig. 4.1. In the x and z directions periodic boundary conditions are imposed leaving y as the only direction of statistical inhomogeneity. At the planes perpendicular to y Dirichlet boundary conditions are imposed on velocity. The planar velocity fields are generated in simulations of HIT by sampling velocities at a plane at every time step of the run. This configuration is chosen because of the following advantages

(i) the net mass-flow rate for the two forcing boundaries is zero, as the same velocity fields are used at opposing boundaries at every time step,

(ii) the use of two statistically equal halves of the computational domain doubles the number of sampling points per time step, i.e. as the simulations are statistically unsteady the averaging is performed over two homogeneous directions taking into account the statistical symmetry of the computational domain,

(iii) the velocity fields (and therefore the kinetic energy fields) at the boundaries are statistically steady as required by the analytical analysis, and

(iv) the fields reflect true turbulence dynamics faithfully, i.e. the fields are obtained from the solution of the LES equations and thereby contain all relevant spatio-temporal correlations of realistic large-scale turbulence.

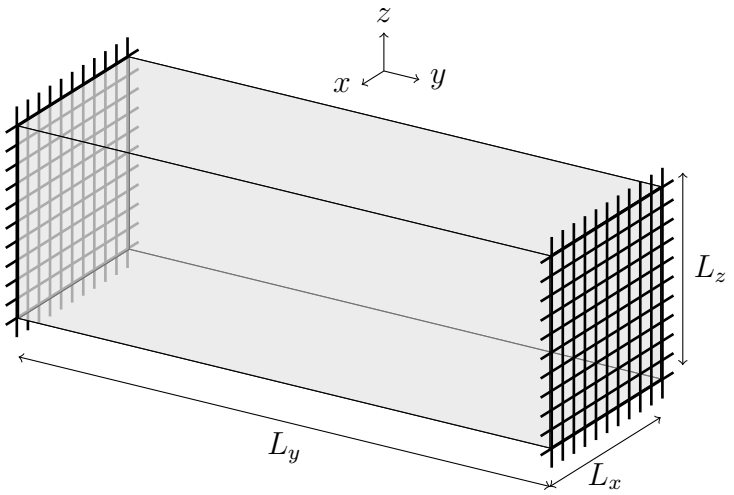

Figure 4.1.: Sketch of the computational domain, perturbations are applied at two opposing boundaries using planes sampled from HIT simulations

The most important disadvantage of the setup is the possibility of a mutual influence between the two turbulent diffusion fields created at the boundaries. The extent to which the interaction of the fields influences the statistical quantities of interest has been estimated by performing simulations at an increased size of the computational domain in the y direction.

4.2. Non-dimensionalized momentum equation and geometry

The present work is a part of a research project which has been motivated by the results of Oberlack and Guenther [56]. The project is concieved as an attempt to generate experimental and numerical turbulent fields which conform to the scaling laws derived analytically. In the experiments, turbulence is generated by a planar grid of spacing M oscillating perpendicularly to its plane at a frequency f and amplitude $S/2$ in a tank of volume $L_x \times L_y \times L_z$ (see [42]). In the DNS calculations, the source of energy is a forcing function characterized by a sinusoidal dependence of its y-component on the x and z directions with the wavelength M, a sinusoidal dependence of the same component on time with frequency f and amplitude $S/2$ and a random part in all three directions (see [40]). Similarly it may be considered that, in the present case, the integral length scale of HIT L is a spatial scale of forcing turbulence and integral time scale T is temporal scale of the forcing turbulence. In order to point out relevant parameters for qualitative comparisons of the LES results with experiments and DNS the momentum equation is analyzed with respect to these parameters. The momentum equation with the forcing term and the Coriolis term reads

$$\frac{\partial \mathbf{U}}{\partial t} + \mathbf{U} \cdot \nabla \mathbf{U} = -\nabla P + \nu \nabla^2 \mathbf{U} + \mathbf{f} + 2\boldsymbol{\Omega} \times \mathbf{U} \tag{4.1}$$

where $\boldsymbol{\Omega}$ is the rotation vector. It may be assumed that the force $\mathbf{f}$ imposes a length scale l_f and time scale l_f. The rationale for such an assumption lies in the fact that the experimental forcing is characterized by the a length-scale S and a time-scale $1/f$ and that an increase in any of the two parameters, S or f, yields a stronger forcing and therefore

larger Reynolds number. Along the same line of reasoning, for HIT the Reynolds number is directly proportional to L and inversely to T. The non-dimensionalized momentum equation with respect to these scales reads

$$\frac{\partial \mathbf{U}^*}{\partial t^*} + \mathbf{U}^* \cdot \nabla \mathbf{U}^* = -\nabla P^* + \frac{1}{\mathrm{Re}} \nabla^2 \mathbf{U}^* + \mathbf{f}^* + \frac{1}{\mathrm{Ro}} \frac{\mathbf{\Omega}}{\Omega} \times \mathbf{U}^* \tag{4.2}$$

where $\Omega = |\mathbf{\Omega}|$, the forcing $\mathbf{f}^*$ may be assumed to be a function of $\mathbf{x}^*$ and t^* and the following holds

$$\begin{gathered} \mathbf{x} = \frac{\mathbf{x}}{l_f},\ t^* = \frac{t}{t_f},\ \mathbf{U}^* = \frac{\mathbf{U} t_f}{l_f},\ P^* = \frac{P t_f^2}{l_f^2} \\ \mathrm{Re} = \frac{l_f^2}{t_f \nu},\ \mathrm{Ro} = \frac{1}{2\Omega t_f} \end{gathered} \tag{4.3}$$

Therefore to fully specify the non-dimensional equation Re and Ro need to be prescribed along with any non-dimensional parameters which describe the forcing acceleration in the non-dimensional space and time. Furthermore, to fully characterize the system at hand the non-dimensional geometry needs to be given as $L_x^* \times L_y^* \times L_z^*$.

In the case $\mathrm{Ro} \to \infty$ (the non-rotating case) the forcing directly produces motions of length-scale l_f and velocity-scale l_f/t_f. This statement may be said to fully apply to the experimental and DNS setup as distinct scales of motion are specified by the choice of the mesh spacing M, the stroke S and the frequency f. In the experimental case the wakes of the grid bars interact as they propagate away from the grid to form HIT to a good approximation. Similarly, the random component of the forcing in DNS acts to enhance the natural instabilities and the highly regular velocity field produced in the vicinity of the forcing breaks down to HIT as the distance from the forcing region increases. Therefore, in the both cases multi-scale motion arises as a spontaneous breakdown of regularity due to instabilities and imposed perturbations. The integral length and time scales of these, now fully turbulent, motions are roughly proportional to the forcing parameters and therefore the Reynolds number. Contrary to the above two cases, in the present LES the boundary perturbation is essentially multi-scaled conforming to genuine turbulence dynamics. In order to create a simulation which fully complies with the companion experiments one would need a full representation of the oscillating grid motion. The requirements of such a simulation exceed the available resources by orders of magnitude (see [43]). As trial simulations have shown, a typical eddy-viscosity LES model applied to a flow in which the source of motions is a forcing as used in the companion DNS, creates dubious values of sub-grid scale viscosity in the regions where the velocity field is highly regular. Essentially, the regular geometric structure of the DNS forcing renders eddy-viscosity LES models inapplicable. Furthermore, the force is an explicit source in the FVM and is therefore proportional to the volume of the cell it acts in. This renders grid refinement in the present case a non-trivial exercise as the forcing region is grid-size dependent. For the reasons stated, an attempt has been made to match the experiments and DNS only approximately, i.e. only to the extent that the Taylor microscale Reynolds numbers reported in the experiments and DNS fall within the range of the Reynolds numbers considered in the present study.

For the rotating case only the experimental data are available. The measurements indicate strong suppression of turbulence propagation due to rotation, and that the suppression increases with the rotation rate. The experiments are performed by suddenly starting the

oscillations of the grid after the water in the tank has been brought to a state of solid-body rotation. The measurements of the TNTI position indicate a significant discrepancy with the theoretical results of Oberlack and Guenther [56]. Similar to the arguments in the preceeding paragraph, an attempt is made here to look at the changes rotation makes to the propagation of turbulence which has been initially at the Taylor microscale Reynolds number and the Rossby number close to values reported in the experiments. Additionally, the inverse cascade of energy takes place in the rotating homogeneous turbulence and the energy dissipation is suppressed; hence, the same forcing parameters used to keep the non-rotating HIT in a statistically steady state lead to increased values in the Reynolds number in the rotating case.

In summary, the non-dimensional momentum equation indicates that the system under consideration is uniquely specified by prescribing the Reynolds and Rossby numbers, which in turn, by the construction of the system, are determined by the forcing parameters. Additional independent quantities are non-dimensional domain sides, the value of which is proportional to the forcing parameters as well. The forcing directly influences the large-scale motions which, due to the intrinstic instabilities and perturbations, develop a turbulent multiscale motion, or the source of motion is itself multiscale turbulence. In turn, the spatio-temporal development of these motions is influenced by geometry and rotation effects. The large-scale parameters govern the transport of momentum by turbulence and therefore the rate of spreading of turbulence. The mechanism by which non-turbulent fluid gains vorticity and turns turbulent is a small scale process of diffusion of vorticity.

4.3. LES of HIT

This section presents characteristics of HIT fields used subsequently as a source of turbulence in the simulations of turbulent diffusion. A detailed description of the algorithm is given in appendix B. Additionally, further information on the LES of HIT may be found in a comprehensive study by Fureby et al. [18].

Simulations at three different Reynolds numbers have been performed, at two different grids, i.e. $N = 64$ and $N = 96$, which amounts to 200k and 900k cells respectively. It is worth noting that the simulations have been started from DNS runs of HIT, i.e. initial velocities are fully developed turbulent fields. A dynamic sub-grid scale model with full spatial averaging of the model coefficients has been used (see section 2.2). Turbulent statistics of interest have been averaged over the whole volume. Table 4.1 contains a brief summary of parameters of the present LES of HIT.

Case	α_f	σ_f	N	Re_λ	$\epsilon_{\mathrm{mod}}/\epsilon$	k_{mod}/k	ν_t/ν
lesHit1	40.0	0.583	64	40.60	0.0193	0.00565	0.0436
lesHit2	30.0	0.883	64	59.10	0.0389	0.00755	0.0815
lesHit3	10.0	0.983	64	130.72	0.146	0.0122	0.282
lesHit4	10.0	0.983	96	105.94	0.0578	0.00603	0.111

Table 4.1.: Summary of relevant parameters of LES of HIT. The values are temporally averaged over a statistically steady period of the simulation. Forcing was applied up to $\kappa_f = 2\sqrt{2}\kappa_{\mathrm{max}}$; this corresponds to 92 forced Fourier modes. For an explanation of the meaning of particular parameters c.f. appendix B.

In order to gain insight into the structure of the obtained solutions, fig. 4.2 shows the isocontour of enstrophy colored by the velocity magnitude in a fully developed LES field calculated for the lesHit4.

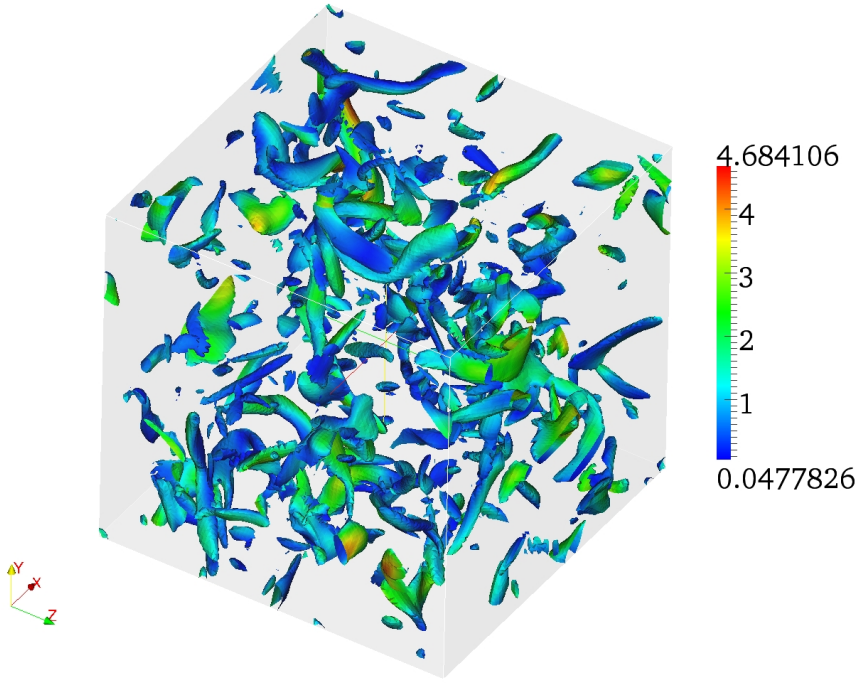

Figure 4.2.: Iso-contour of enstrophy colored by $U^2/\langle U^2\rangle$ calculated from the resolved velocity from lesHit4; figure shows the isocontour at $\langle\omega^2\rangle+2\sigma_{\omega^2}$, where σ_{ω^2} is the standard deviation of enstrophy [35].

Development of the Taylor microscale Reynolds number, Re_λ, is shown in fig. 4.3. This range of Re_λ has been chosen to cover a range of values reported in [28, 29, 42]. The last two runs listed in table 4.1 have been performed with the same forcing parameters, only at different resolution. The estimated Reynolds number changes substantially due to slight under-resolution of the case with $N = 64$ and presumably due to the deficiencies of the approximation formula for the total dissipation rate from LES. Nevertheless, it may be argued, based on the resolution test and the DNS runs presented in appendix B, that the Reynolds numbers are within the intended range.

Similar to the cases treated in the appendix B, turbulent time scales, calculated from the total values of the turbulent kinetic energy and its rate of dissipation, exhibit stable values after initial transients. Stable values develop after less than one eddy turn-over time, and the simulations last about 8-20 eddy turn-over times for different runs. The integral length scales show the same behavior. It is interesting to note that the sensitivity to the change in resolution for the simulation at the largest Reynolds number is clearly more apparent when the length scales are concerned. This may be explained by noting that the forcing scheme, depending on the parameter σ and the value of the time step, governs the correlation time of the forcing and therefore the time scale of the flow.

Figure 4.5 shows the evolution of the length and time scales of the resolved velocity field in the LES of HIT. It may be argued that these are the appropriate characteristic scales

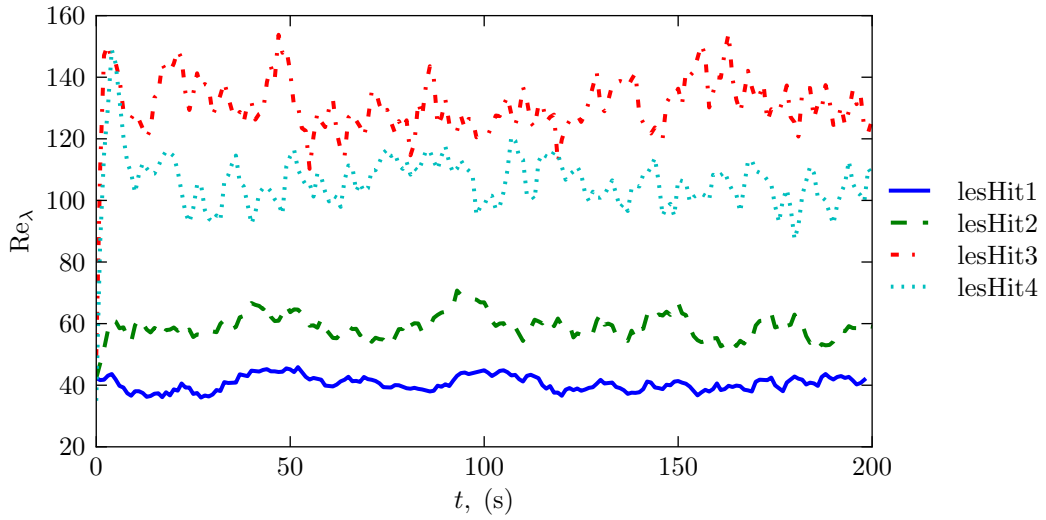

Figure 4.3.: Taylor microscale Reynolds number calculated in LES of HIT

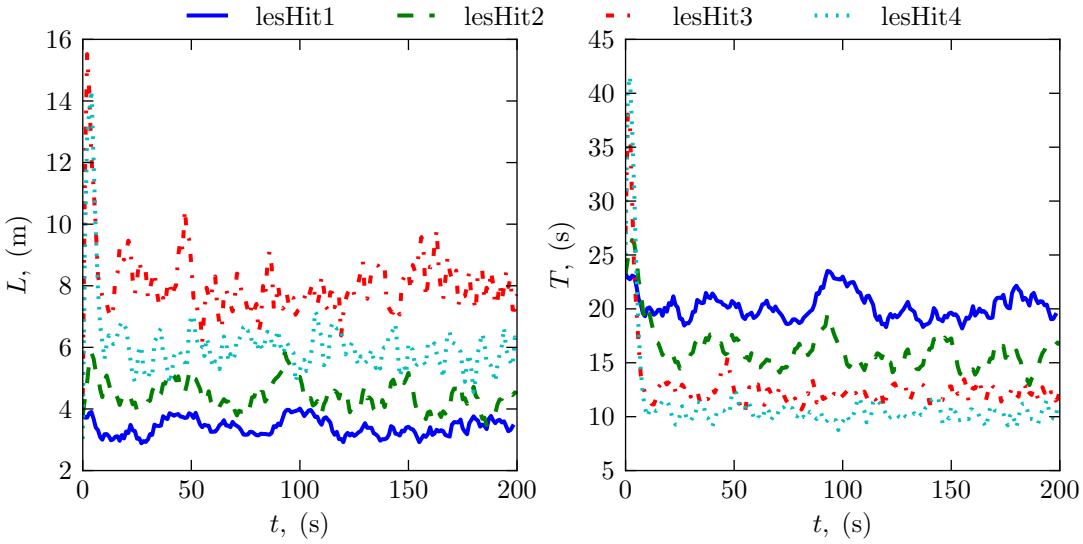

Figure 4.4.: The integral length and time scales as calculated from the total turbulent kinetic energy and rate of dissipation.

to consider, as the modeling contributions, quantified e.g. by presence of sub-grid scale viscosity, is only significant in the vicinity of the forcing boundaries and the propagation proceeds by the resolved scales only.

Figure 4.6 displays the development of some significant LES indicators. Modeled parts of the turbulent kinetic energy and its dissipation rate increase with the Reynolds number for constant resolutions, and for all the runs are statistically stable. With increasing resolution, the algorithm behaves in a predictable manner, as seen for the last two runs. The present LES, judged by the DNS runs in appendix B, i.e. the modeled quantities are comparatively small (see [58]).

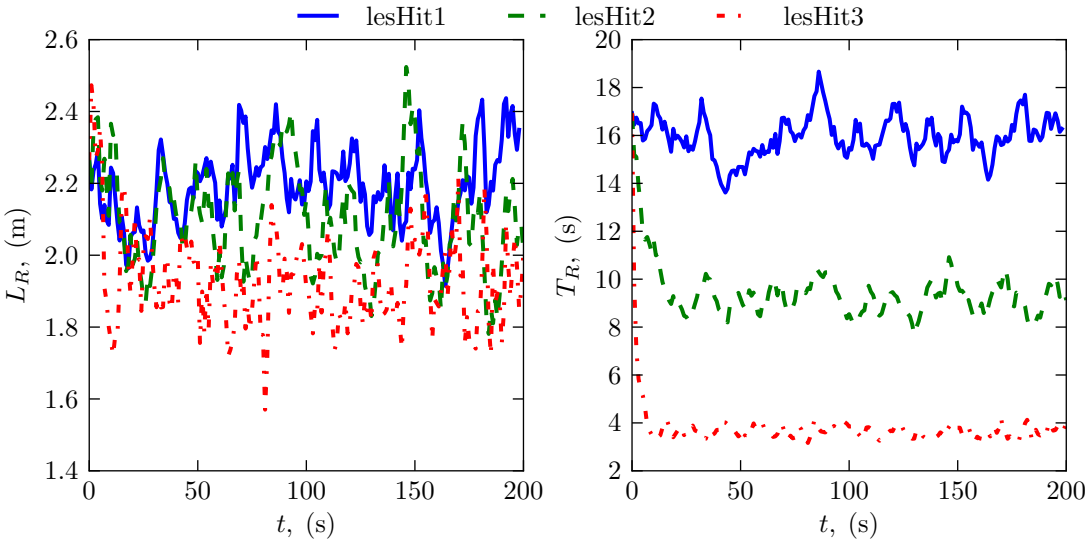

Figure 4.5.: Evolution of the length and time scales of the resolved velocity field of LES of HIT.

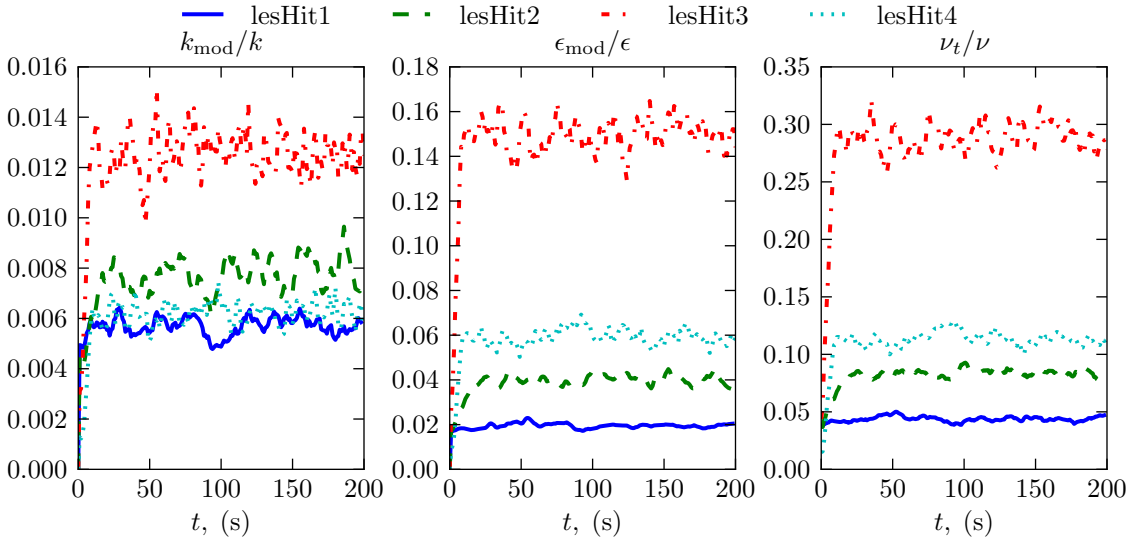

Figure 4.6.: Some parameters for the LES of HIT.

The one-dimensional normalized energy spectra are shown in fig. 4.7. Consistent with the evolution of the integral length scales, the relative increase in the largest scales with the Reynolds number is apparent. Additionally, the resolution test for $\mathrm{Re}_\lambda = 100$ is reflected in the energy spectra by decreased energy content of the largest scales, while the smallest scales, i.e. the estimated Kolmogorov scale, remain in good agreement.

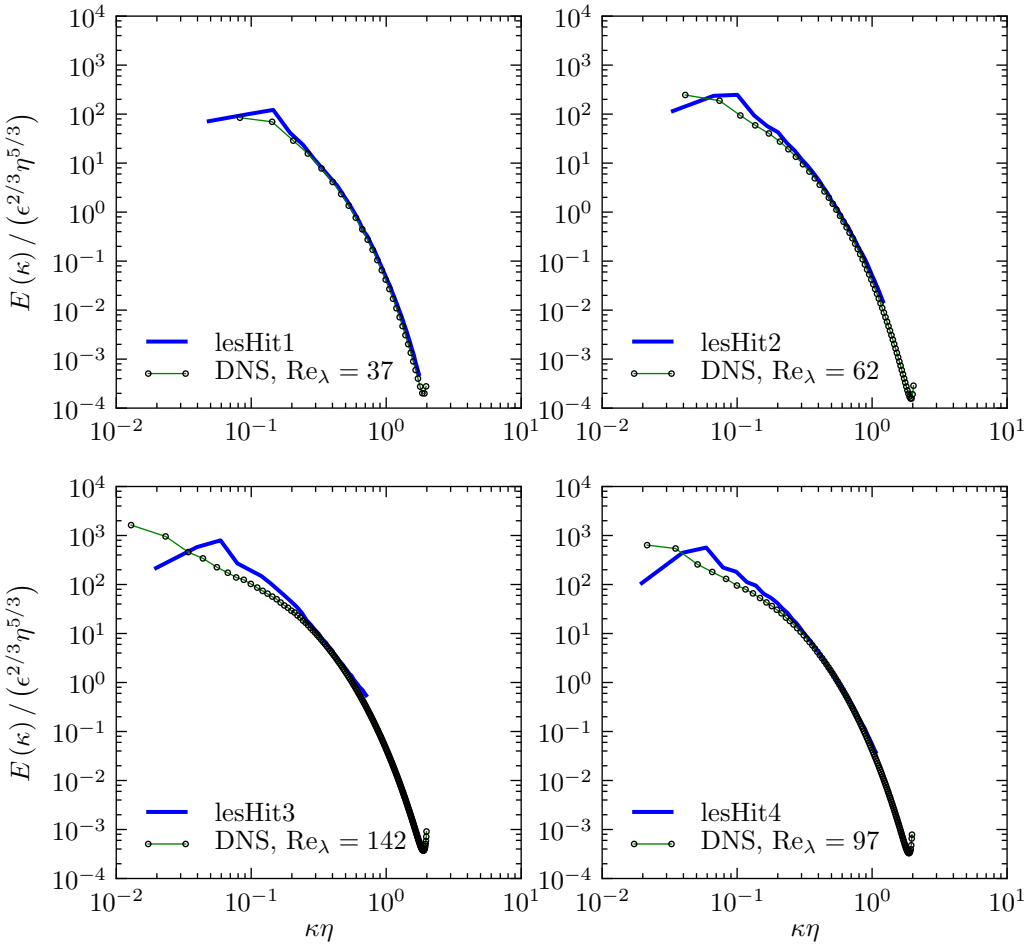

Figure 4.7.: Non-dimensional energy spectrum function of resolved velocity for the simulations summarized in table 4.1 compared to DNS of Jiménez et al. [39]. DNS data are available under http://torroja.dmt.upm.es/ftp/AGARD/, last accessed on February, 2011.

4.4. Detection of TNTI

A summary [33] of contemporary advances and future directions in research on interfaces and inhomogeneous turbulence classifies TNTI in the present context as a boundary interface not affected by mean shear (as opposed to boundary interfaces affected by mean shear, internal interfaces with or without mean shear, or interfaces associated with density or density gradient discontinuities in flows where body forces play significant role). TNTI is a concept which implies that there exist a surface, or, more precisely, a thin layer where flow quantities, when conditionally averaged, exhibit a jump. In a recent study on the thickness of the TNTI, Da Silva and Taveira [10] have shown that the thickness of the TNTI is proportional to the radius of the large-scale vorticity structures in the vicinity of

the TNTI, and that in turn the size of the structures is dependent on the mean shear in the region of TNTI. They have analyzed DNS data for a planar jet and shearless turbulent diffusion, and concluded that the thickness in the case of the planar jet scales with the Taylor microscale, λ, and, in the case of shearless turbulent diffusion, the thickness is proportional to the Kolmogorov scale of turbulence η.

Detection of TNTI has been a subject of interest in several settings [59]. In early experimental studies of partially turbulent flows (e.g. turbulent boundary layers) the subject of interest had been to quantify the external intermittency (a property of regions within a flow with randomly changing turbulent and non-turbulent state). This problem was addressed mainly by introducing temperature as a passive scalar into the turbulence-generating core of the flow and using point temperature sensors to distinguish between the turbulent and non-turbulent instances. This method requires introduction of arbitrary parameters, and, in general, does not yield sharp interface positions. In their paper, Prasad and Sreenivasan [59], recognised the problem and suggested a generalized procedure of determining the interface position using laser-induced fluorescence (LIF) imaging techniques for visualizing turbulent flows. LIF allows visualization of the concentration of fluorescent dye which is introduced as a passive scalar in the generating core of turbulence and is advected by the flow.[1] In this study, Prasad and Sreenivasan suggest using the histogram of the dye concentration, which in general should be bimodal, i.e. should feature two peaks, one which corresponds to the dye containing region and another one at zero which corresponds to the non-turbulent region. A local minimum may be found between the two peaks and is used as a threshold for the detection of TNTI. In cases where the second peak is not easily obtainable, they proposed a more involved method of calculating the so called threshold averaging concentration, which is a monotonically increasing function of threshold value with two distinct slopes. Threshold averaging concentration is the mean value of concentration of all the points at which concentration is larger than a given value. For larger values of threshold, the threshold averaging concentration increases significantly slower than the corresponding averages for small values of threshold. The intersection value of the two slopes is then used as a threshold suitable for TNTI. They have confirmed the plausability of this hypothesis on the study of the self-preserving turbulent round jet. Holzner et al. [30] in their two-dimensional PIV study of the oscillating-grid turbulence have compared the concentration method to the method of setting the threshold criterion based on the amplitude of noise in the measurement of the out-of-plane vorticity. They have shown that the two criteria yield similar results. Further analysis of threshold criteria for detection of TNTI have been documented in the case of the self-preserving round jet by Anand et al. [1]. In the accompanying experiments, see [41], the criterion of Holzner et al. [30] has been used for TNTI detection.

Straightforward application of the 'small-vorticity' criterion to LES data is not reliable. Large-scale vorticity in LES, as calculated from the resolved velocity field, is strongly dependent on the chosen filter width. In this work a hybrid criterion is chosen. Instead of the passive scalar concentration field, the normalized resolved vorticity is used in the algorithm of Prasad and Sreenivasan [59] as a turbulence discriminator. The resolved vorticity field in LES is normalized by the maximal value of vorticity present in the domain. This value usually occurs on the forcing boundaries. The *threshold-averaged vorticity* (TAV) is

[1] Fluorescent dyes have a high Schmidt number, meaning that their molecular diffusion is negligible and is not going to blur the interfaces.

calculated as

$$\mathrm{TAV}\,(\theta) = \left\langle \frac{\omega}{\omega_{\max}} \right\rangle \Bigg|_{\frac{\omega}{\omega_{\max}} > \theta} \tag{4.4}$$

i.e., for a threshold value θ an average is calculated of all normalized resolved vorticity magnitudes at cell centers which are greater than the chosen threshold.

Figure 4.8 shows the threshold-averaged vorticity for the cases hitDiff1 and hitDiff5 from table 4.2 for 1000 equally distributed values of θ between the largest and smallest normalized vorticity magnitude. It may be seen that $TAV\,(\theta)$ is to a good approximation independent of time or grid size for a single case, i.e. independent of the different vorticity levels at different filter widths. The change of slope occurs in the range $\theta \in \left[10^{-2}, 10^{-1}\right]$.

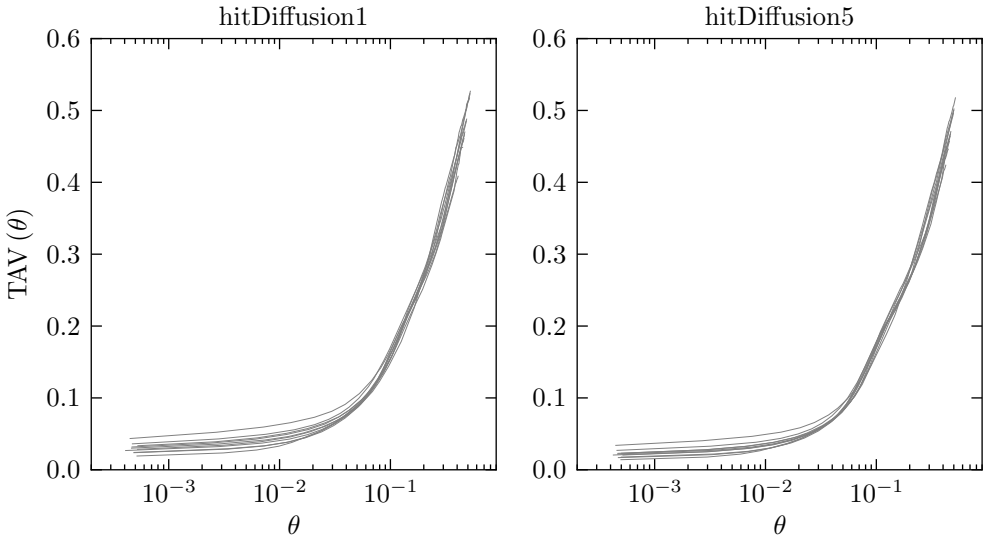

Figure 4.8.: Threshold averaged resolved normalized vorticity for cases hitDiff1 and hitDiff5 (see table 4.2) at several times.

Discussion of the front position dependence on the chosen value of the threshold is now given for the three cases of turbulent diffusion in the following sections.

The second aspect of turbulent front position detection is the means to obtain actual interface positions once the criterion has been established. In the present work two approaches have been tested. The first approach is to use averaged (over homogeneous layers of cells, and using statistical symmetry of the computational domain) normalized vorticity profile, and calculate positions where averaged profiles take the value prescribed by the criterion. The second possible approach is to extract triangularized isosurfaces of normalized vorticity magnitude according to the prescribed value (the isosurfaces are three-dimensional analogues of the lines of constant normalized vorticity in fig. 4.9), and calculate average distance of the isosurface from the boundary (forcing) plane. Both of the approaches for calculation of the TNTI position have been analyzed. They yield different but very comparable values for the front position. Turbulent front positions presented in the subsequent sections are obtained from profiles of the averaged normalized vorticity magnitude.

4.5. LES of turbulent diffusion

Table 4.2 shows a summary of the performed simulations. Simulations have been started from zero initial values of velocity and pressure. The Smagorinsky and the dynamic Smagorinsky model without spatial averaging and with clipping of the negative values of turbulent viscosity have been used as indicated in the table 4.2. Simulations have been performed for four to eight eddy turn-over times. Most of this time interval corresponds to the initial stage of turbulent diffusion, as discussed in section 2.1. On 96^2 cross-section grids, where the available velocity perturbation data have been calculated for a 64^2 grid, velocities have been linearly interpolated.

No.	Case	N	N_{boxes}	lesHit	Re_λ	Model
1	hitDiff1	64	4	lesHit1	40.60	locDynSmagorinsky
2	hitDiff2	64	4	lesHit2	59.10	locDynSmagorinsky
3	hitDiff3	64	4	lesHit3	130.72	Smagorinsky
4	hitDiff4	64	6	lesHit3	130.72	Smagorinsky
5	hitDiff5	96	4	lesHit1	40.60	locDynSmagorinsky
6	hitDiff6	96	4	lesHit2	59.10	locDynSmagorinsky
7	hitDiff7	96	4	lesHit3	130.72	locDynSmagorinsky

Table 4.2.: Summary of relevant parameters of LES of turbulent diffusion. The grid for the simulations of turbulent diffusion is represented here as a superposition in y-direction of N_{boxes} of cubes of N^3 cells, with cube side length $L = 2\pi$, (m).

In order to investigate the influence of the total extent of the computational domain in the direction of turbulence propagation, the case at the largest source Reynolds number has been simulated for two different lengths of the domain (entries 3 and 4 in table 4.2, results are not shown here). The length of the domain does not have any significant influence on the propagation of turbulence as evidenced by the instantaneous fields or development of profiles of averaged vorticity or turbulent kinetic energy.

Contours of the resolved vorticity magnitude in the mid-plane of the computational domain are shown in fig. 4.9 for the two different resolutions and at several time instants. Superimposed are contour lines of the normalized vorticity magnitude at the values 0.001 and 0.1. Qualitative features of the turbulence propagation are shown to be well repeated at the refined spacing. This suggests that the linear interpolation at the boundaries for the refined grid boundary perturbation does not have a qualitative impact on the solutions.

The differences at the two resolutions are twofold. Firstly, one can see that grid refinement brings much richer contortion of the TNTI, or conversely, that the low-resolution merely coarsens the undulations of the interface without significantly affecting the overall propagation. This might suggest that nibbling, identified as the predominant mechanism of the turbulent entrainment process, is well reproduced numerically regardless of the absolute sizes of the smallest scales present in the fields. However, this point should be investigated with respect to some resolution measure of the original HIT fields (e.g. ratio of the modeled to resolved energy, etc.), i.e. this conclusion might be valid only as long as a significant portion of the small scales is resolved. This is perhaps an artifact of this particular configuration, as the contribution to the overall dynamics of LES modeling is virtually irrelevant at

the locations of the TNTI. Second, apparent is the increased departure between the two different levels of the normalized vorticity magnitude with increased resolution. Even though the threshold averaging curves are to a good approximation invariant to the grid resolution, this is not necessarily reflected in the actual fields from which they are produced.

The turbulent diffusion case is characterized by the lack of mean velocity and mean rate of strain. This property has been verified in the simulations in the sense that the energy of the averaged velocity lies under 1% of the fluctuating energy. This small contribution is pronounced at the forcing boundaries and decays rapidly to zero with the distance from the forcing.

In fig. 4.10 the development of the normalized vorticity profiles is shown for three different cases at resolution $4 \times N^3 = 4 \times 64^3$ as listed in table 4.2. Consistent with the total duration of simulations and the values of the time scales of the resolved velocity field of corresponding HIT forcing, TNTI propagation is simulated from 6 to 10 large eddy turnover times at the smallest and largest Reynolds number respectively. It is evident from fig. 4.10 that convergence of the statistics as obtained by averaging over statistically identical homogeneous layers of cells deteriorates with increasing Reynolds number.

Figure 4.11 shows the profiles of the normalized vorticity magnitude along the inhomogeneous direction for the three cases with refined grid, $4 \times N^3 = 4 \times 96^3$, where the velocity perturbation at the boundary has been interpolated from the coarser HIT simulations. Comparing fig. 4.11 to fig. 4.10, one can see that the overall values of the normalized vorticity magnitude remain approximately unchanged with grid refinement. This indicates that, at least in the present case, this variable may be appropriate for detection of TNTI in LES, keeping in mind that, all other paremeters being equal, levels of resolved vorticity in LES increase with grid refinement.

Figure 4.12 and fig. 4.13 display a calculation of the front-position curve for threshold values of 0.001 and 0.01. The front position is calculated for every time step by interpolating the threshold value to the profile line, i.e. the front position must not lay on grid points. The lower value of the threshold normalized vorticity yields similar results on TNTI propagation at the Reynolds numbers and grid resolution considered. The larger threshold value on the other hand falls in the region of highly variable normalized vorticity as can be seen from figs. 4.10 and 4.11 and the detected front positions are correspondingly volatile, which is also related to the convergence of the statistical averages used in the front position calculations. This shows that the presently employed TAV criterion (see fig. 4.8) for determination of the threshold value slightly overestimates the real threshold value, but is nevertheless a good indicator of the coarse interval in which this value should reside. Further research is needed in order to make a definitive statement on the performance of the overall TNTI detection procedure.

Figures 4.14 and 4.15 show averaged profiles of turbulent kinetic energy along the inhomogeneous direction of turbulence propagation. Some unboundedness of the velocity field caused by the loss of the order of accuracy of the pressure-velocity coupling algorithm at the boundary is evident in the profiles of turbulent kinetic energy. This issue has been addressed in references [10, 57] (where simulations with instantly imposed significantly different values of velocity are performed) by drastically reducing the time step. However, this method did not improve the present calculations. Another approach is to improve the accuracy of the pressure-velocity coupling algorithm at the boundary, as seen in e.g. [63]

and references therein. Implementation of the ideas presented in the above references is a non-trivial effort, and is left for future work.

Further evidence of the appropriateness of the present algorithm, inspite of the mentioned errors at the forcing boundaries, comes from the investigation of conditionally averaged quantities with respect to TNTI. Figure 4.16 shows conditionally averaged profiles of enstrophy and kinetic energy obtained from the case hitDiff1 (c.f. table 4.2) at the time step (corresponding roughly to the time step displayed in last frame of fig. 4.9 (a)). The conditionally averaged quantities are in qualitative agreement with the fully resolved DNS and experimental results of Holzner et al. [29]. The turbulent kinetic energy falls less rapidly than the vorticity as a result of the irrotational fluctuations beyond the TNTI.

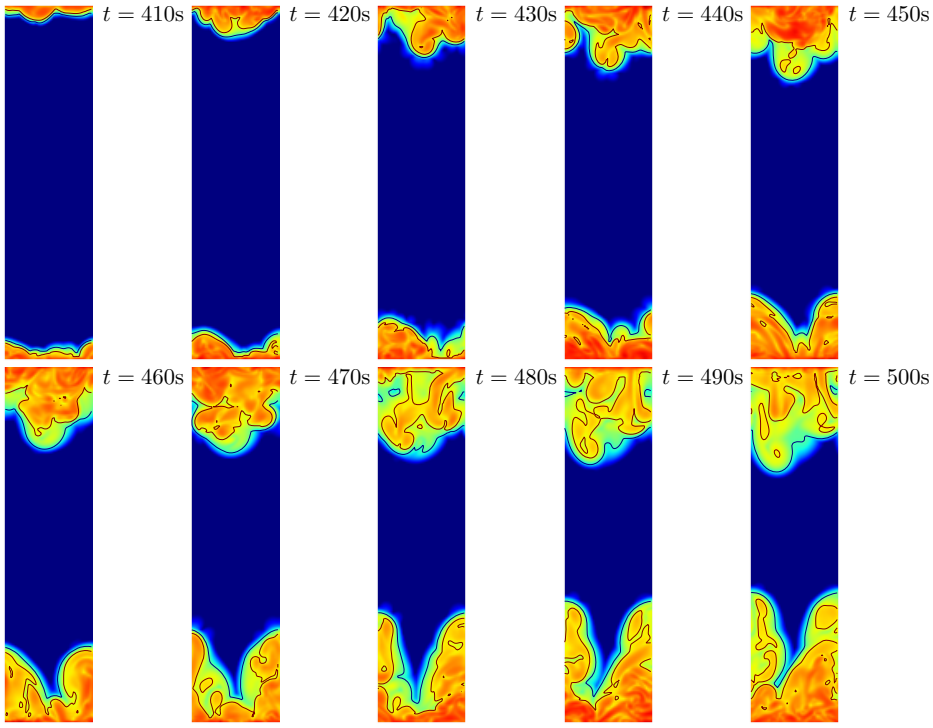

(a) hitDiff2

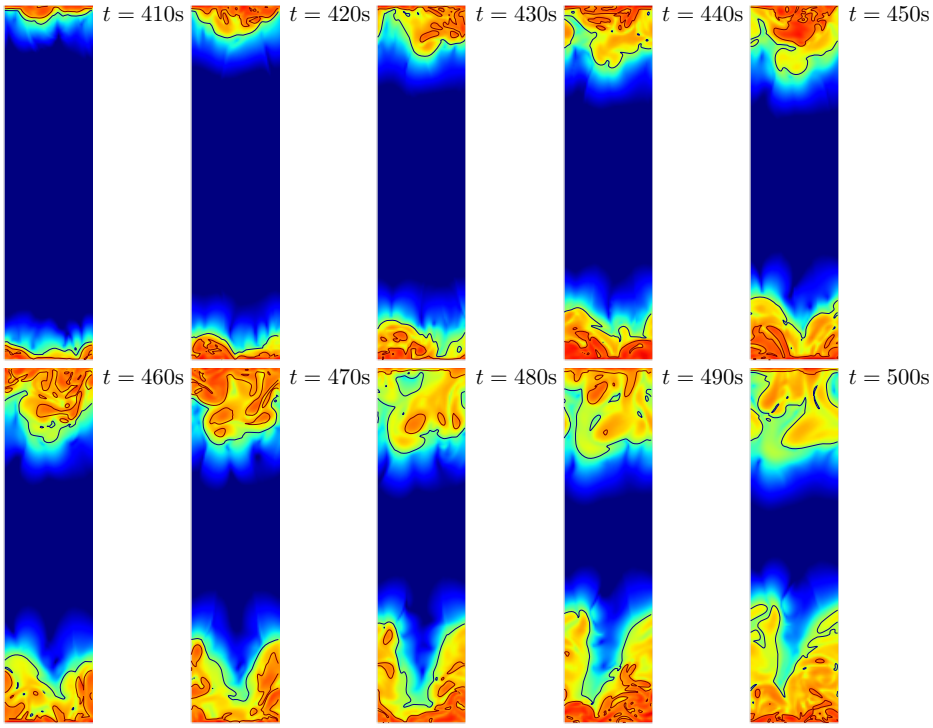

(b) hitDiff6

Figure 4.9.: Resolved vorticity magnitude for cases turbulent diffusion at $Re_\lambda \sim 60$ for two different resolutions (see table 4.2). Superimposed are contour lines of the normalized vorticity magnitude at values 0.001 and 0.01 (see fig. 4.8).

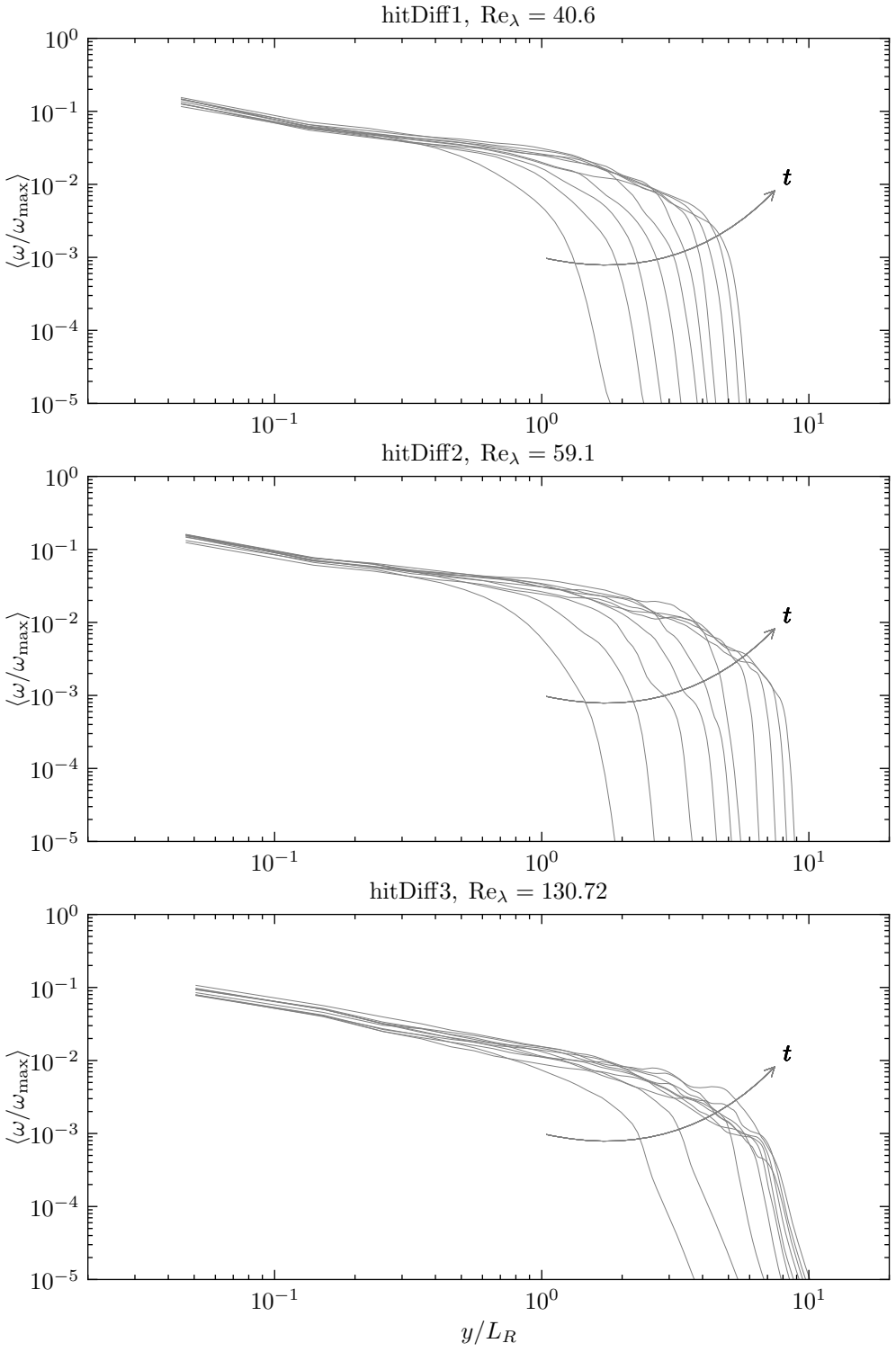

Figure 4.10.: Profile of the vorticity magnitude of the resolved velocity field for free-diffusion cases at grids of size $4 \times N^3 = 4 \times 64^3$.

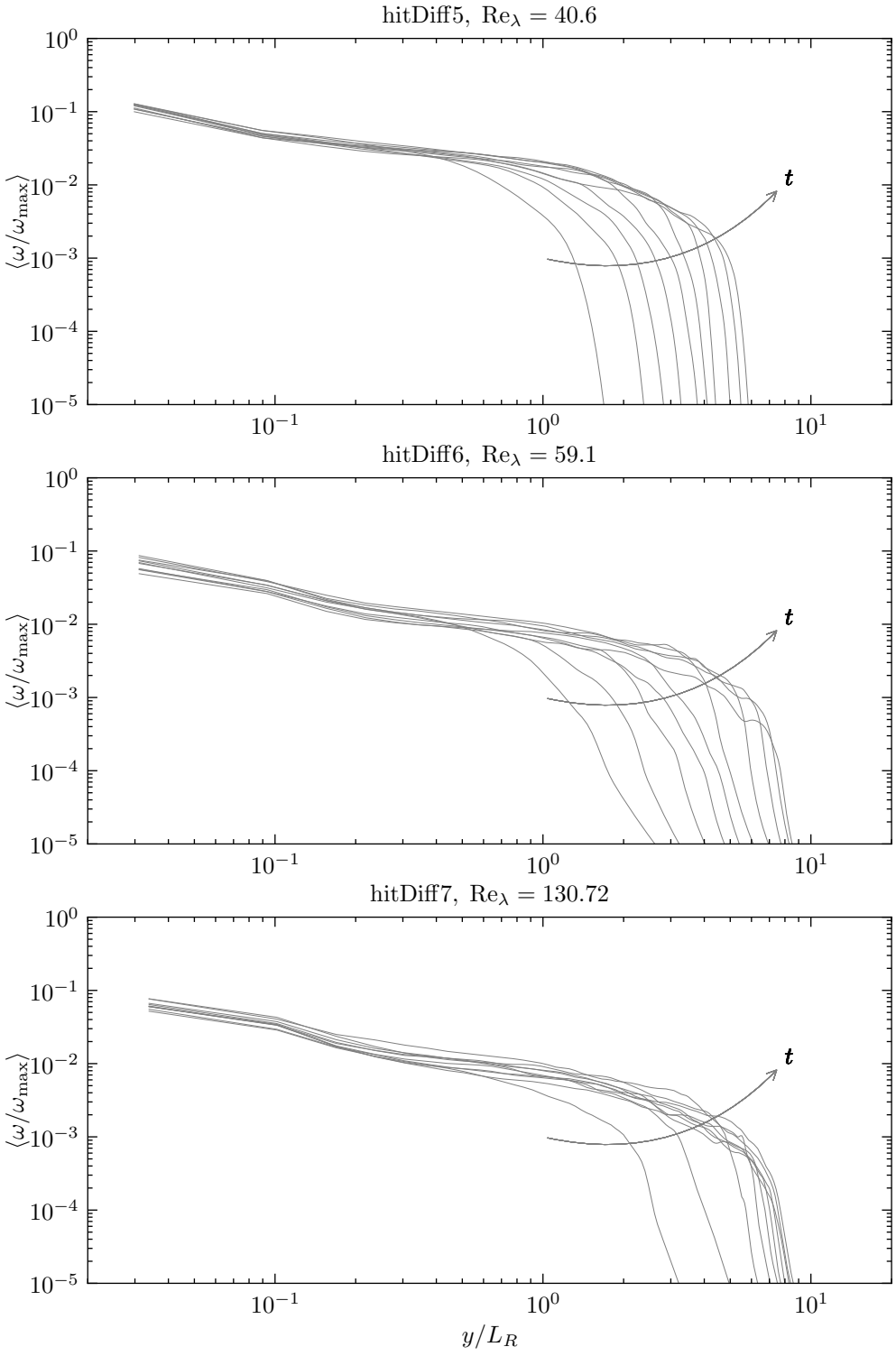

Figure 4.11.: Profile of the vorticity magnitude of the resolved velocity field for free-diffusion cases at grids of size $4 \times N^3 = 4 \times 96^3$.

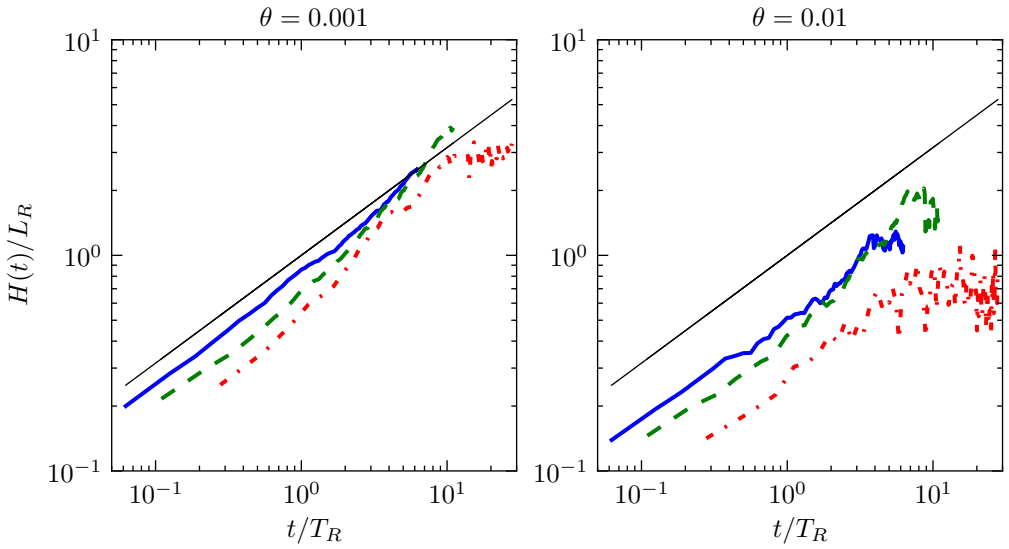

Figure 4.12.: TNTI propagation for the turbulent diffusion at the coarse grid for three different Reynolds numbers (cases hitDiff1 – solid line, hitDiff2 – dashed line and hitDiff3 – dash-dotted line line in table 4.2).

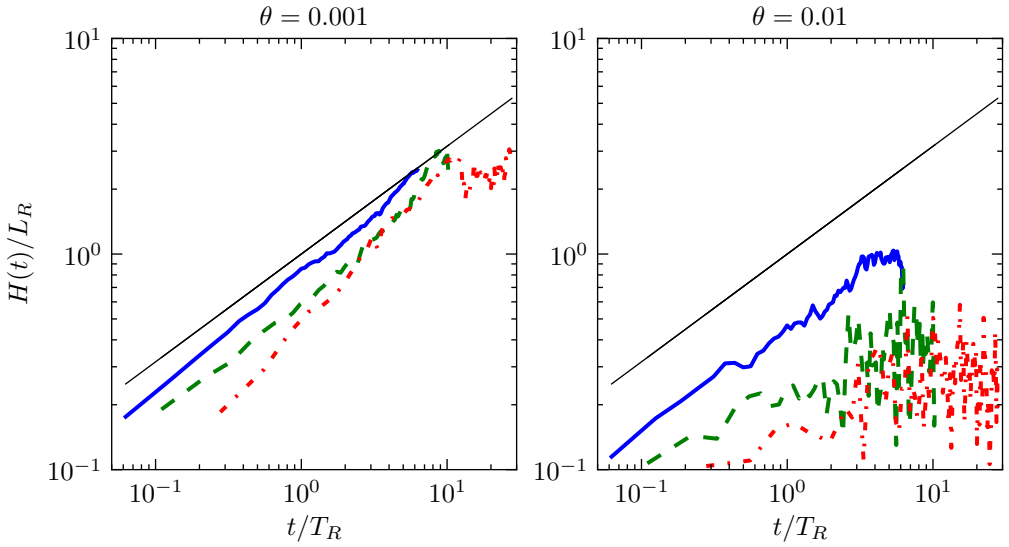

Figure 4.13.: TNTI propagation for the turbulent diffusion at the fine grid for three different Reynolds numbers (cases hitDiff5 – solid line, hitDiff6 – dashed line and hitDiff7 – dash-dotted line in table 4.2).

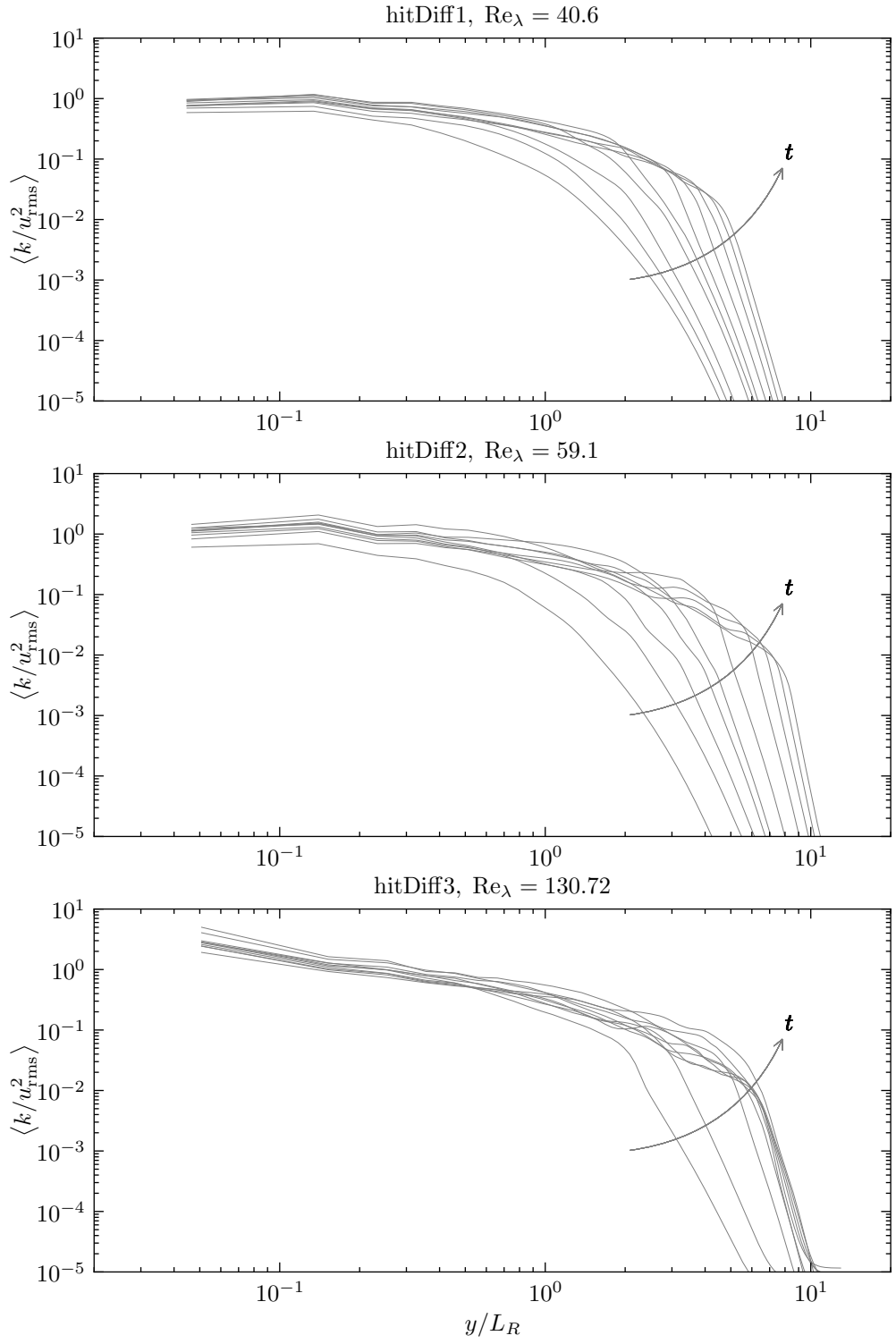

Figure 4.14.: Profiles of the total kinetic energy

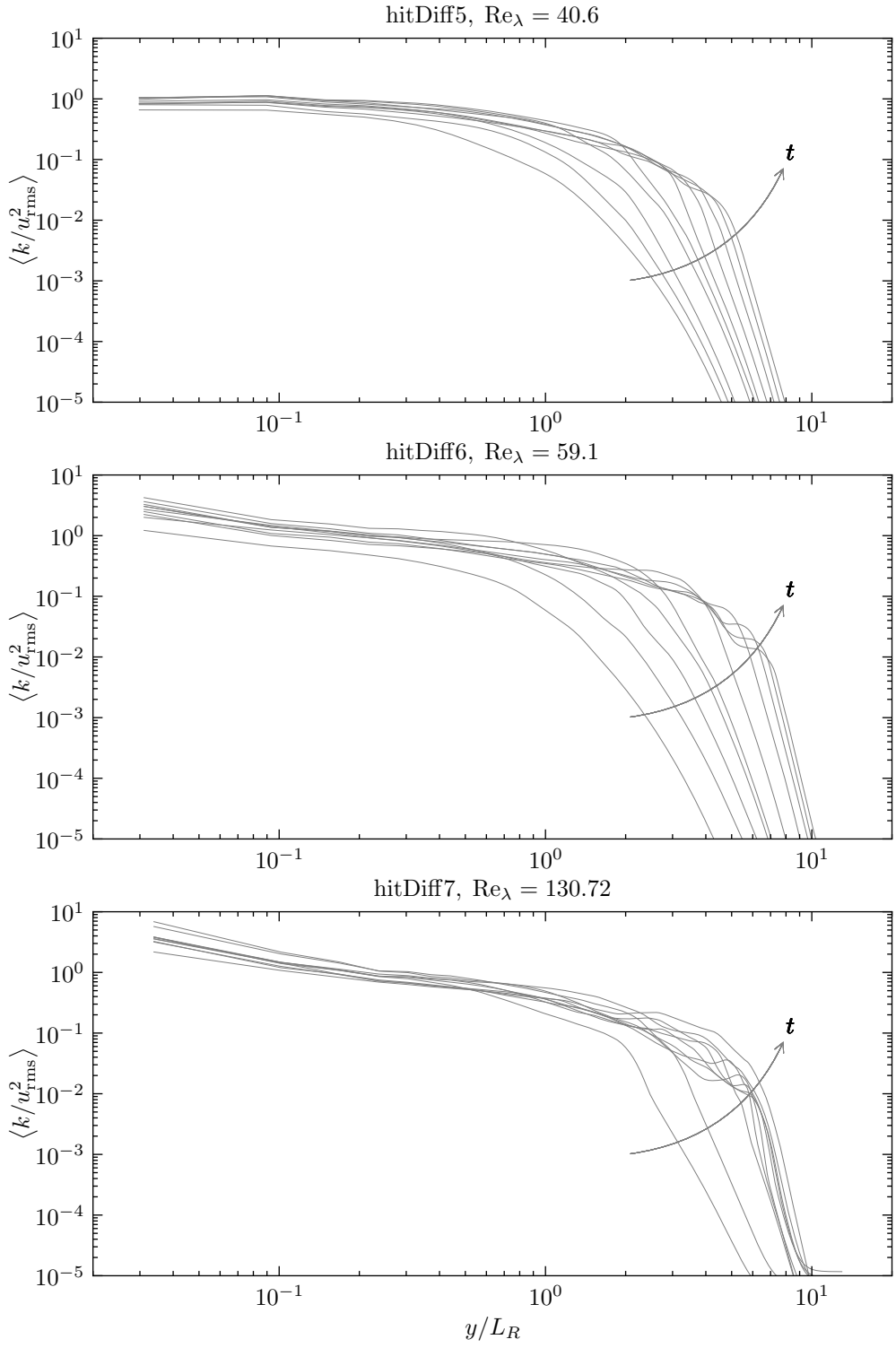

Figure 4.15.: Profiles of the total kinetic energy

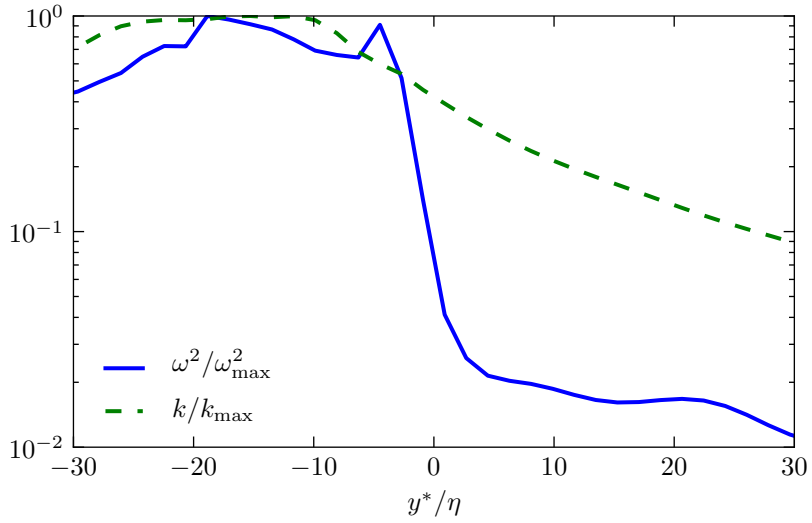

Figure 4.16.: Conditionally averaged profiles of enstrophy and resolved kinetic energy.

4.6. LES of confined turbulent diffusion

Oberlack and Guenther [56] argue that the breaking of symmetry of scaling of space may be achieved by imposing periodic boundary conditions on the sides such that the integral length scales may not grow along the propagation direction. Preliminary simulations have been performed with the sides in x and z directions, L_x and L_z, smaller than the length scale of the resolved motions (see fig. 4.5) and by using fractions of the original planar velocity field as boundary conditions on the forcing boundaries. However, this setup exhibits a significant mean flow on the forcing boundaries, which in turn destroys the statistically diffusive character of the computational setup. Reduction of the mean flow could only be achieved by *ad hoc* manipulations, which would presumably have an adverse effect on the statistics of turbulence at the forcing planes.

Another practical means to impose the symmetry breaking of scaling of space in the present setting is to keep the size of the computational domain intact, and to replace the periodic conditions on the sides of the computational domain with the free-slip boundary condition on velocity. The free-slip boundary condition dissallows flow through the boundary, but, in contrast with the no-slip boundary condition, shear stress or related vorticity, are not introduced. This setup is especially convenient in the present context as, then the TNTI detection criterion does not need to be modified. Results from the companion experimental study (see [41]) at the later stage of propagation of nominaly free turbulent diffusion fields substantiate this particular approach.

The free-slip boundary condition breaks isotropy of the Reynolds stress tensor and planar homogeneity of the computational setup. The study by Campagne et al. [5] discusses the effect of the free-slip boundary condition on the Reynolds stress and other statistics of diffusion of isotropic turbulence in a similar setting, where the diffusion of turbulence proceeds perpendicularly to the boundary. It may be argued that for the present case of turbulence sliding along the boundary these effects of inhomogeneity and anisotropy should not be as strong, and that the turbulence propagation should not be systematically dependent on these, local to the boundary and small-scale, blockage effects. Further investigations are needed in order to confirm this assumption.

Additionally, the present scaling law is explicitly confirmed in the study of a confined jet by Risso and Fabre [60]. The lateral integral length scales of a jet scale with its width and it lends itself easier to lateral confinement then the present case. Here, the size of the computational domain contains at least several integral length scales of turbulence and only with the growth of the length scales with the propagation one may expect direct effects of confinement to affect turbulence statistics.

Three cases have been computed at the smaller resolution; cases hitDiff1, hitDiff2, and hitDiff3 from table 4.2 have been used with a change of the boundary conditions on the side boundaries from periodic to slip. The three new cases are designated confHitDiff1, confHitDiff2 and confHitDiff3 and their correspondence to the forcing LES of HIT can be seen in table 4.2. Additionally, to investigate interaction of the grid spacing with the slip boundary condition, case confHitDiff2 is computed at an increased resolution, corresponding to the case hitDiff5 in table 4.2.

Figure 4.17 shows the evolution of the resolved vorticity magnitude for the case confHitDiff2, i.e. at $\mathrm{Re}_\lambda \sim 60$. There is a peculiar development of turbulence near the slip boundary which appears to be a result of this particular set of forcing boundary conditions.

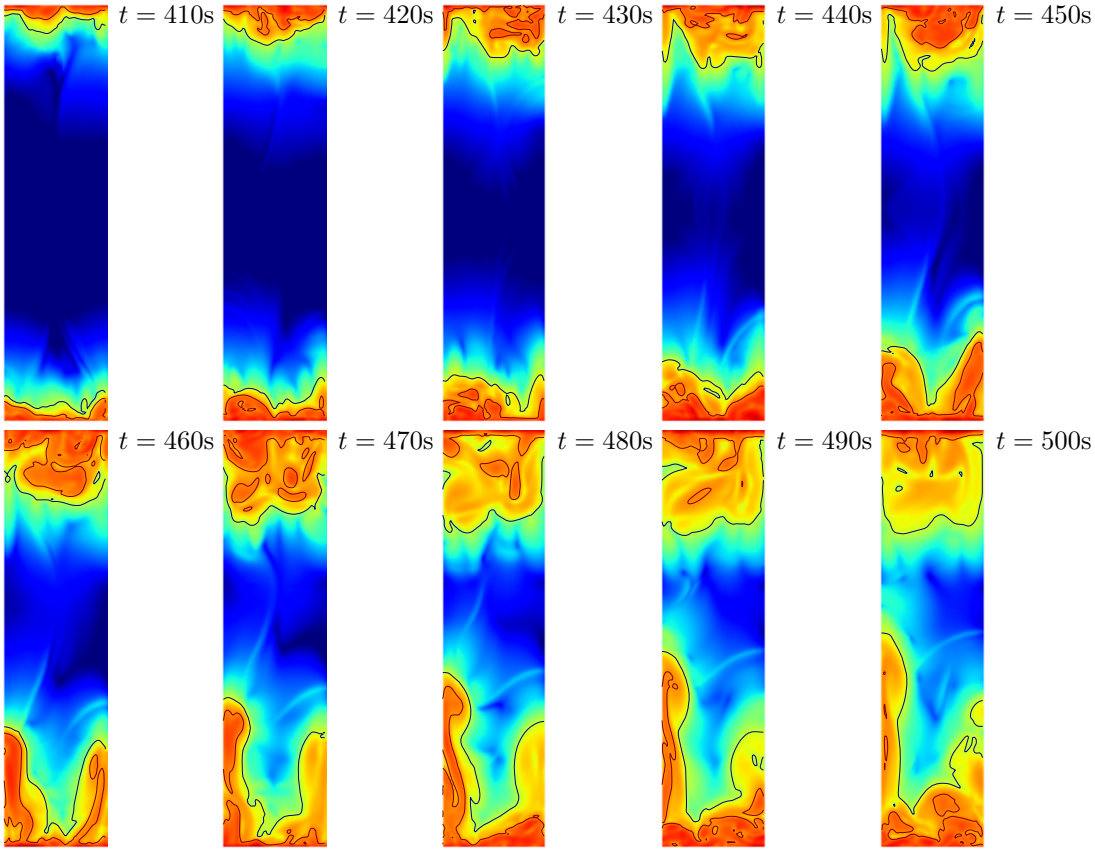

Figure 4.17.: Contours of the resolved vorticity magnitude in the midplane in z-direction for the confined case corresponding to lesHit2. Colors of the vorticity magnitude have been logarithmically scaled in the interval $\left[10, 10^{-4}\right]$, s^{-1}. Superimposed are contour lines of the normalized vorticity magnitude at 0.01 and 0.001.

Figure 4.18 displays the development of the averaged normalised vorticity profiles along the direction of turbulence propagation for the three cases of confined diffusion. Consistent with the contour plots of vorticity, at later times of propagation significant levels of averaged vorticity are present in flow regions far away from the forcing boundaries, and the drop in normalised vorticity profiles is much slower relative to the corresponding cases of free diffusion at initial propagation times. Profiles of the turbulent kinetic energy are consistent with the behavior of vorticity as shown in fig. 4.19.

Inspite of the fact that the TNTI position lines do not display the theoretically predicted logarithmic propagation, fig. 4.20 shows that the imposition of the slip boundary conditions supresses the overall propagation of turbulence in comparison to the free diffusion cases. This is consistent with the experimental results where turbulence propagation is considered at three different confinement widths, and turbulence spreading decreases with decreasing confinement width.

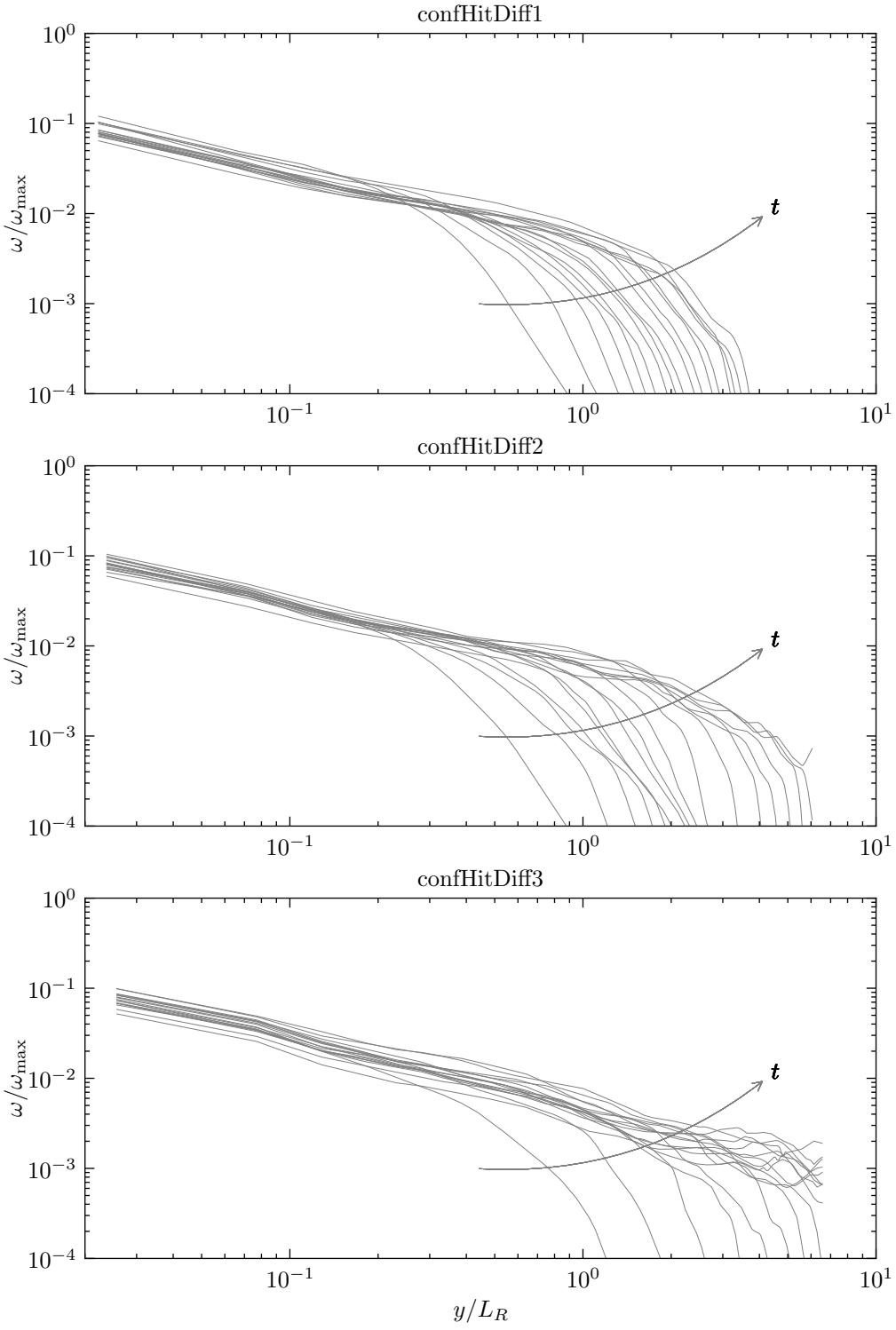

Figure 4.18.: Profile of the vorticity magnitude of the resolved velocity field

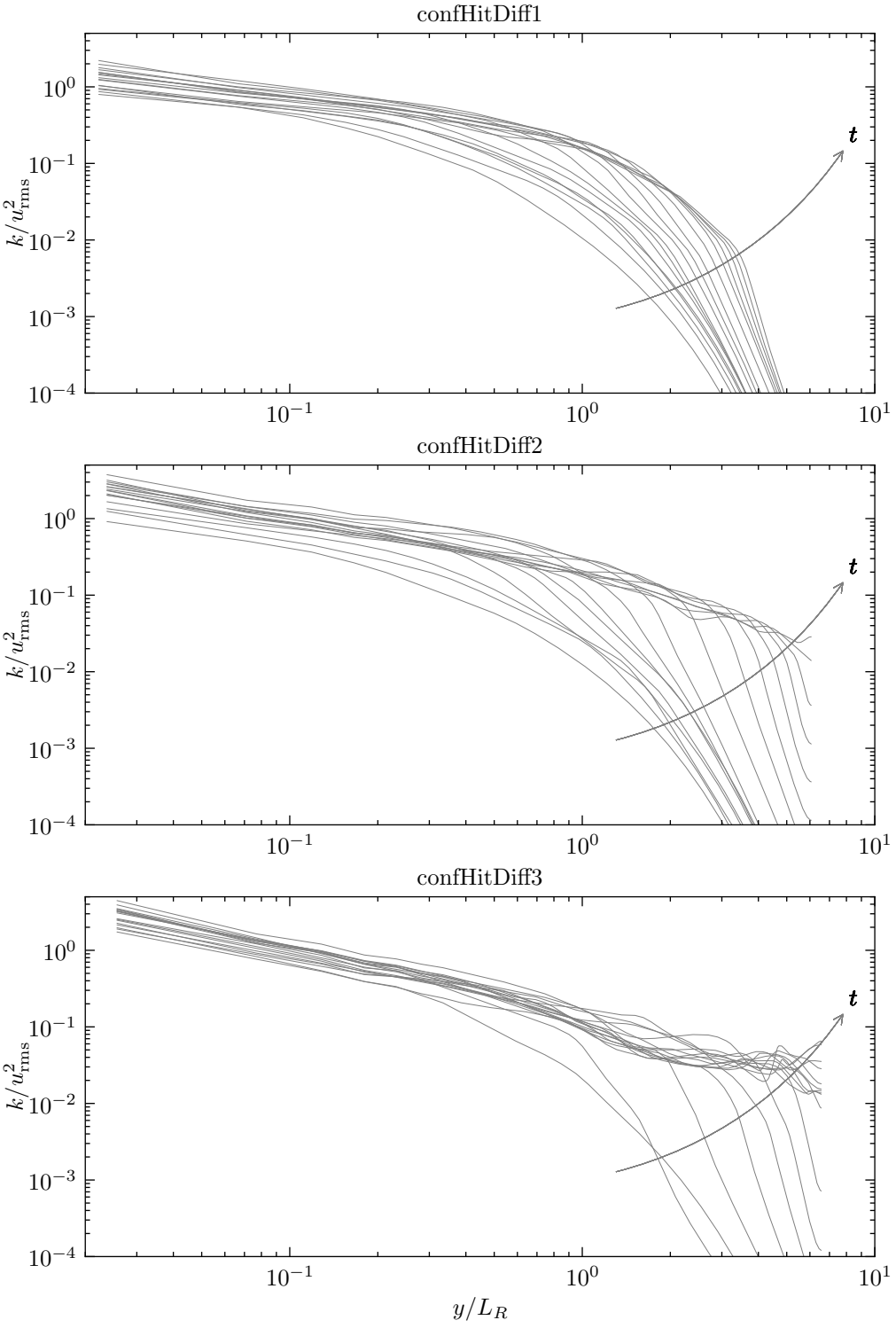

Figure 4.19.: Profile of the turbulent kinetic energy of the resolved velocity field

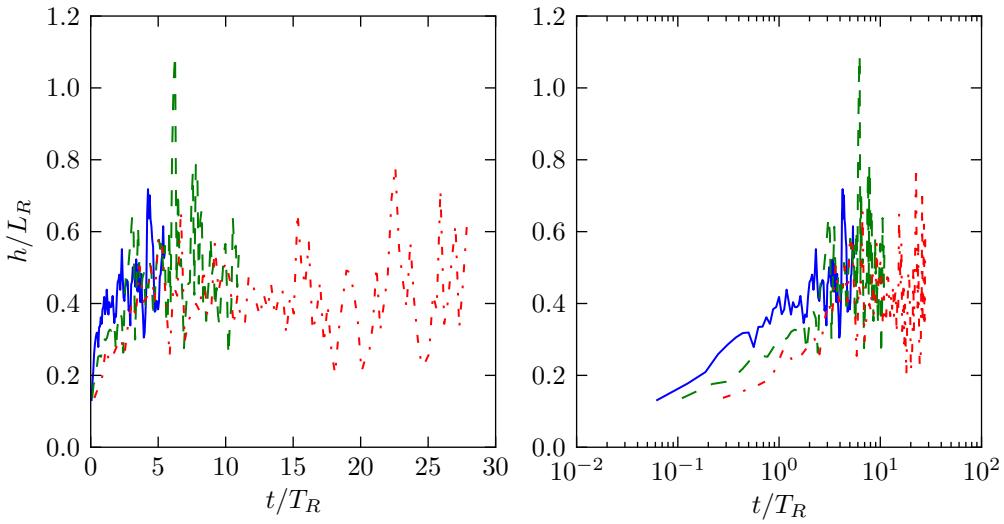

Figure 4.20.: Position of the TNTI for the three cases of confined turbulent diffusion (confHitDiff1 – solid, confHitDiff2 – dashed, confHitDiff3 – dash-dotted line) in linear and semilogarithmic plot.

4.7. LES of rotating forced homogeneous turbulence

Similarly to the DNS of forced rotating homogeneous turbulence, an LES of the case has rarely been reported in the literature in comparison to the non-rotating case. It is particularly difficult to apply the isotropic sub-grid scale models, i.e. eddy-viscosity models, at very small Rossby numbers for at least two reasons. First, rotation tends to inhibit the energy transfer from the large scales and therefore turbulence in general. Second, one of the main features of rotating turbulence is the appearance of anisotropy. In the range of moderate Rossby numbers, anisotropy is primarily distributed at the larger scales, while the smaller scales tend to remain isotropic. To summarize, rotation tends to increase the smallest energetic scales by decreasing the rate of dissipation, and thereby narrowing the span of energetically-relevant length scales. Simultaneously, anisotropy appears at the largest scales, and the range of scales affected by anisotropy increases with the rate of dissipation. It may be argued, based on these qualitative facts, that as long as the Rossby number remains in a moderate range, and the Reynolds number is high enough for a significant range of scales to exist, the eddy-viscosity models with the dynamic procedure may be utilized. This is especially valid for the dynamic procedure models, as they have been shown to be robust to the changes from turbulent to non-turbulent states, i.e. in the limit of laminar flow the dynamic procedure diminishes the turbulent viscosity. Figure 4.21 (a) shows the

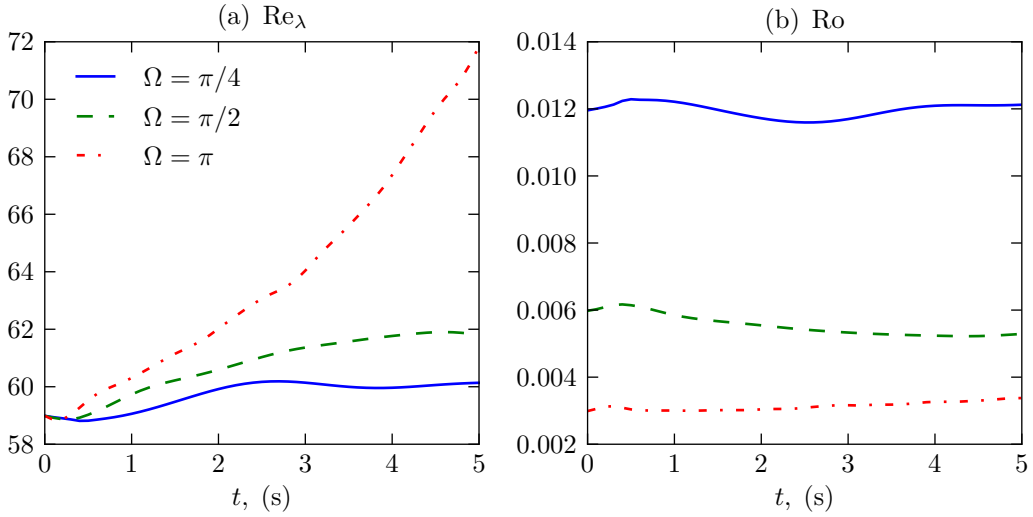

Figure 4.21.: (a) Reynolds number based on the Taylor microscale for LES of homogeneous forced rotating turbulence. (b) Rossby number.

development of the Reynolds number based on the Taylor microscale. The rotating simulation has been started from the initial LES of isotropic turbulence, and, as explained in the appendix B, forcing has been implemented by freezing the largest velocity scales. This setup is reflected in the increase of Re_λ, as the rate of dissipation is suppressed and the velocity scale is kept constant by the forcing. Figure 4.21 (b) displays the development of the Rossby number during the simulations. It evolves in a stable manner for the duration of the runs, even at the highest rotation rate.

In fig. 4.22 the development of the turbulent kinetic energy and the normalized dissipation

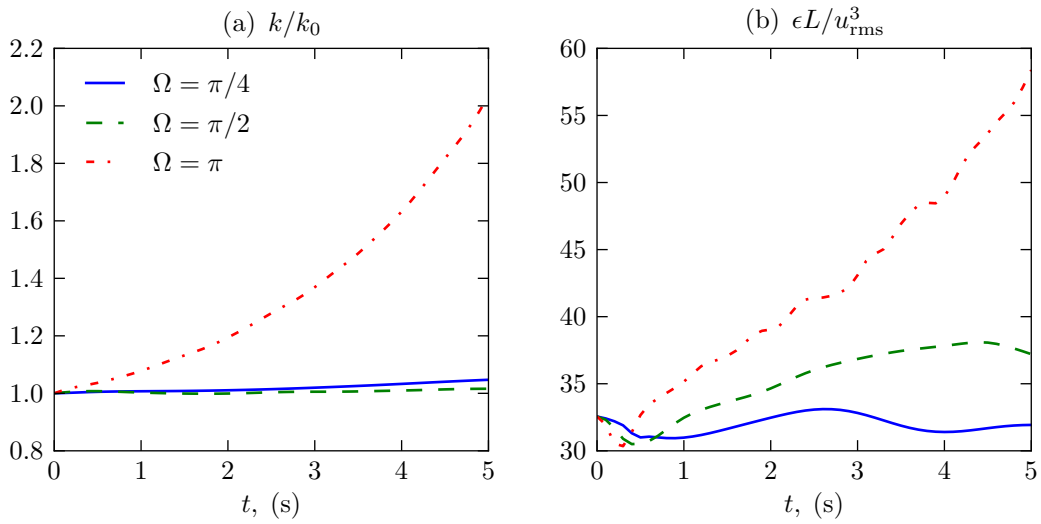

Figure 4.22.: (a) Evolution of the turbulent kinetic energy in LES of homogeneous forced rotating turbulence. (b) Normalized dissipation rate.

rate is displayed. The energy grows in comparison to the non-rotating case as a consequence of a reduced dissipation rate. This effect is stronger with the increasing rate of rotation. The normalized dissipation rate shows that the energy supply by the largest scales is adjusted, at least for the Fourier modes which are not frozen, in order to create shifted equilibrium as compared to the non-rotating case. In the case of the strongest rotation the adjustment of the non-frozen modes does not bring enough balance and the system is fully unsteady, i.e. energy grows unboundedly.

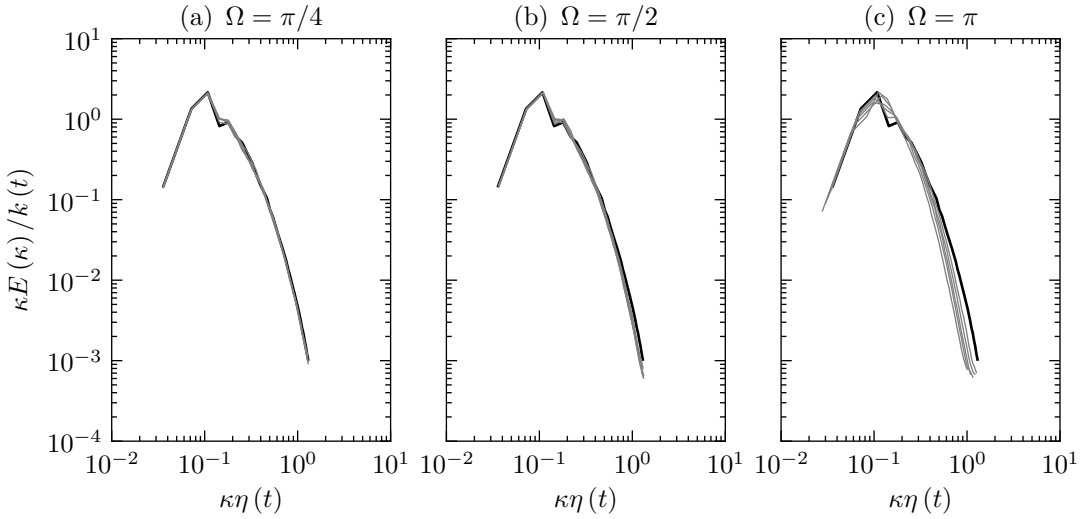

Figure 4.23.: Energy spectra evolution in LES of rotating homogeneous turbulence; thick line is the initial spectrum of isotropic turbulence

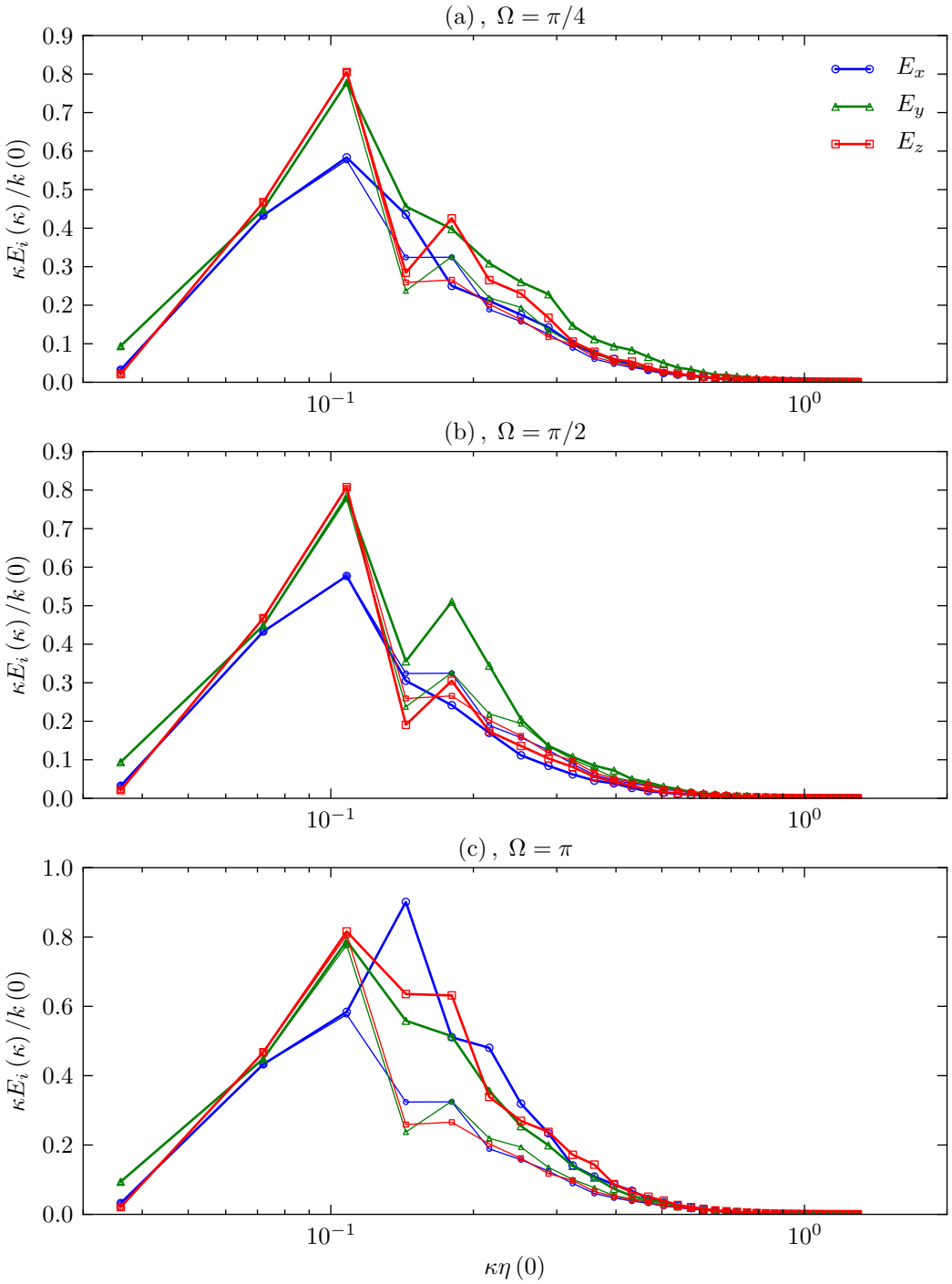

Figure 4.24.: One-dimensional spectra of component energies calculated at time $t\Omega = 0$ (isotropic turbulence, thin lines, small markers) and at $t\Omega = 3$ (rotating homogeneous turbulence, thick lines, large markers) for three rotation rates. Spectra are calculated by averaging squared coefficients of three-dimensional Fourier transform of the velocity component field withing wavenumber shells.

Figure 4.23 shows the evolution of the energy spectrum function, here normalized with the instantaneous volume averages of the turbulent kinetic energy and the Kolmogorov scale.

(It should be noted that the calculation of the energy spectrum function has been performed without considering the fact that, in the Fourier space, the turbulence energy is no longer equaly distributed in each direction of the wave-number vector.) In agreement with the increased Re_λ, apparent from fig. 4.23 is the decrease in the rate of energy transfer to the small scales as reflected by their decreased energy content relative to the non-rotating isotropic initial field. The rate of dissipation and the energy transfer to the smallest scales are both inversely proportional to the rate of rotation, although these quantities are no longer in equilibrium (as in isotropic turbulence) due to the appearance of the energy backscatter. The backscatter of energy is more pronounced as the Rossby number decreases, which is visible in the growth of the energy at the largest non-frozen wavenumbers.

Figure 4.24 shows the one-dimensional spectra of component energies for the three rotation rates. As evident from the subfigures (a) and (b), the energy cascade preferably transfers energy in the rotation direction at moderate rotation rates. At the highest rotation rate, the effect is masked by the backscatter of energy to the components perpendicular to the rotation rate, signaling the anisotropic two-componentality.

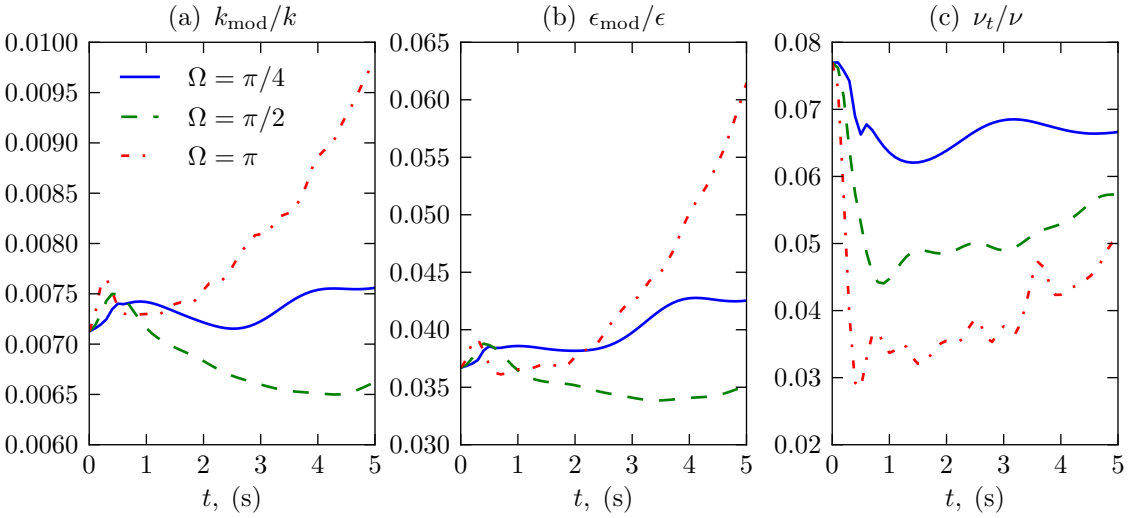

Figure 4.25.: Modeled quantities in LES of rotating homogeneous turbulence and their dependence on the rate of rotation; (a) turbulent kinetic energy, (b) rate of dissipation, (c) turbulent viscosity.

4.8. LES of rotating turbulent diffusion

In this section results of LES of turbulent diffusion in a rotating frame are presented. The runs have been performed starting from zero initial fields, and perturbing the velocity at the boundary using planar velocity profiles sampled from the simulations described in the previous section. The simulations have been performed for three different rotation rates: $\pi/4$, $\pi/2$ and π. For all simulations, a grid of size $(N_x, N_y, N_z) = (64, 256, 64)$. A localized dynamic Smagorinsky model, as described in section 2.2, has been applied as a subgrid stress model. Simulations are performed with an adaptive time-step, with a Courant number limit of 0.3. For all three rotation rates, the total simulation time spanned at least three rotation periods. The mean flow, calculated by averaging velocity over homogeneous and statistically symmetric planes, has been verified to contribute, in the energy sense, less than 1% to the total kinetic energy for all times along the inhomogeneous direction. The contribution is only noticable in the vicinity of the turbulence forcing boundaries and increases with the rotation rate.

The most significant characteristic of the numerical setup of rotating turbulent diffusion, is the fact that the boundary perturbations tend to propagate into the initially calm fluid much faster than in the non-rotating case. The reason for this is presumably the ability of a fluid in a rotating frame to support the inertial waves. Inertial waves are solutions to the Navier-Stokes equations when $\mathrm{Ro} \ll 1$, so that all the terms in the equation vanish except for the pressure gradient and the Coriolis acceleration. In the present case, the inertial wave effects compete with the nonlinear turbulence effects, but the inertial wave motions are faster to affect the initially still fluid.

The second major characteristic of this case, relative to the case of non-rotating diffusion, is the essentially transient energy at the boundary of the domain. This is an inevitable consequence of the adaptation of turbulence to the rotating frame, as shown in the previous section. The choice has been made here so that the non-rotating and the rotating cases are mutually related as are the accompanying experiments [41] (in the experiments, the parameters of the oscillating grid are kept the same as in the non-rotating case, meaning that the turbulence is essentially modulated due to the decrease in the rate of dissipation).

Figure 4.26 shows isocontours of the turbulent kinetic energy obtained from several snapshots during turbulence development. The columnar structure of the isocontours clearly shows the dominance of the structuring effect that is imposed by rotation over the disorderly structure dictated by turbulence. A similar impression of the structuring can be gained from the two-dimensional contours of the vorticity magnitude shown in fig. 4.27.

Figure 4.28 shows the temporal development of the averaged normalized vorticity with respect to the propagation direction. Contrary to the cases of free and confined diffusion, a certain vorticity level is reached at larger distances from the forcing boundaries even at the earliest times of turbulence propagation, which may be explained by propagation of perturbations by means of inertial waves.

Profiles of the turbulent kinetic energy are shown in fig. 4.29. Here it is evident that the kinetic energy has wave-like propagation, and that the amplitude of the waves increases with the rotation rate. The existence of waves is expected from the theoretical considerations of fluid motions in a rotating frame of reference. However, in the current computational setup, one cannot easily distinguish wave components caused by the turbulence fluctuations

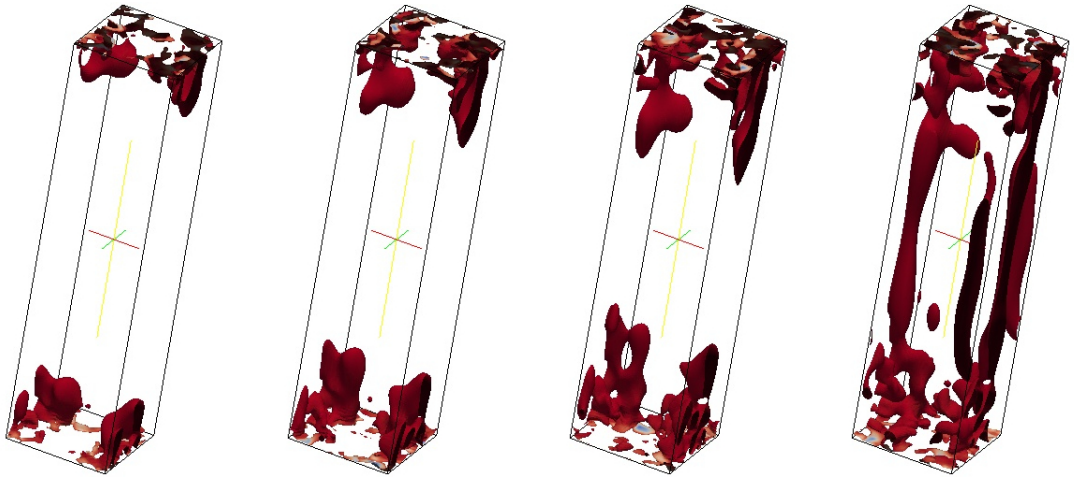

(a) (b) (c) (d)

Figure 4.26.: Isocontours of the turbulent kinetic energy

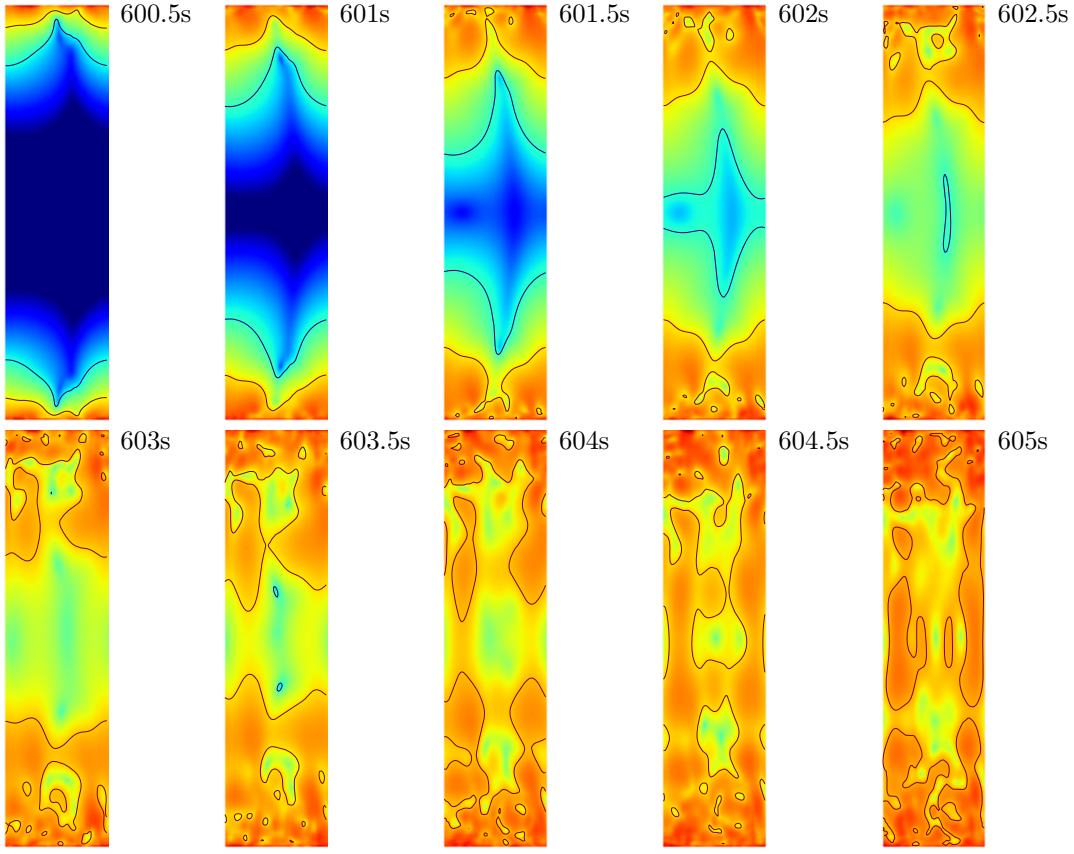

Figure 4.27.: Profile of the vorticity magnitude of the resolved velocity field

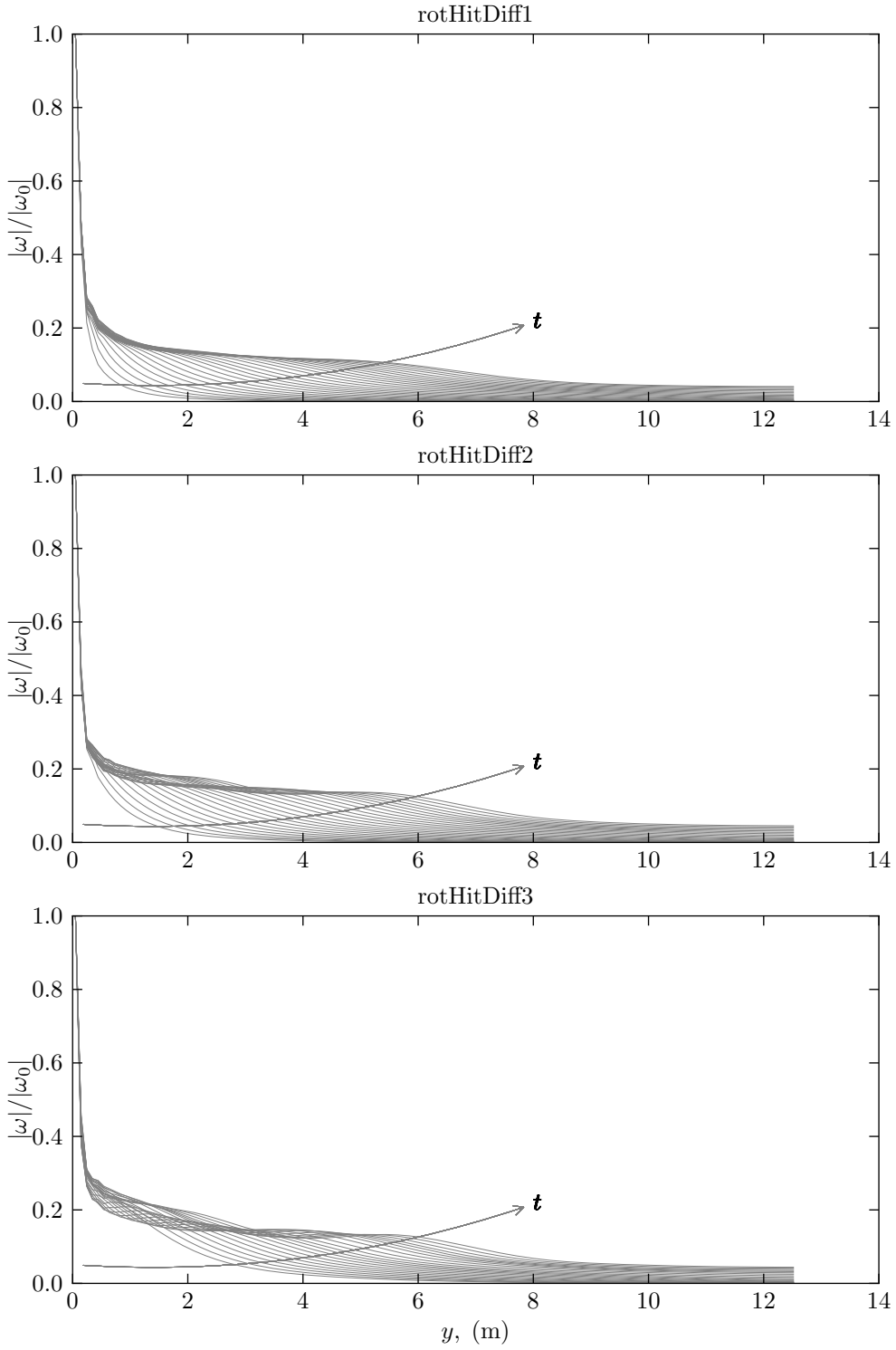

Figure 4.28.: Profile of the vorticity magnitude of the resolved velocity field

from those induced by the mentioned errors resulting from the pressure velocity coupling algorithm at the boundary. Further investigations are needed in order to clarify this issue.

TNTI positions as a function of time normalized with the rotation rate are shown in fig. 4.30. At initial times of propagation the TNTI position lines scale well, while at later times the scaling is good for the cases with higher rotation rates. TNTI position does not correspond very well to the theoretically predicted exponential function and presumably much higher Reynolds numbers are needed in order to suppress the dominance of the rotation effects in order to obtain results close to the theoretical scaling law for rotating turbulent diffusion.

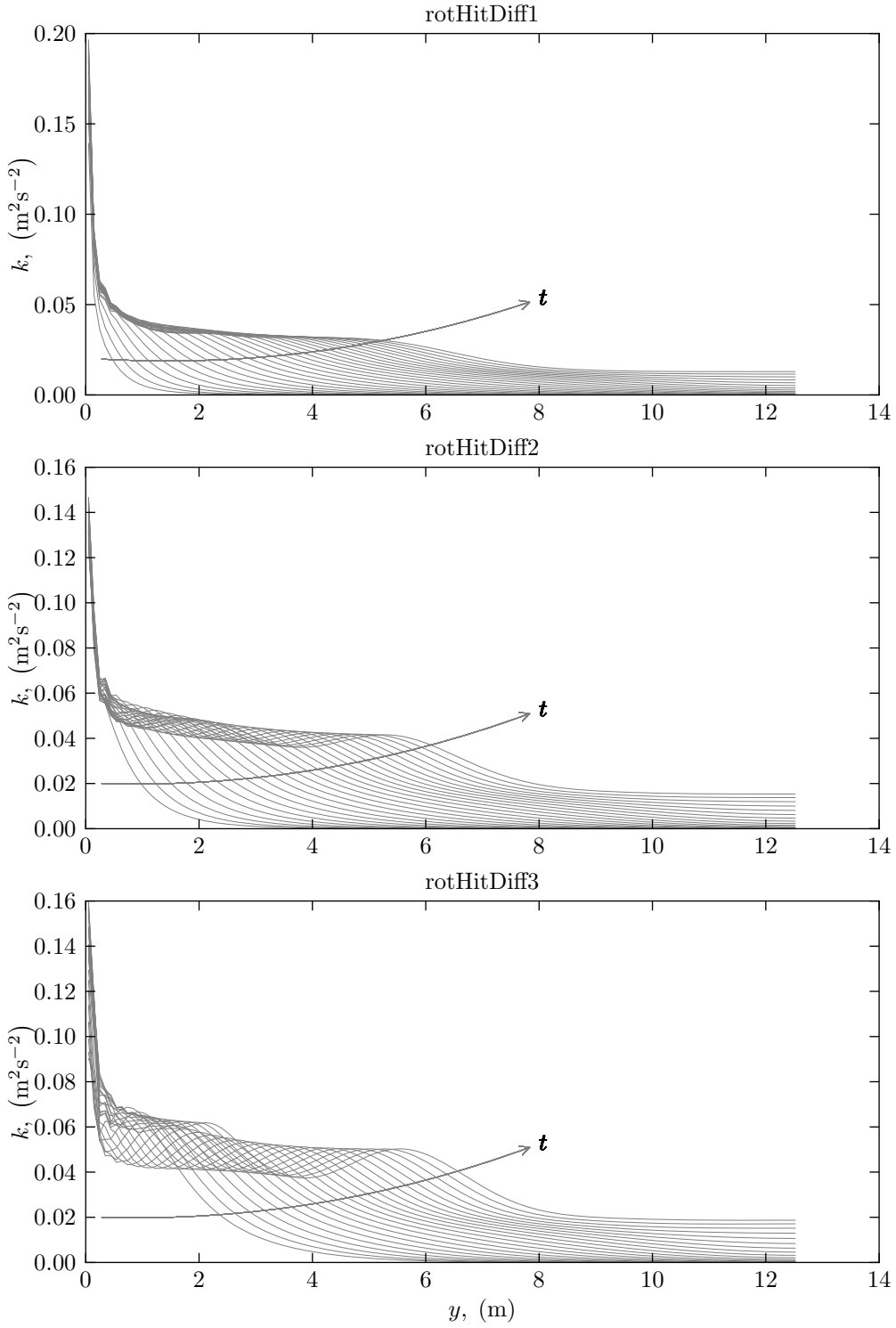

Figure 4.29.: Profile of the total kinetic energy

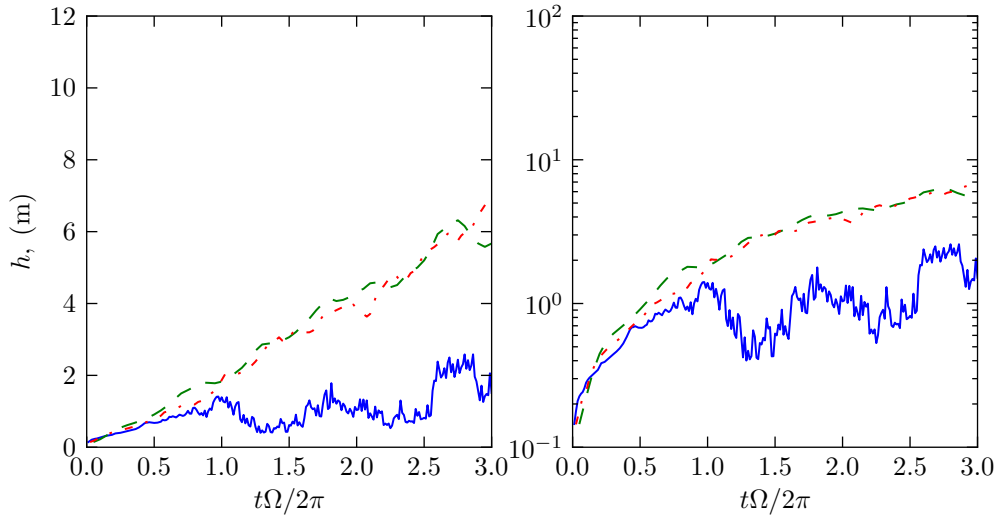

Figure 4.30.: Propagation of the TNTI for the three rotating cases (rotHitDiff1 – solid, rotHitDiff2 – dashed, rotHitDiff3 – dash-dotted lines) in a linear and semilogarithmic plot.

5. Conclusions and outlook

The present work investigated performance of large-eddy simulations for the case of pure turbulent diffusion, distinguishing between free diffusion, diffusion under the influence of confinement and diffusion in a rotating frame of reference.

From the point of view of simulation settings, turbulent diffusion simulation has been realized using pre-computed fields of isotropic and homogeneous turbulence as boundary conditions to the otherwise calm velocity fields. In the present nominally second-order FVM, this setup has shown some weaknesses regarding the interaction of the non-uniform and unsteady boundary conditions with the pressure velocity coupling algorithm. The consequences of the weaknesses appear however to be confined to the narrow region close to the boundary, and the rest of the computational domain remains free of numerically incurred deficiencies. This problem is of general nature in the second-order FVMs, but the lack of convection dominance makes it apparent and significant in the present case. Related to this, it has been found by observation that the explicitly discretized rotational form of the convective term in the momentum equation serves to reduce numerical inaccuracies at the forcing boundaries compared to the discretization of the nonlinear term utilizing the most widely used second-order convective schemes.

Precursor DNS runs were performed to test the FVM turbulence-generation algorithm in which only the large-scale forcing is manipulated in the spectral space. DNS of isotropic turbulence show good agreement with the results available in the literature, as far as the kinetic energy spectrum, Taylor-microscale Reynolds number, Kolmogorov scales, alignment of vorticity and eigenvectors of the rate of strain tensor, and joint PDF of the invariants of the rate of strain tensor are concerned. The DNS results of rotating forced homogeneous turbulence, being in comparison with the related isotropic non-rotating case relatively scarce in the literature, has confirmed generally accepted properties of rotating turbulence: depletion of dissipation rate relative to the isotropic turbulence under equally strong large-scale forcing, related steepening of the inertial range slope of the energy spectrum and tendency of suppression of turbulence in favor of a more structured flow aligned with the rotation axis. Due to the constant strength of the forcing, the case is unsteady, causing an increase in total energy with time, and future work should address a dissipation dependent forcing algorithm which would keep overall energy levels invariant with time, but presumably lead to faster suppression of turbulence. It is shown that forced rotating homogeneous turbulence is characterized by relative asymetry in the PDFs of vorticity and strain rate eigenvectors, which is related to the asymetry in cyclonic and anticyclonic longitudinal vortices, and this is another point left for future investigations. The low order of the method relative to the pseudo-spectral and higher-order finite difference algorithms usually applied in these types of simulations is shown to be viable and adequate at least for low-order statistics, and could be efficiently utilized in testing LES modeling and numerical discretization approaches.

Related LES of isotropic and rotating homogeneous turbulence retain robustness and accuracy in terms of low order statistics of precursor DNS calculations. In terms of energy spectra at different Reynolds numbers LES performs satisfactorily when compared to the available data from literature. Underresolution in LES of homogeneous turbulence at higher Reynolds number results in an overall reduction of the total dissipation rate, so the filter width should be a low multiple of the Kolmogorov length scale in order to obtain physically realistic turbulence in low-order physical space simulations. The anisotropy caused by rotation in LES of homogeneous rotating turbulence opens a question of appropriateness of LES models, developed with the assumption of small scale isotropy, in this context. It is argued here that at high enough Reynolds and Rossby numbers the anisotropy prevails at the largest scales and that the currently widely available LES models perform reasonably well. Quantitative statements on performance of currently available LES models in rotating turbulence require further investigations in this field.

Detection of the TNTI has been investigated in terms of different criteria used for discriminating between turbulent and non-turbulent parts of the flow field. Currently available results on TNTI detection have invariably used fully resolved either experimental or DNS flow data to compute vorticity, which is the flow variable best suited for discriminating between the rotational turbulent and irrotational non-turbulent flow regions. Dependance of vorticity in resolved LES velocity fields on resolution poses a significant challenge in determining an unambiguous value of vorticity to be used as a threshold in TNTI detection. In the present work, LES vorticity suitably normalized by the maximum absolute value of vorticity available in the simulation field has been used as a non-dimensional field for interface detection. Using the so-called threshold averaged (normalized) vorticity function as a quantity inherent to the partially turbulent flow fields, it has been shown that it is possible to obtain a value of the normalized vorticity threshold which is coarsely unique over the resolutions and Reynolds numbers considered in the present study. The issue of TNTI detection from LES fields is not resolved, and efforts made towards its resolution could prove to be useful in improving future LES models for partially turbulent flows.

LES of free turbulent diffusion has been simulated at three Reynolds numbers, each at two different grid resolutions. Profiles of the normalized vorticity of the resolved velocity fields (as described in the previous paragraph) exhibit a change in slope of decay with the distance from the forcing plane, as evidenced from the double-log graphs of profiles at different propagation times, i.e. decay of vorticity along a moderate slope, characteristic of fully turbulent part of the field, changes over a short distance (characteristic of the thickness of the interface) to a steep slope of decay consistent with the lack of vorticity in the non-turbulent region. The shape and intensity of the normalized vorticity profiles are preserved over the range of Reynolds numbers and LES resolutions, suggesting that this computational setup is generally suitable for simulations of pure turbulent diffusion. Turbulent fronts, as detected from the averaged normalized vorticity profiles, behave roughly in agreement with the power law predicted in the theoretical analysis, and are qualitatively consistent with the reported experimental and DNS results in the framework of the present project at initial times of propagation. At later times and at larger distances of the TNTI from the forcing plane, dissipation becomes the dominant quantity in the energy balance and propagation of turbulence is suppressed relative to the initial power law. Profiles of the averaged turbulent kinetic energy are consistent with the experimental findings, i.e. the change of slope of the turbulent kinetic energy is milder compared to the profiles of vorticity, which reflects the existence of the irrotational fluctuations outside of the turbulent part of the flow.

LES of confined turbulent diffusion has been simulated by imposing slip boundary conditions on the lateral sides of the computational domain, as opposed to the periodic boundary conditions on the corresponding sides in free diffusion simulations. The non-permeability of the lateral sides of the domain should inhibit the growth of the length scales with the distance from the forcing. However, the original isotropic turbulence from which the forcing planes are extracted contains several integral length scales of turbulence within the computational domain, and the slip boundaries confine the growth only to later times of propagation, where dissipation, which is not considered in the theoretical analysis, and the interaction of turbulence with the slip boundaries play a significant role. This is reflected in front propagation of the confined case which does not follow the profiles predicted in the theoretical analysis and reported in the experiments. A remedy could be to create a degenerate case of 'isotropic' turbulence box where integral length scales of turbulence would be comparable in size to the computational domain and use thereby obtained turbulence fields as forcing boundaries for turbulent diffusion.

LES of rotating turbulent diffusion has been performed by solving LES equations in a rotating frame of reference, using planar samples of velocity from the LES of rotating homogeneous turbulence at forcing boundaries. Simulations are performed at three different rotation rates at the Reynolds and Rossby numbers in the range of those proposed in the accompanying experiments. Under the influence of propagation of inertial waves perturbations at the forcing boundaries quickly spread throughout the computational domain. The waves increase in amplitude as the velocity magnitude at the forcing planes increase which is evident in the profiles of the averaged turbulent kinetic energy along the propagation direction. The errors in the velocity fields very close to the boundaries also have an influence on triggering inertial waves, however without much more detailed simulations the influences of pressure-velocity coupling, LES modeling and turbulence forcing cannot be distinguished, and this should be a subject of future analysis. Isocontours of the turbulent kinetic energy and pressure show appearance of columnar regions aligned with the rotation axis, which is consistent with descriptions of rotating turbulence found in the available literature. Turbulence propagation, as detected by the normalized averaged vorticity, is comparatively slower and confined to the region close to the forcing planes. TNTI propagation does not compare well with the one predicted by the theoretical analysis and the experimental results which are also mutually incompatible. It is assumed that much higher Reynolds numbers are needed in order to create the fields with an adequate balance of inertial and Coriolis forces to meet the constraints of the theoretical analysis of this case. Contrary to the theoretical findings which predict an upper limit to the propagation of turbulence, at later times of simulations vorticity is also pronounced away from the boundaries.

In a brief analysis of RANS modeling approaches it is shown that the currently available models conform to the scaling laws of the free turbulent diffusion, and that further work is required to sensitize RANS models to the constraints of confinement and rotation.

A. Symmetry analysis of the two-point correlation equation

The description of the method of symmetry analysis of the two-point correlation equation in the statistically unsteady, one-dimensional configuration shall be given here. This is essentially a detailed summary of available results. However, the method of symmetry analysis of differential equations can be considered non-standard and the procedure to obtain the solutions has been only tersely outlined elsewhere, e.g. [55], so a reiteration of the concepts is warranted. Additionally, the detailed specification of the assumptions sets the stage for a meaningful discussion of the simulations and consequent conclusions.

A.1. Basic concepts

A *point symmetry* (as opposed to other more complicated symmetries, a discussion of which is out of scope of the present report) of a system of differential equations is a transformation of independent and dependent variables which leaves the system of equations invariant, i.e. the equations have the same form in the new variables. An equivalent way to define a symmetry is that it is a transformation which maps solutions to solutions. A system of differential equations is treated algebraically, to quote Cantwell [6]

> In group theory differential equations are viewed as surfaces in a higher-dimensional (jet) space whose coordinates are the independent variables, the dependent variables, and all the possible derivatives of one with respect to the other[...]

Within the tangent (jet) space, a particular solution is a subset of the hyper-surface defining the system of differential equations. A symmetry maps a particular solution to another one, thereby leaving the whole solution set, i.e. the hyper-surface within the tangent space, invariant.

A.1.1. Example – Invariance of an ODE under translation

To illustrate the concepts introduced it is instructive to look at a simple example Cantwell [6] of an ordinary differential equation (ODE)

$$\frac{dy}{dx} - e^{(x-y)} = 0 \tag{A.1}$$

The surface representing the set of solutions to the eq. (A.1) is shown in fig. A.1 (a tangent space of an ODE is amenable to simple illustrations as the tangent space is three-dimensional). The translation group (translation symmetry)

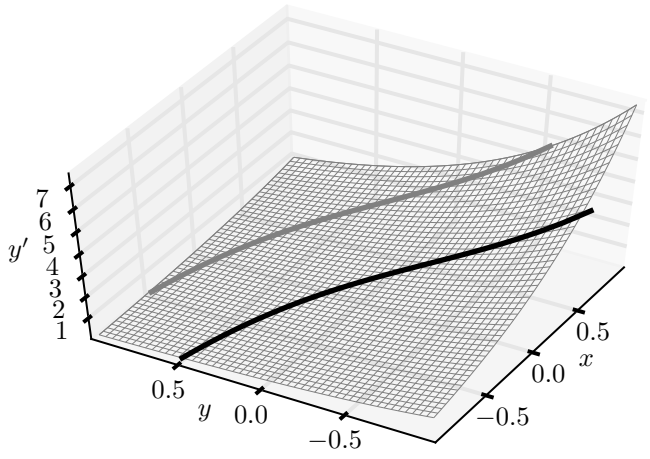

Figure A.1.: Hyper surface (thin gray wireframe) representing the set of solutions to eq. (A.1), together with the particular solution (thick black line) $C = e^y - e^x$ for $C = 2$ and its transformation (thick gray line) by eq. (A.2) for $s = 0.5$

$$\begin{aligned} \tilde{x} &= x + s \\ \tilde{y} &= y + s \end{aligned} \tag{A.2}$$

leaves the equation invariant. This equation is easily solved to obtain the general solution

$$e^y - e^x = C \tag{A.3}$$

Symmetry transformation eq. (A.2) leaves the eq. (A.1) invariant as

$$\frac{d\tilde{y}}{d\tilde{x}} = e^{(\tilde{y}-\tilde{x})} \tag{A.4}$$

which is easily confirmed by direct substitution. Hence, the transformation maps solutions to solutions as shown in fig. A.1.

A.1.2. Example – Invariance of a PDE under scaling

A more involved example Cantwell [6] (which is also of direct relevance to the present case of turbulent diffusion) is that of a PDE describing one-dimensional unsteady diffusion of heat in a conductive solid given by the following initial-boundary value problem

$$\frac{\partial u}{\partial t} = \kappa \frac{\partial^2 u}{\partial x^2} \tag{A.5}$$

with initial and boundary conditions

$$\begin{aligned} t < 0 &: \; u(0,t) = 0, \; u(\infty,t) = 0 \\ t \geq 0 &: \; u(0,t) = u_0, \; u(\infty,t) = 0 \end{aligned} \tag{A.6}$$

Here, in accordance with the previous example tangent space, spanned by the coordinates

$$\left(u, t, x, \frac{\partial u}{\partial t}, \frac{\partial u}{\partial x}, \frac{\partial^2 u}{\partial t^2}, \frac{\partial^2 u}{\partial x^2}, \frac{\partial^2 u}{\partial x \partial t}\right)$$

is 8-dimensional (and difficult to visualize). The eq. (A.5) is a hypersurface of the above space. The transformation

$$\begin{aligned} \tilde{x} &= e^s x \\ \tilde{t} &= e^{2s} t \\ \tilde{u} &= u \end{aligned} \tag{A.7}$$

is a symmetry of the eq. (A.5) as may be verified by direct substitution. Hence, solutions to eq. (A.5) are mapped to other solutions by the transformation eq. (A.7). Also, by direct inspection it is concluded that the initial and boundary conditions are also invariant under the transformation.[1] For problems invariant under the scaling symmetry it is possible to construct the *similarity variables* (which are also invariant under scaling). For the heat conduction problem the similarity variables are[2]

$$v = \frac{u}{u_0},\ \xi = \frac{x}{\sqrt{\kappa t}} \tag{A.8}$$

and the problem reduces to a boundary value ODE

$$\frac{d^2 v}{d\xi^2} + \frac{\xi}{2}\frac{dv}{d\xi} = 0 \tag{A.9}$$

with boundary conditions

$$v\,(0) = 1,\ v\,(\infty) = 0 \tag{A.10}$$

Figure A.2 displays a numerical solution to eq. (A.5). Graph (a) of fig. A.2 shows temperature profiles for different times, and in (b) the same solutions are represented in a log-log plot. Graphs in (c) and (d) represent the curves from (a) and (b) respectively in the similarity variables, or equivalently solution to the ODE eq. (A.9). As an aside to the discussion of symmetries proper, graph (e) of fig. A.2 shows the positions of the *heat front* with time for arbitrary definitions of the front positions in the subplot (d). It is concluded that the front propagation behavior is a direct consequence of the similarity variables constructed from the original system, and that different criteria for discriminating the front position are in this respect of no significance.[3]

[1] Were the far boundary in x placed at a finite distance the transformation would no longer keep the boundary conditions (and hence the initial-boundary value problem) invariant (see Cantwell [6]). This is the case in every one-dimensional unsteady conduction problem in nature and the symmetry transformation is not strictly applicable. However, it may provide sufficiently accurate solutions for initial times where the far-boundary may still be regarded as infinitely distant. An additional restriction posed by boundary conditions is that the value at $x = 0$ is prescribed at a point, for otherwise symmetry of an ideal problem would in general be broken. These points are of relevance for the turbulent diffusion case.

[2] Formally, it is not necessary to include problem parameters u_0 and κ in the definition of the similarity variables, but this practice is common because it makes the subsequent reduced problem parameter-independent.

[3] For different thresholds on the similarity variable, front-position curves differ by a constant factor. Additionally, values of the original variable u at which this threshold is reached are time-dependent. This conclusion is of direct relevance for the problem of turbulent diffusion.

As a conclusion, the heat conduction problem eq. (A.5) is invariant under scaling transformation eq. (A.7). Similarity variables eq. (A.8) (constructed here by an educated guess) make it possible to reduce the original problem to an ODE. Solutions to the problem are self-similar, meaning that when they are plotted in the similarity variables they collapse to one curve. The solutions are invariant under a change in parameters of the problem when expressed in the non-dimensionalized similarity variables (i.e. u_0 and κ are not present in the reduced problem directly).

A.1.3. The method of symmetry analysis

This section presents a brief description of the Lie-algorithm. For more details the textbooks Bluman et al. [3], Cantwell [6], Stephani [65] are of interest. The method of symmetry analysis of differential equations, also known as the Lie-group method, is a means for algorithmically obtaining all symmetries admitted by a given system. One proceeds as follows

- A system of differential equations is given.
- A general symmetry of the system is postulated in the *infinitesimal generator* form. The infinitesimal generator form is an equivalent representation for one-parameter point symmetries which form a group with respect to the operation of a composition of functions. The infinitesimal generator form of transformations features unknown functions of the dependent and independent variables.
- The infinitesimal transformation is *prolonged*, so that the transformations of the derivatives are expressed in terms of the infinitesimal generators.
- A condition of invariance is invoked, which represents an overdetermined system of linear differential equations for the unknown functions within the infinitesimal transformation. This system of equations, also know as the *determining system*, is solved.
- The symmetry transformations are constructed from the calculated infinitesimal generators.

For a general system of PDEs this is a tedious procedure, and for this reason the method has not been utilized to its full power until recently. Advances in symbolic computation have made it possible to develop software systems which implement the Lie-algorithm, and enable calculation of symmetries of a given system of differential equations automatically.[4]

The Lie-algorithm yields point symmetries of a system of differential equation if they exist. Knowledge of such symmetries is later used for simplifications of the original system or under special circumstances for obtaining solutions. Of particular interest are *invariant solutions* which are solutions of the original system satisfying the *invariant surface condition*. In contrast to a general solution, an invariant solution is mapped to itself by a symmetry. Invariant solutions signify that the phenomenon described by the original system of equations is *self-similar*.

[4]For a proprietary system see, e.g. http://math.usask.ca/~cheviakov/gem/ or http://arxiv.org/abs/1004.3339, and as an open-source alternative there is e.g. http://www.latrobe.edu.au/mathstats/department/dimsym/index.html.

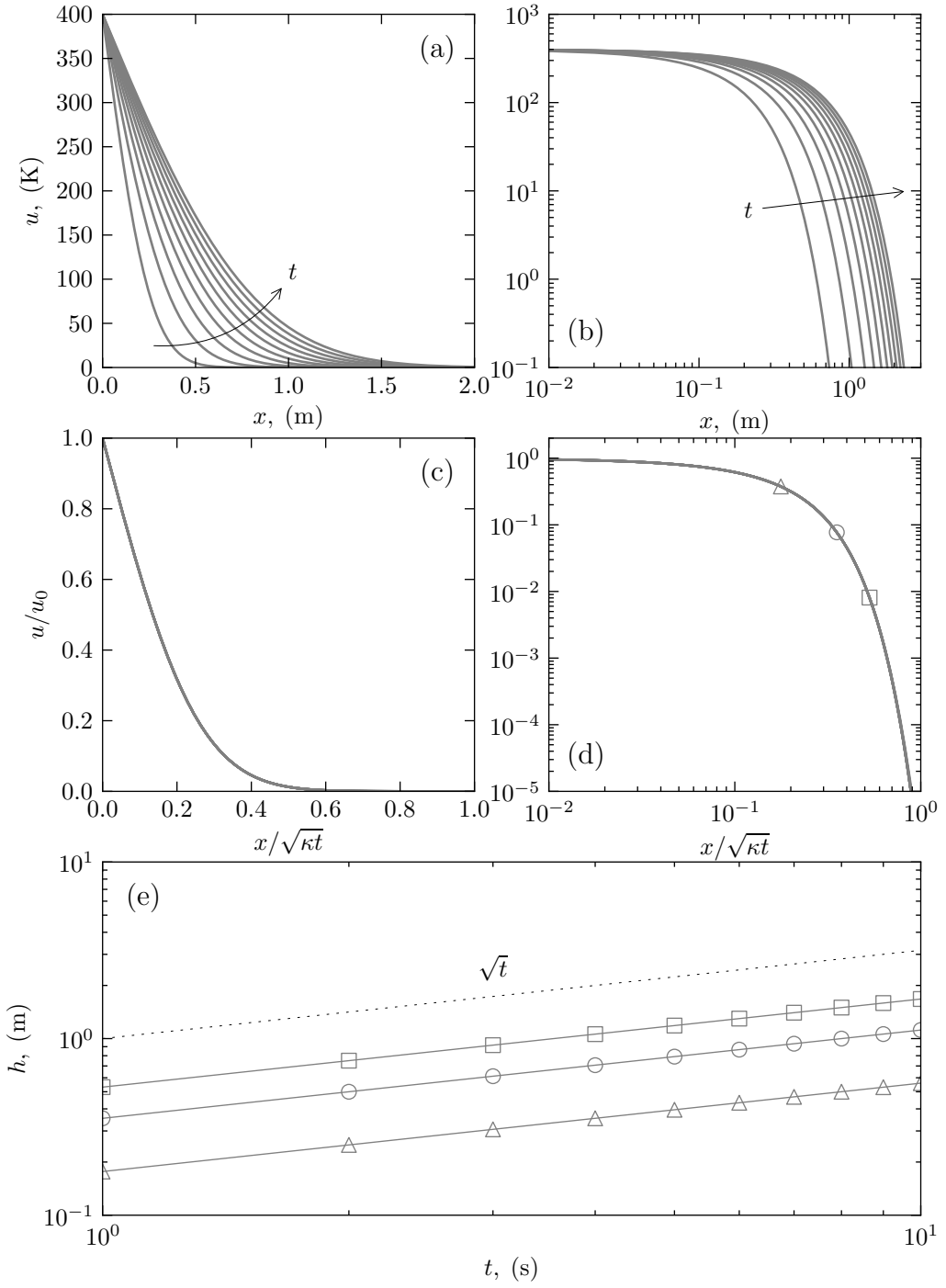

Figure A.2.: Numerical solution to the heat conduction problem eq. (A.5) for $u_0 = 400\text{K}$ and $\kappa = 0.02\text{m}^2\text{s}^{-1}$: (a) solution for 10 times in physical coordinates, (b) solution in log-log plot, (c) solution in similarity coordinates, (d) graph (c) in log-log plot, together with arbitrarily selected locations where heat front is considered to reside, (e) position of heat front with time for the criteria chosen in (d)

To summarize, given a system of differential equations, the Lie-algorithm enables calculation of transformations of the independent and the dependent variables which leave the system of equations invariant in the sense described above. Given the set of calculated symmetries, one is able to compute the set of *similarity variables* which is in general smaller than the set of the independent and dependent variables of the original system. The set of similarity variables, when substituted in the original system, yields a new simpler system of differential equations. It is important to note that the algorithm considers the system of equations only and its properties in its tangent space. For initial-boundary-value problems additional constraints in terms of the boundary conditions are introduced which also need to be invariant under the calculated set of symmetries in order to be applicable to the obtained solutions.

A.2. Two-point correlation equation for turbulent diffusion

A.2.1. Exact governing equations

The results presented here are derived from [54, 56]. The exact equation for the two-point correlation tensor (in Cartesian coordinates) reads

$$\begin{aligned}\frac{\bar{\mathrm{D}}R_{ij}}{\bar{\mathrm{D}}t} + R_{kj}\frac{\partial\langle U_i\rangle}{\partial x_k} + R_{ij}\frac{\partial\langle U_j\rangle'}{\partial x_k} + \left[\langle U_k\rangle' - \langle U_k\rangle\right]\frac{\partial R_{ij}}{\partial r_k} \\ + \frac{\partial\langle pu_j\rangle}{\partial x_i} - \frac{\partial\langle pu_j\rangle}{\partial r_i} + \frac{\partial\langle u_i p\rangle}{\partial r_i} \\ -\nu\left[\frac{\partial^2 R_{ij}}{\partial x_k\partial x_k} - 2\frac{\partial^2 R_{ij}}{\partial x_k\partial r_k} + 2\frac{\partial^2 R_{ij}}{\partial r_k\partial r_k}\right] \\ + \frac{\partial R_{(ik)j}}{\partial x_k} - \frac{\partial}{\partial r_k}\left[R_{(ik)j} - R_{i(jk)}\right] + 2\Omega_k\left[e_{kli}R_{lj} + e_{klj}R_{il}\right] = 0\end{aligned} \tag{A.11}$$

where R_{ij} is given by eq. (1.19), and the following holds

$$\langle pu_i\rangle = \langle p(\mathbf{x},t)u_i(\mathbf{x}+\mathbf{r},t)\rangle \tag{A.12}$$

$$\langle u_i p\rangle = \langle u_i(\mathbf{x},t)p(\mathbf{x}+\mathbf{r},t)\rangle \tag{A.13}$$

$$\langle U_i\rangle' = \langle U_i\rangle(\mathbf{x}+\mathbf{r},t\rangle \tag{A.14}$$

The above equation may be extended by the kinematic conditions (utilizing the continuity equation)

$$\frac{\partial R_{ij}}{\partial x_i} - \frac{\partial R_{ij}}{\partial r_i} = 0 \tag{A.15}$$

$$\frac{\partial R_{ij}}{\partial r_j} = 0 \tag{A.16}$$

$$\frac{\partial\langle pu_i\rangle}{\partial r_i} = 0 \tag{A.17}$$

$$\frac{\partial \langle u_j p \rangle}{\partial x_j} - \frac{\partial \langle u_j p \rangle}{\partial r_j} = 0 \tag{A.18}$$

Additionally, the following non-local functional relationships hold

$$R_{ij}(\mathbf{x}, \mathbf{r}, t) = R_{ji}(\mathbf{x} + \mathbf{r}, -\mathbf{r}, t) \tag{A.19}$$

$$\langle p u_j \rangle (\mathbf{x}, \mathbf{r}, t) = \langle u_j p \rangle (\mathbf{x} + \mathbf{r}, -\mathbf{r}, t) \tag{A.20}$$

Taking the divergence of the eq. (A.11), one obtains Poisson equations for the pressure-velocity two-point correlations. The eqs. (A.11) to (A.20) together with the Poisson equations represent the system of equations which govern behavior of R_{ij} in a turbulent flow.

A.2.2. Separation of scales

In the following let the turbulent Reynolds number, defined as

$$\mathrm{Re}_t = \sqrt{k}\ell/\nu \tag{A.21}$$

be large, where the integral length scale is

$$\ell = \frac{1}{k} \int_V R_{kk} \frac{\mathrm{d}^3 r}{r^2} \tag{A.22}$$

and k is the turbulent kinetic energy. Large Re_t means that there exist scales between the Kolmogorov scale, defined as

$$\eta = \left(\nu^3/\epsilon\right)^{1/4} \tag{A.23}$$

and the integral length-scale ℓ which may be considered independent of viscosity, or equivalently that the two-point correlation tensor is independent of viscosity for separations of the order of these scales. Let eq. (A.11) be non-dimensionalized with ℓ and $\sqrt{k}$. Taking the limit $1/\mathrm{Re}_t \to 0$ one obtains the large-scale two-point correlation equation

$$\begin{aligned} \frac{\bar{\mathrm{D}} R_{ij}}{\bar{\mathrm{D}} t} + R_{kj} \frac{\partial \langle U_i \rangle}{\partial x_k} + R_{ij} \frac{\partial \langle U_j \rangle'}{\partial x_k} + \left[\langle U_k \rangle' - \langle U_k \rangle \right] \frac{\partial R_{ij}}{\partial r_k} \\ + \frac{\partial \langle p u_j \rangle}{\partial x_i} - \frac{\partial \langle p u_j \rangle}{\partial r_i} + \frac{\partial \langle u_i p \rangle}{\partial r_i} \\ + \frac{\partial R_{(ik)j}}{\partial x_k} - \frac{\partial}{\partial r_k} \left[R_{(ik)j} - R_{i(jk)} \right] + 2\Omega_k \left[e_{kli} R_{lj} + e_{klj} R_{il} \right] = 0 \end{aligned} \tag{A.24}$$

(Here, the nomenclature is deliberately ambiguous, as in the above equation the non-dimensionalized variables are denoted by the same symbols as the variables in the previous section, to avoid unnecessary proliferation of symbols.) References [27, 53, 54, 56] contain further relationships on the quantities which may be derived from the large-scale R_{ij}, such as the Reynolds stress, the turbulent dissipation rate, etc.

A.2.3. Governing equations in the turbulent diffusion case

At the level of two-point moments the setting of the shear-free diffusion is confined to the (x_1, r_1, r_2, r_3, t)-space of independent variables, where x_1 is the spatial coordinate in direction of propagation of turbulence, r_1 is the projection of the two-point separation vector $\mathbf{r}$ to the direction of propagation, and r_2, r_3 are components of its projection to the plane normal to the propagation direction. In this space the eq. (A.24) reduces to

$$\begin{aligned} &\frac{\partial R_{ij}}{\partial t} + \delta_{i1}\frac{\partial \langle pu_j\rangle}{\partial x_1} - \frac{\partial \langle pu_j\rangle}{\partial r_i} + \frac{\partial \langle pu_i\rangle}{\partial r_j} + \frac{\partial R_{(i1)j}}{\partial x_1} \\ &-\frac{\partial}{\partial r_k}\Big[R_{(ik)j} - R_{i(jk)}\Big] + 2\Omega_k\left[e_{kli}R_{lj} + e_{klj}R_{il}\right] = 0 \end{aligned} \tag{A.25}$$

with the kinematic conditions

$$\delta_{i1}\frac{\partial R_{ij}}{\partial x_1} - \frac{\partial R_{ij}}{\partial r_i} = 0 \qquad \frac{\partial R_{ij}}{\partial r_j} = 0$$

$$\frac{\partial \langle u_1 p\rangle}{\partial x_1} - \frac{\partial \langle u_j p\rangle}{\partial r_j} = 0 \qquad \frac{\partial \langle pu_i\rangle}{\partial r_i} = 0$$

The above system of equations is accompanied by the Poisson equations for the pressure-velocity two-point correlations. At this point, the rotation term is disregarded. The above equations form the input system to the Lie-algorithm. The result of the algorithm are the following symmetries

$$T_{s_x} : t^* = t, x_1^* = e^{a_1}x_1, r_i^* = e^{a_1}r_i, R_{ij}^* = e^{2a_1}R_{ij}, \dots \tag{A.26}$$

$$T_{s_t} : t^* = e^{a_2}t, x_1^* = x_1, r_i^* = r_i, R_{ij}^* = e^{-2a_2}R_{ij}, \dots \tag{A.27}$$

$$T_{x_1} : t^* = t, x_1^* = x_1 + a_3, r_i^* = r_i, R_{ij}^* = R_{ij}, \dots \tag{A.28}$$

$$T_t : t^* = t + a_4, x_1^* = x_1, r_i^* = r_i, R_{ij}^* = R_{ij}, \dots \tag{A.29}$$

which represent scaling of space, scaling of time, translation in space, and translation in time respectively. Usage of the symmetries to obtain similarity variables is explained in e.g. [2, section 4.1.3] and [65, chapter 18]. Briefly, any linear combination of the obtained symmetries is also a symmetry. From the linear combination of symmetries, eqs. (A.26) to (A.29), separate infinitesimals may be computed. The invariant surface condition is invoked to determine the functional form of the invariant solutions and similarity variables. The invariant surface condition reads

$$\frac{dx_1}{a_1x_1 + a_2} = \frac{dt}{a_2t + a_3} = \frac{dr_\alpha}{a_1r_\alpha} = \frac{dR_{\alpha\beta}}{2\left(a_1 - a_2\right)R_{\alpha\beta}} = \cdots \tag{A.30}$$

where the Greek subscripts indicate that the summation convention does not apply, and the dots represent the ommited variables.

Based on the scaling parameters a_1 and a_2, the following cases are distinguished

- **Free turbulent diffusion,** $a_1 \neq 0$ **and** $a_2 \neq 0$. The similarity variables admit the following form

$$\tilde{x}_1 = \frac{x_1 + x_1^0}{\left(t + t^0\right)^{1/(1+m)}},\ \tilde{r}_i = \frac{r_i}{x_1 + x_1^*} \tag{A.31}$$

and the two-point correlation tensor is

$$R_{ij} = \left(x_1 + x_1^0\right)^{-2m} \tilde{R}_{ij}\left(\tilde{x}, \tilde{r}_i\right) \tag{A.32}$$

where the superscript x_1^0 and t^0 mark the *virtual origins* in space and time respectively. Analogously to the above example of the heat equation, eq. (A.31) describes the law of propagation of turbulence for the present case, i.e., for a fixed point in the similarity coordinates, e.g. $\tilde{x}_1$-$\tilde{k}$, the original spatial variable changes according to a power law.

- **Confined turbulent diffusion,** $a_1 = 0$ **and** $a_2 \neq 0$. In this case, the similarity variables are

$$\tilde{x}_1 = x_1 - x_1^0 \ln\left(t - t^0\right),\ \tilde{r}_i = r_i \tag{A.33}$$

and the two-point correlation is given by

$$R_{ij} = \exp\left(-2x_1/x_1^0\right) \tilde{R}_{ij}\left(\tilde{x}_1, \tilde{r}_i\right) \tag{A.34}$$

- **Rotating turbulent diffusion,** $a_1 \neq 0$ **and** $a_2 = 0$. Here, the similarity variables are given by

$$\tilde{x}_1 = \left(x_1 + x_0\right) \exp\left(-t/t_0\right),\ \tilde{r}_i = \frac{r_i}{x_1 + x_0} \tag{A.35}$$

and the two-point correlation is given by

$$R_{ij} = \left(x_1 + x_0\right)^2 \tilde{R}_{ij}\left(\tilde{x}_1, \tilde{r}_i\right) \tag{A.36}$$

B. Homogeneous turbulence forcing

This chapter explains the method of forcing the flow to obtatin a homogeneous turbulence field. The first section is concerned with isotropic turbulence in a non-rotating frame of reference. The second section treats the homogeneous turbulence in a rotating frame of reference. Both parts contain results of precursor DNS runs which are representative for the algorithms.

B.1. HIT

The forcing which keeps the homogeneous turbulence statistically steady adopted in the present work is based on Eswaran and Pope [15]. Originally, the forcing method was implemented in a pseudo-spectral Navier-Stokes solver with explicit time-stepping second-order Runge-Kutta scheme and exact treatment of the viscous terms. The solution domain was a periodic cube of side $L = 2\pi$ with N^3 equally spaced grid points. This setup implies the availability of N^3 discrete wavenumber vectors, components of which are integer multiples of the lowest wavenumber $\kappa_0 = 1$. The dependent variables in the simulation are the Fourier coefficients of the velocity field $\hat{\boldsymbol{u}}(\boldsymbol{\kappa}, t)$ at the wavenumber vectors $\boldsymbol{\kappa}$. The equation governing the evolution of a Fourier mode (derived from the Navier-Stokes equation) is

$$\frac{\partial \hat{\boldsymbol{u}}(\boldsymbol{\kappa}, t)}{\partial t} = \hat{\boldsymbol{a}}(\boldsymbol{\kappa}, t) + \hat{\boldsymbol{a}}_F(\boldsymbol{\kappa}, t) \tag{B.1}$$

where the acceleration $\hat{\boldsymbol{a}}(\boldsymbol{\kappa}, t)$ is due to the convective and diffusive contributions and the acceleration $\hat{\boldsymbol{a}}_F(\boldsymbol{\kappa}, t)$ is due to the forcing. The forcing acceleration is specified in the low wavenumber range $\kappa < 2\sqrt{2}\kappa_0$ by the following divergenceless expression

$$\hat{\boldsymbol{a}}_F(\boldsymbol{\kappa}, t) = \hat{\boldsymbol{b}}(\boldsymbol{\kappa}, t) - \boldsymbol{\kappa}\frac{\boldsymbol{\kappa} \cdot \hat{\boldsymbol{b}}(\boldsymbol{\kappa}, t)}{\boldsymbol{\kappa} \cdot \boldsymbol{\kappa}} \tag{B.2}$$

and the components of (the complex vector) $\hat{\boldsymbol{b}}(\boldsymbol{\kappa}, t)$ are six independent Ornstein-Uhlenbeck processes [24, 25] governed by the equation

$$\begin{aligned} \mathrm{d}c(t) &= -c(t)\frac{\mathrm{d}t}{T} + \left(\frac{2\sigma^2}{T}\right)^{1/2} \mathrm{d}W(t) \\ c(0) &= \mathcal{N}(0, \sigma^2) \end{aligned} \tag{B.3}$$

where T is a positive time scale, $\mathcal{N}(\mu, \sigma^2)$ is a Gaussian probability distribution function with mean μ and standard deviation σ and $W(t)$ is the Wiener process. The process is characterized by

$$\langle c(\boldsymbol{\kappa}, t) \rangle = 0 \tag{B.4}$$

and

$$\langle c(\boldsymbol{\kappa}, t) c^*(\boldsymbol{\kappa}, t+s) \rangle = 2\sigma^2 \exp(-s/T) \tag{B.5}$$

The implementation of the Ornstein-Uhlenbeck process proceeds as

$$[c_{P_\kappa}] = (1.0 - \alpha_f \Delta t) \, [c_{P_\kappa}]^{old} + \sigma_f \, [\mathcal{N}_{P_\kappa}] \tag{B.6}$$

i.e., for every resolved wavenumber in a prescribed interval forcing is specified by eq. (B.6). It is trivial to obtain the relationship between the parameters σ and T in eq. (B.3) and the corresponding implementation analogues α_f and σ_f. Force field in physical space is obtained by inverse Fourier transform of the zero-divergence part of the above expression (which is calculated as a cross product of eq. (B.6) and unit wavenumber vectors). The initial conditions are specified by constructing a divergenceless velocity field conforming to a spectrum function $E(\kappa)$ of the form

$$E(\kappa) = E_a \left(\frac{\kappa}{\kappa_a} \right)^4 \exp\left(-2 \left(\frac{\kappa}{\kappa_a} \right)^2 \right) \tag{B.7}$$

which is characterized by the wavenumber at which the energy spectrum has a maximum κ_a and the value of the spectrum at the maximum wavenumber E_a. In summary, in order to fully specify a simulation of HIT the following parameters need to be prescribed

- The size of the domain L
- The number of control volumes in each direction N
- The initial condition characterized by κ_a and E_a
- The kinematic viscosity ν
- The forcing characterized by T and σ and the forcing range $\kappa < 2\sqrt{2}\kappa_0$

In the FVM framework, as opposed to the pseudo-spectral framework in which the forcing method has been developed, only the term $\hat{\boldsymbol{a}}_F$ is manipulated in the spectral space. At each time step, the force, which in the FVM is an explicit source, is computed by an inverse Fourier transform of $\hat{\boldsymbol{a}}_F$. In the present study the FFTW[1] library's MPI routines have been used [17].

Supporting DNS runs were conducted in order to gain insight into the characteristics and performance of the algorithm in the FVM framework without an influence of modeling terms. DNS is performed for three different grids, $N^3 \in \{64^3, 96^3, 128^3\}$ keeping the rest of the input parameters the same. Figure B.1 shows the instantaneous values of the large-scale eddy-turnover time for HIT. The runs start from artificial initial conditions and two eddy-turnover times are required for the fields to reach a statistically steady state. The duration of the simulation in the statistically steady state is roughly six eddy-turnovertimes which is sufficient for the present purpose of gaining insight into the performance of the algorithm.

In order to give an impression of the turbulence field in the steady state fig. B.2 shows isocontours of enstrophy colored by velocity magnitude for $N = 128$. Clearly observable is the intermittent arrangement of regions, vortex tubes and sheets, of intense dissipation,

Case	N	σ	α	k_a	E_a	κ_f	Re_λ
dnsHit1	64	0.483	40	2	10	$2\sqrt{2}$	36
dnsHit2	96	0.483	40	2	10	$2\sqrt{2}$	32
dnsHit3	128	0.483	40	2	10	$2\sqrt{2}$	30

Table B.1.: Summary of parameters of the DNS of HIT

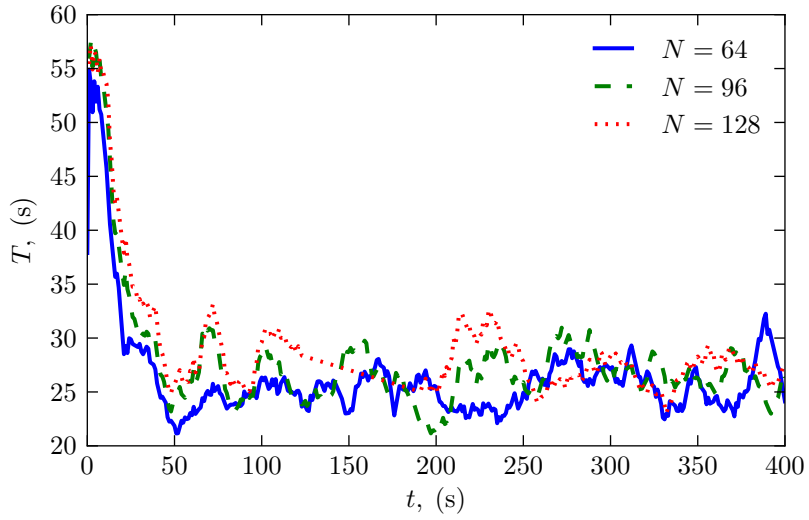

Figure B.1.: Eddy-turnover time T for three grids as calculated by $T \equiv L/u_{\mathrm{rms}}$, where $L \equiv k^{3/2}/\epsilon$ and $u_{\mathrm{rms}} \equiv \frac{2}{3}k$

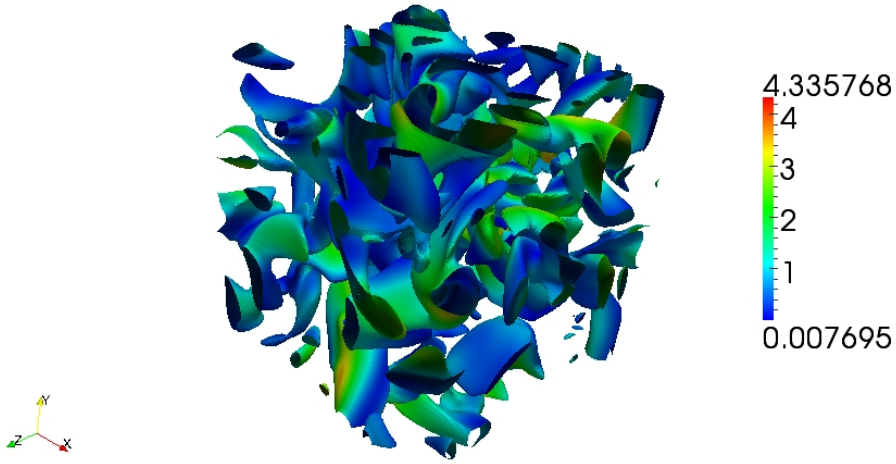

Figure B.2.: Isocontour of enstrophy colored by $U^2/\langle U^2 \rangle$ calculated from the resolved velocity from rotDnsHit2; figure shows the isocontour at $\langle \omega^2 \rangle + 4\sigma_{\omega^2}$, where σ_{ω^2} is the standard deviation of enstrophy [35].

commonly encountered in large-scale forced HIT. The resolution of the smallest scales is shown in fig. B.3. The Taylor-microscale Reynolds number is shown in fig. B.4. The

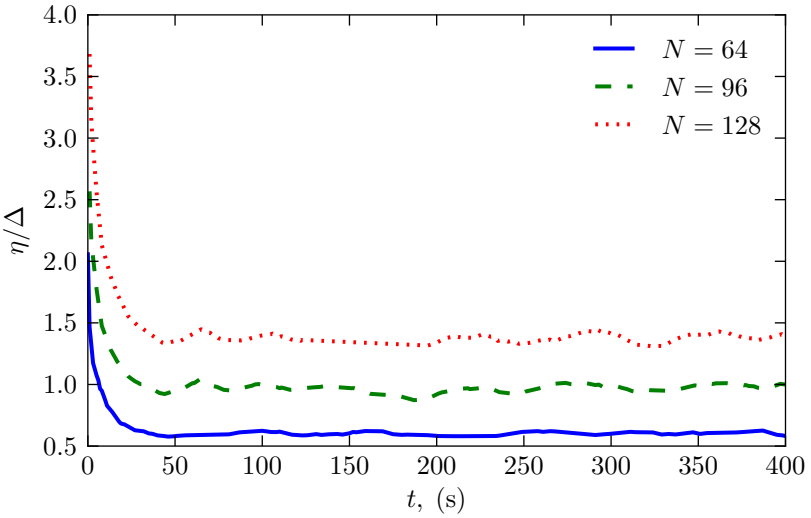

Figure B.3.: Kolmogorov scale $\eta \equiv (\nu^3/\epsilon)^{1/4}$ compared to the grid size $\Delta \equiv 2\pi/N$

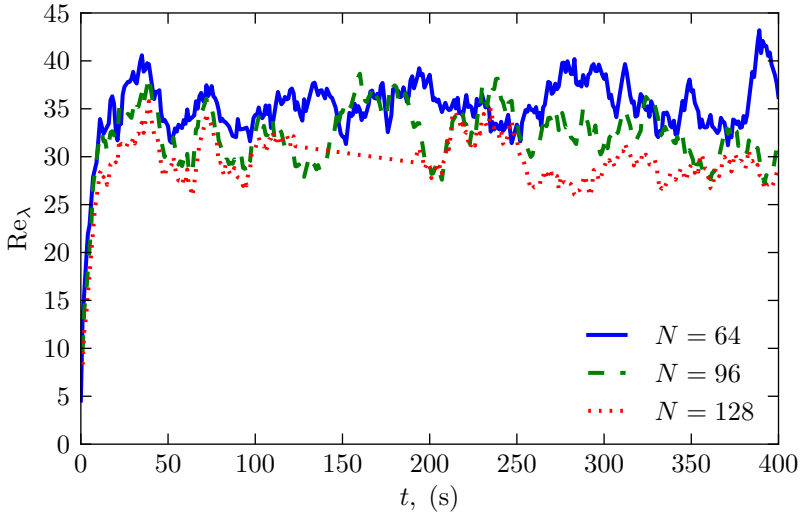

Figure B.4.: Taylor-microscale Reynolds number $\mathrm{Re}_\lambda \equiv u_{\mathrm{rms}}\lambda/\nu$ where $\lambda \equiv \sqrt{15\nu u_{\mathrm{rms}}^2/\epsilon}$

normalized energy spectrum function is compared to a DNS of Jiménez et al. [39] in fig. B.5. The forcing and slightly different Reynolds number cause a deviation from the DNS at the largest scales, while the energy transfer and the rate of dissipation are well captured. Figure B.6 shows the alignment of the vorticity vector with the eigenvalues of the rate of strain tensor and the joint PDF of the invariants of the velocity gradient tensor which

[1]The actual version used is the FFTW 2.1.5 being the latest production version for the MPI routines, http://www.fftw.org/, April, 2010

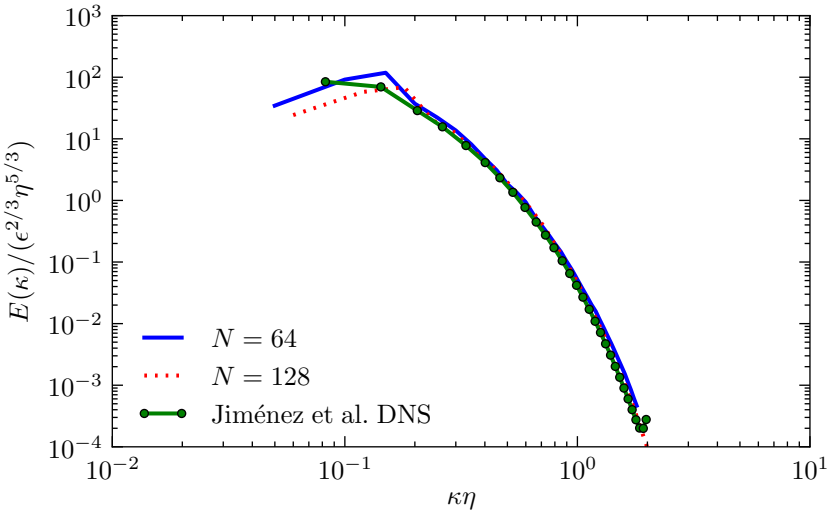

Figure B.5.: Non-dimensional energy spectrum function from present simulations compared to a pseudo-spectral DNS of [39] at $\mathrm{Re}_\lambda = 36.4$

present universal statistics of small scale turbulence [14]. These statistics are very well reproduced in the present simulations.

B.2. Rotating homogeneous turbulence

Literature on the rotating homogeneous turbulence is scarce in comparison to the non-rotating case, the chief reason being the difficulty to experimentally or numerically produce suitable turbulent fields. The main characteristics of the rotating homogeneous turbulence (a turbulence which is freely decaying in a suddenly applied rotation from initial isotropic state) are, quoting Sagaut and Cambon [62]

- Rotation inhibits the energy cascade so that the dissipation rate is reduced[...]
- The initial 3-D isotropy is broken, so that a moderate anisotropy [...] develops.
- Elongated vortical structures are generated with asymmetry in terms of cyclonic and anticyclonic axial vorticity [...] structures with cyclonic vorticity being observed to be dominant.

The majority of previous studies, be them experimental or numerical, have been carried out for the decaying case. However, the turbulent diffusion case treated here, imposes a requirement of having a statistically steady source of turbulent kinetic energy in the rotating frame, which necessitates a simulation of statistically steady rotating turbulence box. A number of studies dealing with direct simulations of steady rotating turbulence in a box may be mentioned here, e.g. Favier et al. [16], Müller and Thiele [52], Yeung and Zhou [72]. In Yeung and Zhou [72] the forcing is kept the same as in the HIT case. Favier

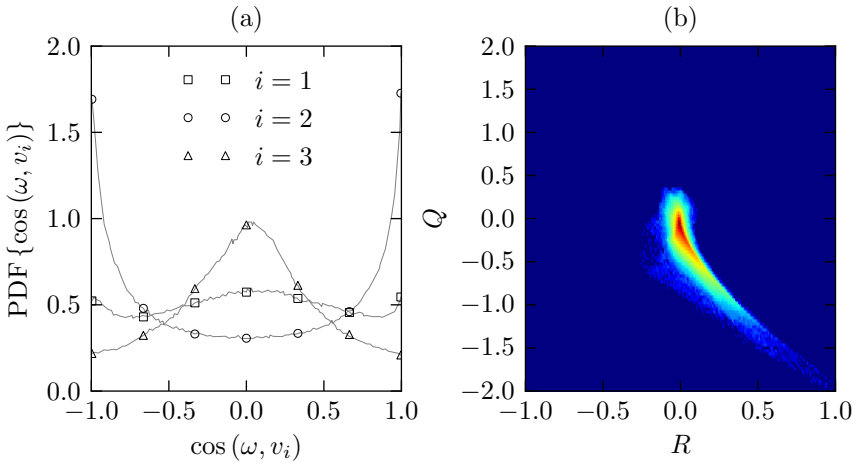

Figure B.6.: Universal statistics: (a) allignment of the vorticity vector with eigenvectors of the rate of strain; (b) tear-drop shape of the joint probability-density function of the invariants of the velocity gradient tensor.

Case	N	κ_f	Ω	Re_λ
rotDnsHit1	64	$2\sqrt{2}$	2π	30
rotDnsHit2	96	$2\sqrt{2}$	2π	30

Table B.2.: Summary of parameters of the DNS of rotating homogeneous turbulence

et al. [16] inject energy globally lost due to viscous effects in a range of small wavenumbers prescribed. The third method, applied in Müller and Thiele [52] fixes the Fourier modes in a prescribed range of small wavenumbers, so that only the wavenumbers outside of this range are allowed to evolve. It is worth noting that these simulations are performed in a pseudo-spectral numerical setting and that their properties may not uniquely map to the present FVM. All three mentioned methods have been tested in the present study. The methods of [16, 72] have exibited instability in the present FVM framework. The instability in these cases comes from a significant disproportion between the input of energy by the forcing and reduced dissipation rate due to rotation, so that the energy within the turbulence box grows unboundedly with time. For these reason, the method of Müller and Thiele [52] has been selected.

Figure B.7 and fig. B.8 show enstrophy isosurfaces of the second case rotDnsHit2 of homogeneous rotating turbulence at initial time step and after 6 full rotations. Isosurfaces get more structured as the rotation progresses along with the increase of the overall energy intensity due to depletion of the dissipation rate.

Universal aspects of turbulence at the start and after 6 rotations are shown in fig. B.9 and fig. B.10. The alignment of the vorticity and eigenvectors of the strain rate is reduced [22], and the tail of the tear-drop shape of the joint PDF of the invariants of the strain rate is reduced consistent with the reduction in dissipation [69].

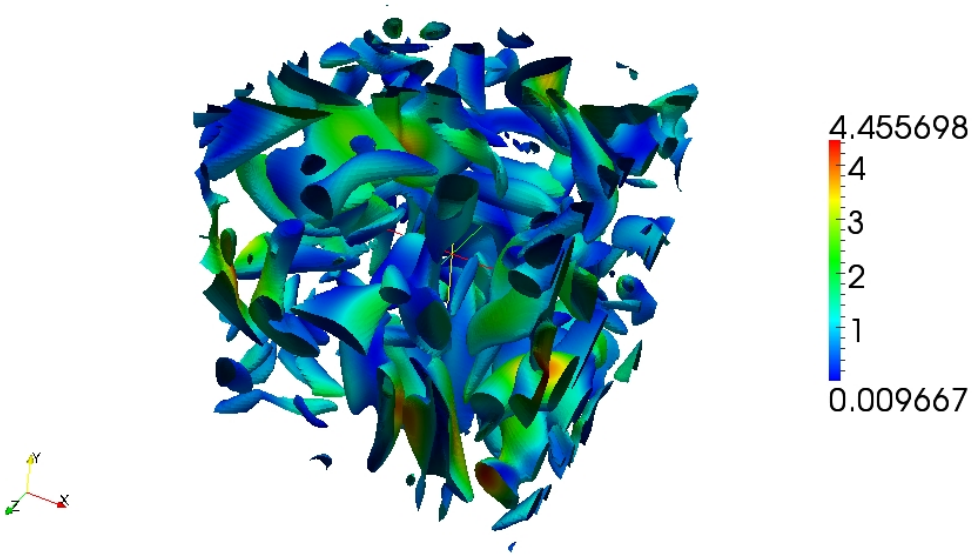

Figure B.7.: Isocontour of enstrophy colored by $U^2/\langle U^2 \rangle$ calculated from the resolved velocity from rotDnsHit2; figure shows the isocontour at $\langle \omega^2 \rangle + 4\sigma_{\omega^2}$, where σ_{ω^2} is the standard deviation of enstrophy [35] at initial time, i.e. corresponding to initial isotropic turbulence.

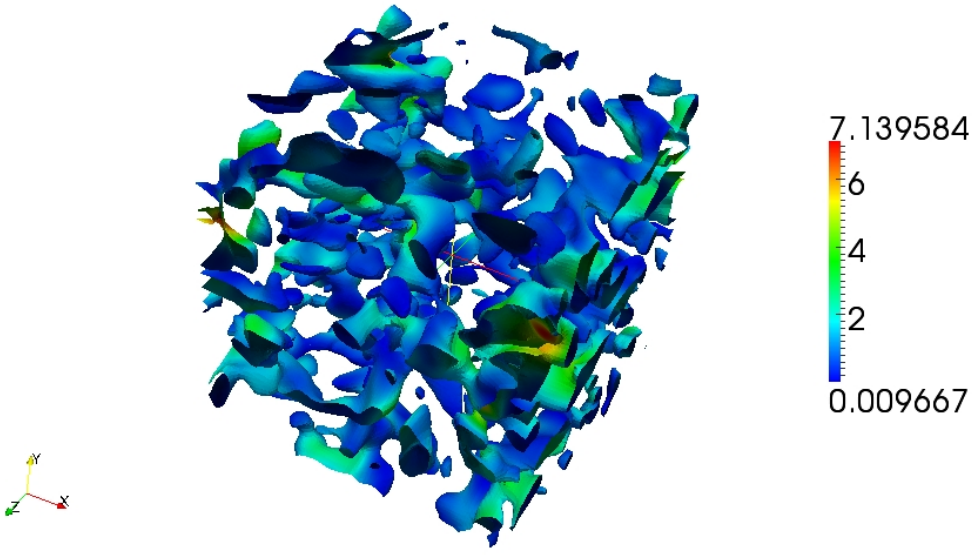

Figure B.8.: Isocontour of enstrophy colored by $U^2/\langle U^2 \rangle$ calculated from the resolved velocity from rotDnsHit2; figure shows the isocontour at $\langle \omega^2 \rangle + 4\sigma_{\omega^2}$, where σ_{ω^2} is the standard deviation of enstrophy [35] after 6 rotations.

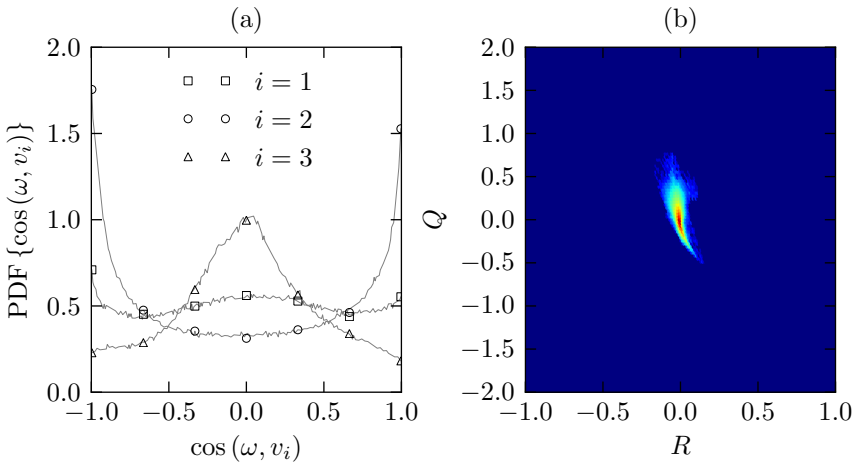

Figure B.9.: Universal statistics for DNS of homogeneous rotating turbulence: (a) allignment of the vorticity vector with eigenvectors of the rate of strain; (b) tear-drop shape of the joint probability-density function of the invariants of the velocity gradient at initial time.

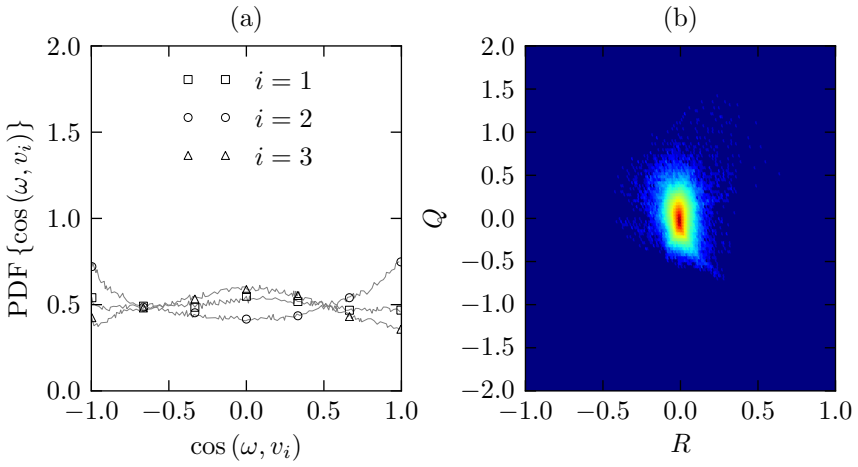

Figure B.10.: Universal statistics for DNS of homogeneous rotating turbulence: (a) allignment of the vorticity vector with eigenvectors of the rate of strain; (b) tear-drop shape of the joint probability-density function of the invariants of the velocity gradient after 6 rotations.

Bibliography

[1] R. K. Anand, B. J. Boersma, and A. Agrawal. "Detection of turbulent/non-turbulent interface for an axisymmetric turbulent jet: evaluation of known criteria and proposal of a new criterion." In: *Experiments in Fluids* 47 (2009), pp. 995–1007.

[2] G. W. Bluman and S. C. Anco. *Symmetry and integration methods for differential equations*. Springer, 2002.

[3] G. W. Bluman, A. F. Cheviakov, and S. C. Anco. *Applications of symmetry methods to partial differential equations*. Springer, 2010.

[4] J. Boussinesq. "Essai sur la théorie des eaux courantes." In: *Mémoires présentés par divers savants à l'Académie des Sciences XXIII* 1 (1877), pp. 1–680.

[5] G. Campagne, J.-B. Cazalbou, L. Joly, and P. Chassaing. "The structure of a statistically steady turbulent boundary layer near a free-slip surface." In: *Physics of Fluids* 21.6 (2009), pp. 065111–+.

[6] B. J. Cantwell. *Introduction to symmetry analysis*. Cambridge University Press, 2002.

[7] J. B. Cazalbou and P. Chassaing. "New results on the model problem of the diffusion of turbulence from a plane source." In: *Physics of Fluids* 13.2 (2001), pp. 464–475.

[8] J. B. Cazalbou and P. Chassaing. "The structure of the solution obtained with Reynolds-stress-transport models at the free-stream edges of turbulent flows." In: *Physics of Fluids* 14.2 (2002), pp. 597–611.

[9] J. B. Cazalbou, P. R. Spalart, and P. Bradshaw. "On the behavior of two-equation models at the edge of a turbulent region." In: *Physics of Fluids* 6.5 (1994), pp. 1797–1804.

[10] C. B. Da Silva and R. R. Taveira. "The thickness of the turbulent/nonturbulent interface is equal to the radius of the large vorticity structures near the edge of the shear layer." In: *Physics of Fluids* 22.12, 121702 (2010), p. 121702.

[11] B. J. Daly and F. H. Harlow. "Transport equations in turbulence." In: *Physics of Fluids* 13 (1970), pp. 2634–2649.

[12] S. C. Dickinson and R. R. Long. "Laboratory study of the growth of a turbulent layer of fluid." In: *Physics of Fluids* 21.10 (1978), pp. 1698–1701.

[13] S. C. Dickinson and R. R. Long. "Oscillating-grid turbulence including effects of rotation." In: *Journal of Fluid Mechanics* 126.-1 (1983), pp. 315–333.

[14] G. E. Elsinga and I. Marusic. "Universal aspects of small-scale motions in turbulence." In: *Journal of Fluid Mechanics* 662 (2010), pp. 514–539.

[15] V. Eswaran and S. B. Pope. "An examination of forcing in direct numerical simulations of turbulence." In: *Computers & Fluids* 16.3 (1988), pp. 257 –278.

[16] B. Favier, F. S. Godeferd, and C. Cambon. "On space and time correlations of isotropic and rotating turbulence." In: *Physics of Fluids* 22.1, 015101 (2010), p. 015101.

[17] M. Frigo and S. G. Johnson. "The design and implementation of FFTW3." In: *Proceedings of the IEEE* 93.2 (2005). Special issue on "Program Generation, Optimization, and Platform Adaptation", pp. 216–231.

[18] C. Fureby, G. Tabor, H. G. Weller, and A. D. Gosman. "A comparative study of subgrid scale models in homogeneous isotropic turbulence." In: *Physics of Fluids* 9.5 (1997), pp. 1416–1429.

[19] W. K. George and H. Wang. "The exponential decay of homogeneous turbulence." In: *Physics of Fluids* 21.2, 025108 (2009), p. 025108.

[20] M. Germano. "Turbulence - the filtering approach." In: *Journal of Fluid Mechanics* 238 (1992), pp. 325–336.

[21] M. Germano, U. Piomelli, P. Moin, and W. H. Cabot. "A dynamic subgrid-scale eddy viscosity model." In: *Physics of Fluids* 3 (1991), pp. 1760–1765.

[22] B. J. Geurts, D. Holm, and A. Kuczaj. *Direct and large-eddy simulation of rotating turbulence*. 2007. URL: http://www3.imperial.ac.uk/pls/portallive/docs/1/18181703.PDF (visited on 05/25/2011).

[23] M. M. Gibson and B. E. Launder. "Ground effects on pressure fluctuations in the atmospheric boundary layer." In: *Journal of Fluid Mechanics* 86 (1978), pp. 491–511.

[24] D. T. Gillespie. "Exact numerical simulation of the Ornstein-Uhlenbeck process and its integral." In: *Physical Review E* 54.2 (1996), pp. 2084–2091.

[25] D. T. Gillespie. "The mathematics of Brownian motion and Johnson noise." In: *American Journal of Physics* 64.3 (1996), pp. 225–240.

[26] F. S. Godeferd and L. Lollini. "Direct numerical simulations of turbulence with confinement and rotation." In: *Journal of Fluid Mechanics* 393.-1 (1999), pp. 257–308.

[27] S. Guenther. "Symmetry methods for turbulence modelling." PhD thesis. TU Darmstadt, 2005.

[28] M. Holzner, A. Liberzon, N. Nikitin, B. Lüthi, W. Kinzelbach, and A. Tsinober. "A Lagrangian investigation of the small-scale features of turbulent entrainment through particle tracking and direct numerical simulation." In: *Journal of Fluid Mechanics* 598.-1 (2008), pp. 465–475.

[29] M. Holzner, B. Lüthi, A. Tsinober, and W. Kinzelbach. "Acceleration, pressure and related quantities in the proximity of the turbulent/non-turbulent interface." In: *Journal of Fluid Mechanics* 639.-1 (2009), pp. 153–165.

[30] M. Holzner, A. Liberzon, M. Guala, A. Tsinober, and W. Kinzelbach. "Generalized detection of a turbulent front generated by an oscillating grid." In: *Experiments in Fluids* 41 (2006), pp. 711–719.

[31] E. J. Hopfinger and J. A. Toly. "Spatially decaying turbulence and its relation to mixing across density interfaces." In: *Journal of Fluid Mechanics* 78.01 (1976), pp. 155–175.

[32] E. J. Hopfinger, F. K. Browand, and Y. Gagne. "Turbulence and waves in a rotating tank." In: *Journal of Fluid Mechanics* 125.-1 (1982), pp. 505–534.

[33] J. C. R. Hunt, I. Eames, C. B. da Silva, and J. Westerweel. "Interfaces and inhomogeneous turbulence." In: *Royal Society of London Philosophical Transactions Series A* 369 (2011), pp. 811–832.

[34] D. Hurst and J. C. Vassilicos. "Scalings and decay of fractal-generated turbulence." In: *Physics of Fluids* 19.3, 035103 (2007), p. 035103.

[35] T. Ishihara, T. Gotoh, and Y. Kaneda. "Study of high-Reynolds number isotropic turbulence by direct numerical simulation." In: *Annual Review of Fluid Mechanics* 41 (2009), pp. 165–180.

[36] R. I. Issa. "Solution of the implicitly discretised fluid flow equations by operator-splitting." In: *Journal of Computational Physics* 62.1 (1986), pp. 40 –65.

[37] H. Jasak. "Error analysis and estimation for the finite volume method with applications to fluid flows." PhD thesis. Imperial College of Science, Technology and Medicine, 1996.

[38] H. Jasak. *Numerical solution algorithms for compressible flows.* Course prepared for the Aerospace Engineering Program, Tempus NUSIC Project JEP-18085-2003. 2006.

[39] J. Jiménez, A. A. Wray, P. G. Saffman, and R. S. Rogallo. "The structure of intense vorticity in isotropic turbulence." In: *Journal of Fluid Mechanics* 255.-1 (1993), pp. 65–90.

[40] G. Khujadze and M. Oberlack. "DNS of vibrating grid turbulence." In: *Sixth International Symposium on Turbulence and Shear-Flow Phenomena.* 2009.

[41] M. Kinzel. "Experimental investigation of turbulence under the influence of confinement and rotation." PhD thesis. TU Darmstadt, 2010.

[42] M. Kinzel, M. Holzner, B. Lüthi, C. Tropea, W. Kinzelbach, and M. Oberlack. "Experiments on the spreading of shear-free turbulence under the influence of confinement and rotation." In: *Experiments in Fluids* 47.4 (2009), pp. 801–809.

[43] S. Laizet, E. Lamballais, and J. C. Vassilicos. "A numerical strategy to combine high-order schemes, complex geometry and parallel computing for high resolution DNS of fractal generated turbulence." In: *Computers & Fluids* 39.3 (2010), pp. 471 –484.

[44] B. E. Launder and N. D. Sandham, eds. *Closure strategies for turbulent and transitional flows.* Cambridge University Press, 2000.

[45] S. K. Lele. "A consistency condition for Reynolds stress closures." In: *Physics of Fluids* 28.1 (1985), pp. 64–68.

[46] D. K. Lilly. "A proposed modification of the Germano subgrid-scale closure method." In: *Physics of Fluids* 4 (1992), pp. 633–635.

[47] OpenCFD Ltd. http://www.opencfd.co.uk/openfoam/. 2010.

[48] OpenCFD Ltd. *OpenFOAM®, The open source CFD toolbox, Programmers guide, Version 1.6.* 2009.

[49] OpenCFD Ltd. *OpenFOAM®, The open source CFD toolbox, User guide, Version 1.6.* 2009.

[50] J. Mathew and J. A. Basu. "Some characteristics of entrainment at a cylindrical turbulence boundary." In: *Physics of Fluids* 14.7 (2002), pp. 2065–2072.

[51] P. Moin and K. Mahesh. "Direct numerical simulation: a tool in turbulence research." In: *Annual Review of Fluid Mechanics* 30.1 (1998), pp. 539–578.

[52] W.-C. Müller and M. Thiele. "Scaling and energy transfer in rotating turbulence." In: *Europhysics Letters* 77.3 (2007), p. 34003.

[53] M. Oberlack. "A unified approach for symmetries in plane parallel turbulent shear flows." In: *Journal of Fluid Mechanics* 427.-1 (2001), pp. 299–328.

[54] M. Oberlack. "Symmetrie, Invarianz und Selbständlichkeit in der Turbulenz." Habilitationsschrift. RWTH Aachen, 2000.

[55] M. Oberlack. "Symmetries and invariant solutions of turbulent flows and their implications for turbulence modelling." In: *Theories of Turbulence*. Ed. by Oberlack M. and Busse F. Springer, 2002.

[56] M. Oberlack and S. Guenther. "Shear-free turbulent diffusion—classical and new scaling laws." In: *Fluid Dynamics Research* 33.5-6 (2003), p. 453.

[57] B. Perot and P. Moin. "Shear-free turbulent boundary layers. Part 1. Physical insights into near-wall turbulence." In: *Journal of Fluid Mechanics* 295 (1995), pp. 199–227.

[58] S. B. Pope. *Turbulent flows*. Cambridge University Press, 2000.

[59] R. R. Prasad and K. R. Sreenivasan. "Scalar interfaces in digital images of turbulent flows." In: *Experiments in Fluids* 7 (1989), pp. 259–264.

[60] F. Risso and J. Fabre. "Diffusive turbulence in a confined jet experiment." In: *Journal of Fluid Mechanics* 337 (1997), pp. 233–261.

[61] J. Rotta. "Statistische Theorie nichthomogener Turbulenz." In: *Zeitschrift fur Physik* 129 (1951), pp. 547–572.

[62] P. Sagaut and C. Cambon. *Homogeneous turbulence dynamics*. Cambridge University Press, 2008.

[63] D. Shirokoff and R. Ruben Rosales. "An efficient method for the incompressible Navier-Stokes equations on irregular domains with no-slip boundary conditions, high order up to the boundary." In: *ArXiv e-prints* (2010).

[64] P. J. Staplehurst, P. A. Davidson, and S. B. Dalziel. "Structure formation in homogeneous freely decaying rotating turbulence." In: *Journal of Fluid Mechanics* 598 (2008), pp. 81–105.

[65] H. Stephani. *Differential equations. Their solutions using symmetries*. Cambridge University Press, 1989.

[66] A. G. Straatman. "A modified model for diffusion in second-moment turbulence closures." In: *Journal of Fluids Engineering* 121.4 (1999), pp. 747–756.

[67] A. G. Straatman, G. D. Stubley, and G. D. Raithby. "Examination of diffusion modeling using zero-mean-shear turbulence." In: *AIAA Journal* 36.6 (1998), pp. 929–935.

[68] H. Tennekes and J.L. Lumley. *A first course in turbulence*. The MIT Press, 1972.

[69] A. Tsinober. *An informal conceptual introduction to turbulence*. Springer, 2009.

[70] H. G. Weller, G. Tabor, H. Jasak, and C. Fureby. "A tensorial approach to computational continuum mechanics using object-oriented techniques." In: *Computers in Physics* 12 (1998), pp. 620–631.

[71] J. Westerweel, C. Fukushima, J. M. Pedersen, and J. C. R. Hunt. "Mechanics of the turbulent-nonturbulent interface of a jet." In: *Physical Review Letters* 95.17 (2005), p. 174501.

[72] P. K. Yeung and Y. Zhou. "Numerical study of rotating turbulence with external forcing." In: *Physics of Fluids* 10.11 (1998), pp. 2895–2909.

[73] A. T. Zang. "On the rotation and skew-symmetric forms for incompressible flow simulations." In: *Applied Numerical Mathematics* 7.1 (1991), pp. 27 –40.

List of figures

List of tables

Curriculum Vitae

Emir Sirbubalo

E-mail: emir.sirbubalo@gmail.com

Personal

Date of birth: August 07, 1982

Place of birth: Sarajevo

Nationality: Bosnia and Herzegovina

Education

1997-2001 Druga gimnazija Sarajevo, high school

2001-2006 Faculty of Mechanical Engineering, University of Sarajevo, Dipl.-Ing. in mechanical engineering

2006-2010 TU Darmstadt, doctoral study in mechanical engineering